MESOSCALE MODELING STUDY OF A POLAR LOW IN THE CHUKCHI AND BEAUFORT SEAS

By

Paula Doubrawa Moreira

RECOMMENDED:

John E Walsh

Xiangdong Zhang

Advisory Committee Chair

Nicole Mölders

Chair, Department of Atmospheric Sciences

APPROVED:

Dean, College of Natural Science and Mathematics

Lawrence K Duffy

Dean of the Graduate School

Nov 29, 2011

Date

MESOSCALE MODELING STUDY OF A POLAR LOW IN THE CHUKCHI AND BEAUFORT SEAS

A

THESIS

Presented to the Faculty

of the University of Alaska Fairbanks

in Partial Fulfillment of the Requirements

for the Degree of

MASTER OF SCIENCE

By

Paula Doubrawa Moreira, B.S.

Fairbanks, Alaska

December 2011

Abstract

Polar lows are intense mesoscale maritime cyclones, often associated with strong winds that can damage high-latitude coastal environments and infrastructure. These systems have been historically infrequent in the Chukchi and Beaufort seas, but this behavior is expected to change along with the amplified changes in Arctic climate. This study investigates the unusual occurrence of a polar low in this region on October 9-10, 2009. Sensitivity experiments with the Weather Research and Forecasting model indicate that using ERA-Interim as large-scale forcing and performing spectral nudging at all simulation hours yield the most realistic simulation. The simulations are highly sensitive to physical parameterizations, where Morrison microphysics and Yonsei University boundary layer produce the smallest errors. Surface forcings were not important for the polar low development and their influence could not extend above 850 hPa due to a stable lower atmosphere. A convergence zone between the Aleutian Low and the Beaufort High established a southerly flow that created favorable conditions by continuously advecting heat and moisture from lower latitudes. The polar low had a hybrid development and was likely triggered by the interaction between a deep-penetrating upper-level potential vorticity anomaly and a low-level baroclinic zone, which were driven northward by the jet stream.

Table of Contents

Page

Page

List of Figures

Page

List of Tables

Page

Acknowledgements

Illustration by Antoine de Saint-Exupéry

I would like to thank my advisor Dr. Xiangdong Zhang for giving me the opportunity to come to Alaska and experience atmospheric sciences in ways that I would never have imagined. I will never forget this experience that taught me so much about science, nature, people, and myself. I also thank him for all his advice and comments regarding my research and thesis. I also would very much like to thank my committee members Dr. Richard Collins and Dr. John Walsh for their encouragement and valuable comments which have guided me in the best of ways and significantly improved this work.

I would also like to thank Dr. Nicole Mölders for all her encouragement, and Dr. Uma Bhatt who was always available to help with scientific questions and whose bits of advice allowed me to keep on going. I thank the entire "Mesoscale Meteorology Study" research group, especially Jeremy Krieger who eased my entrance into the modeling world and was always available to answer my desolate programming inquiries. I thank Dr. Jun Inoue for providing the ship sounding data that was used in this study and Eric Stevens from the National Weather Service for providing surface charts and warnings.

Finally, huge thanks to my good friends, for understanding and comforting me in moments of distress and for being such good companions in moments of enjoyment.

This research was funded by the Department of Interior/Bureau of Ocean Energy Management, Regulation and Enforcement through Contract M06PC00018, the National Science Foundation/Office of Polar Program under grant ARC-1023592, and the Japanese Agency of Marine and Earth Science and Technology project "Storm activity and atmosphere-sea ice-ocean interaction." The computational resources were provided by the Arctic Region Supercomputing Center.

Chapter 1: Introduction and Motivation

1.1 Overview on Polar Lows

Many definitions have been proposed to describe polar lows, most of which emphasize on characteristics such as intensity, scale and location. The one adopted throughout this thesis was proposed by Rasmussen and Turner (2003) when attempting to produce a general description based on previously proposed definitions. With that in mind, polar lows can be described as intense maritime mesoscale cyclones that form poleward of a major baroclinic zone. The spatial scale may range from 200 to 1000 km and the surface winds should be near gale force (~17 m s^{-1}).

The effects of polar lows have been noticed for a long time and the first references to these systems date back to the early 1950s (Sumner 1950; Dannevig 1954). Due to their small scale and the sparseness of data in the regions where they occur, detailed analyses of polar lows were only made possible once satellite imagery became available for meteorological studies in the early 1960s. The first known image of a polar low (Figure 1.1) dates back to January 5, 1970 (Lyall 1972) and from then on many studies have followed. Up to this day, research initiatives seek to understand the manifold dynamics of polar lows, ranging from analyses based purely on convective activity (e.g., Linders and Saetra 2010) to those focused on baroclinic processes (e.g., Yanase and Niino 2007). However, most polar lows are hybrid systems (e.g., Bracegirdle and Gray 2008) and thus, cannot be explained by one single theory.

Figure 1.1: First known satellite image of a polar low. The Polar low is off the British coast. Reference: Lyall (1972).

The fact that polar lows occur associated with varied synoptic conditions and dynamical processes is precisely the greatest challenge in studying these systems. In order to avoid confusion, the term "polar low spectrum" has been coined and refers to the wide range of polar low types. Due to this large spectrum several authors have proposed different ways of classifying these systems. Five of the major polar low classifications are listed in Table 1.1 and are based on different parameters such as cloud morphology (Forbes and Lottes 1985; Rasmussen and Turner 2003), synoptic background (Businger and Reed 1989; Rasmussen and Turner 2003), and triggering instability processes (Gang 2001). The most intuitive and simple classification pertains to their morphology, where polar lows can be either spiraliform or comma-shaped. In the first case, they resemble tropical cyclones (Figure 1.2a) and may be referred to as "Arctic hurricanes." In this case, they usually develop within cold air masses (Rasmussen and Turner 2003). On the

other hand, when presenting a comma-shaped cloud structure they resemble extratropical cyclones (Figure 1.2b) and are often related to a differential vorticity anomaly between upper and lower levels (Rasmussen and Turner 2003). By examining these classifications, it is clear that there are no strict criteria for categorizing polar lows. The forcing mechanisms may vary from case to case or even within an individual case. While in some instances it may be possible to apply strict classifications, they are often not ideal.

Table 1.1: Polar low classifications proposed by different authors.

Rasmussen (1983)	**Forbes and Lottes (1985)**	**Businger and Reed (1989)**	**Gang (2001)**	**Rasmussen (2003)**
Primary (spiral)	Comma, deep spiral	Short-wave/ jet-streak	Baroclinic Instability	Reverse shear
	Merry-go-round or ring of vortices			Troughs
	Crescent	Arctic Front	Barotropic Instability	Boundary layer fronts
	Oval, solid mass			Cold lows
Secondary (comma)	Multiple deep bands			Comma clouds
	Multiple shallow bands	Cold low	CISK or WISHE	Baroclinic wave forward shear
	Single deep band			
	Single shallow band			Orographic

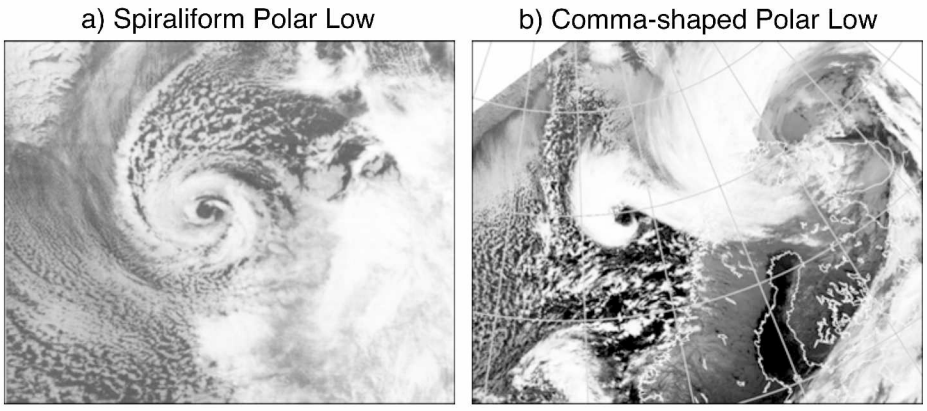

Figure 1.2: Polar lows off the Norwegian coast. Spiraliform low (a) on February 27 1987 (Nordeng and Rasmussen 1992) and comma-shaped low (b) October 14 1993 (Claud et al. 2004).

Polar lows have been studied for decades in the North Pacific (e.g., Reed 1979; Businger 1987; Yanase et al. 2004), North Atlantic (e.g., Harrold and Browning 1969; Mailhot et al. 1996; Condron et al. 2006) and Northern Seas (e.g., Shapiro et al. 1987; Turner et al. 1992; Brümmer et al. 2009). Various studies have also been carried out for the southern hemisphere (e.g., Auer 1986; Turner et al. 1993; Heinemann 1996). On the other hand, very little attention has been given to the Chukchi and Beaufort Seas (CBS), which are known to present a general minimum of cyclone frequency and intensity when compared to other regions of the Arctic (Lynch et al. 2003). This reduced cyclogenesis is due not only to the increased sea-ice concentration in this sector, but also to the climatological high-pressure system that is present over this region especially in the winter months, known as the Beaufort High (Figure 1.3). As a result, there are very few documented cases of polar lows in this area, most of which are unpublished records (Rasmussen and Turner 2003). Some examples are mentions of storms in 1970 (Wilson

1971) and in 1982 (Black 1982) through unpublished manuscripts and in 1985 (Fett 1992) in a U.S. Navy guide.

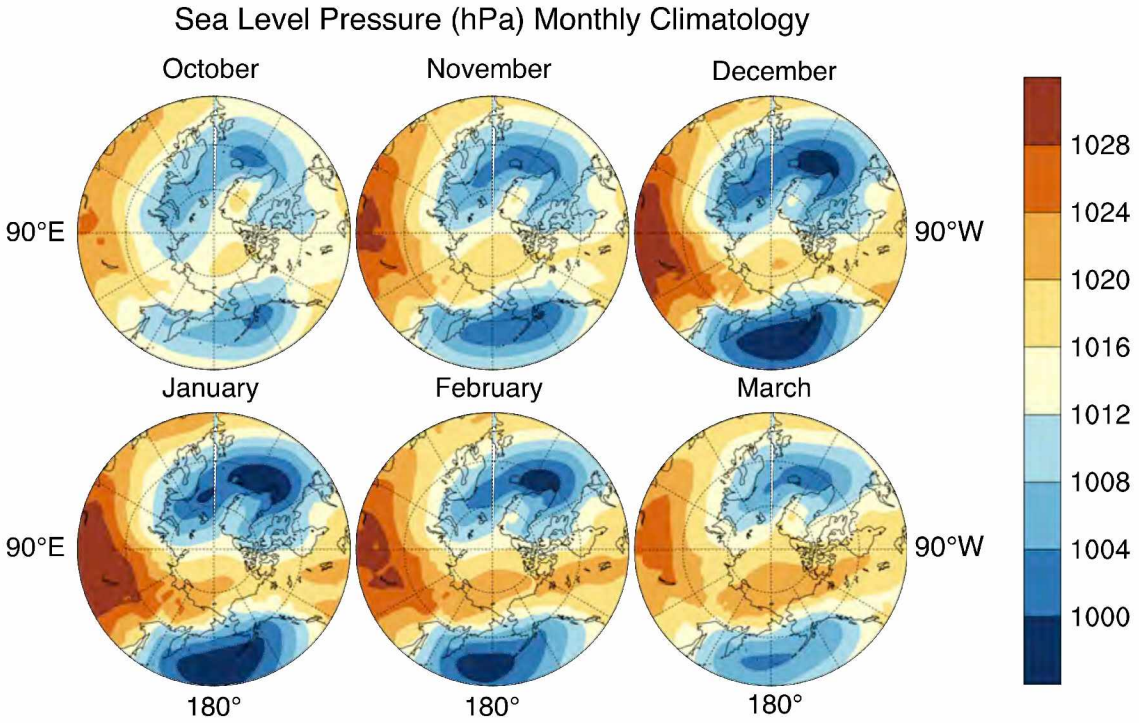

Figure 1.3: Sea-level pressure monthly climatology. Calculated from 1979-2009 European Reanalysis (ERA) Interim monthly fields from October through March from 45°N to 90°N. Unit: hPa.

One of the few published records of polar low studies in the region of the CBS was conducted by Parker (1989). He examined detailed surface charts for periods of open water from 1976 to 1989 and concluded that polar lows are indeed rare in the region but may be prone to develop in years of minimum sea-ice cover. The recent observations and the Coupled Model Intercomparison Project (CMIP) climate model projections suggest a

rapid reduction of sea-ice coverage over the CBS (e.g., Zhang and Walsh 2006; Comiso et al. 2008; Zhang et al. 2008). These changes are expanding the area and increasing the persistence of open water, which suggests that this sector should exhibit more favorable conditions for the formation of polar mesocyclones that depend on maritime forcings for their development. However, this expected increase in polar low frequency should not be generalized to other regions. On the contrary, studies focusing on the North Atlantic have found a negative trend for the occurrence of polar lows (Zahn and von Storch 2010) and of marine cold-air outbreaks (Kolstad and Bracegirdle 2008), which are one of the main triggers for polar low development.

Due to their intense nature and the location where they occur, polar lows have been a concern for forecasters and researchers for many decades. They can affect not only marine activities, but also high-latitude environments and infrastructure by presenting a risk for storm surges, flooding and erosion (e.g., Cassano et al. 2006). These coastal and marine arctic areas are often large hubs of oil industry and such intense cyclones may additionally threaten the environment by acting on the dispersion of potential oil spills. With that in mind, the Alaska coast (Figure 1.4) presents itself as an ideal example of vulnerability. Not only is it home to extensive oil development and frequent spill occurrences (Figure 1.5), but it is also seriously affected by surge episodes (Owen Mason 1997). As illustrated in Figure 1.6 storm surges, flooding and erosion events associated with coastal storms have had serious effects on the land and activities of Alaska coastal villages and oil industry operations.

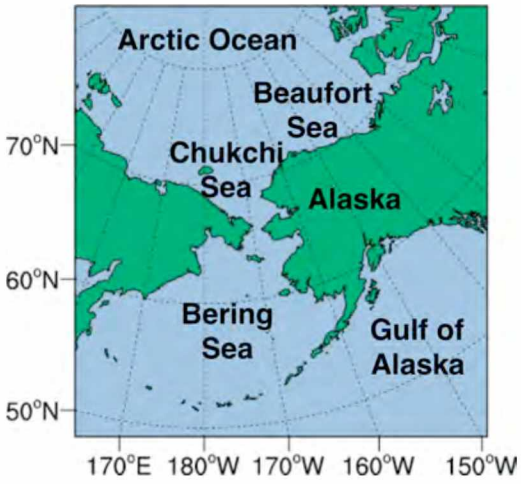

Figure 1.4: The Alaska coast and surrounding continents and bodies of water.

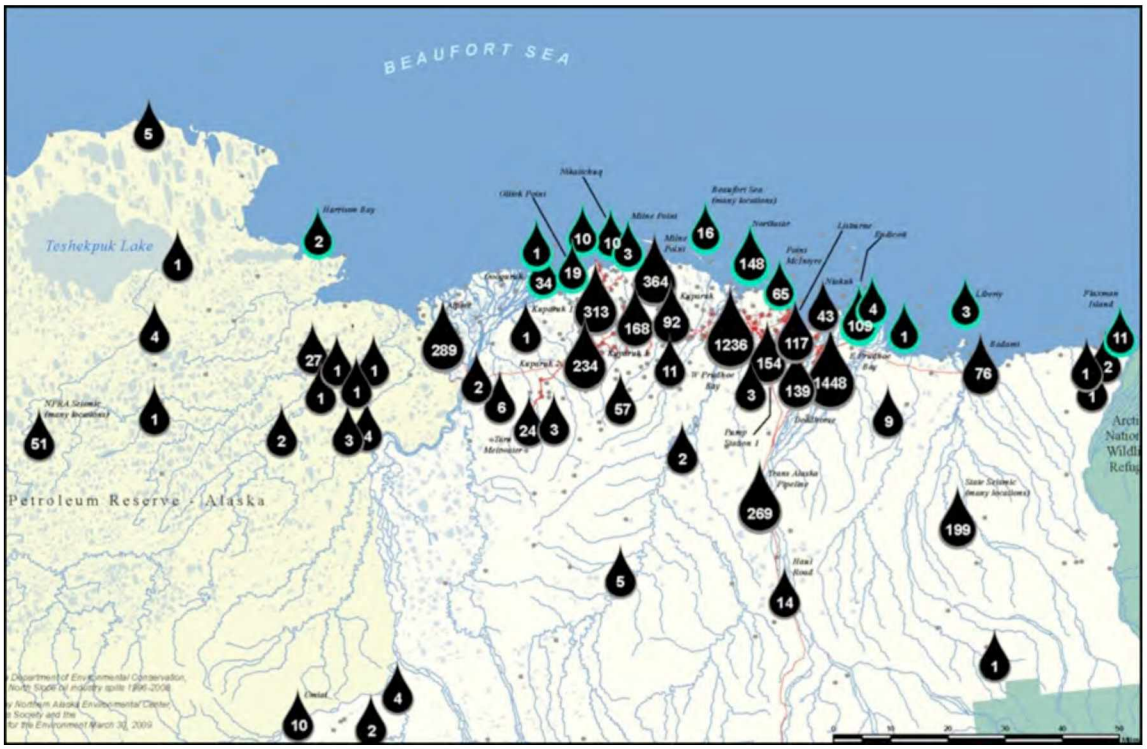

Figure 1.5: Oil and gas industry toxic spills in the Alaska North Slope. Data from 1996 to 2008. Data compiled by Pam Miller, Northern Alaska Environmental Center. Mapping by Doug Tosa, Alaska Center for the Environment. Data from Alaska Department of Environmental Conservation spill database. The size of the black drops is proportional to the number of spills on the sites, ranging from 1 to 1448. Modified after: Center 2011.

Figure 1.6: Damage from coastal storms in Alaska. Flooding in Newtok, Alaska on the Bering Sea coast (a). Credit: Tom Stanley. Erosion damage in Shishmaref, Alaska on the Chukchi Sea coast (b). Credit: Tony Weyiouanna. Source: Workgroup 2008. Flooding in Barrow, Alaska on the Chukchi Sea coast (c). Credit: Grace Reeding. Source: Brunner et al. 2006.

1.2 A Polar Low Process in the Chukchi and Beaufort Seas

In spite of polar lows being infrequent in the CBS, a comma-shaped one was observed in this region (Figure 1.7) on October 9-10, 2009 (Inoue et al. 2010). Its evolution can be seen in Figure 1.7. It had a lifetime of less than 24 hours and a horizontal scale of approximately 600 km by 800 km. Its cycle can be broken down into a developing stage (b), mature stage (c), and dissipating stage (d). The approximate polar low track is illustrated by the colored dots in Figure 1.8, which are at 2-hourly intervals from October 9 at 2200 UTC up to October 10 at 0800 UTC, as obtained from model simulations. Figure 1.9 shows the National Center for Environmental Prediction (NCEP) final analyses (FNL) for sea-level pressure (SLP) and geopotential height at 500 hPa for the times closest to those in Figure 1.7. The synoptic situation during the polar low development from October 8, 2009 to October 10, 2009 as seen from satellite images, FNL analyses and other observational data is summarized in the following paragraphs.

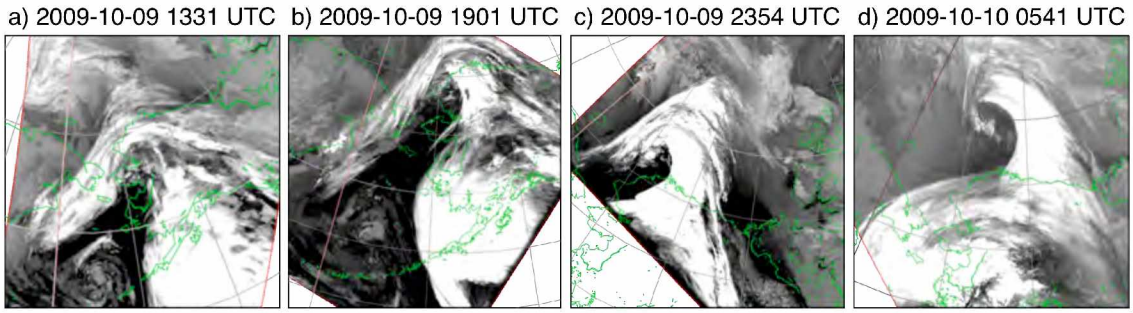

Figure 1.7: Polar low evolution in IR satellite images. Valid for October 9 at 1331 UTC (a), 1901 UTC (b) and 2354 UTC (c) and October 10 at 0541 UTC (d). Sensors are the Advanced Very High Resolution Radiometer (AVHRR) and the Defense Meteorological Satellite Program (DMSP) Operational Linescan System (OLS).

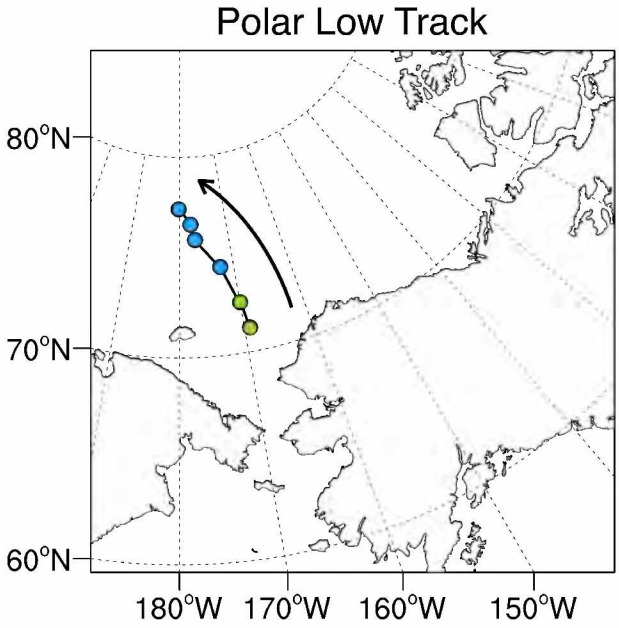

Figure 1.8: Polar low track in the Chukchi Sea. Based on surface wind data obtained from model simulations. Dots represent the approximate location of the closed low at the surface and are displayed at 2-hourly intervals from October 9, 2009 (green) at 2200 UTC to October 10, 2009 (blue) at 0800 UTC. Black arrow represents direction of polar low movement.

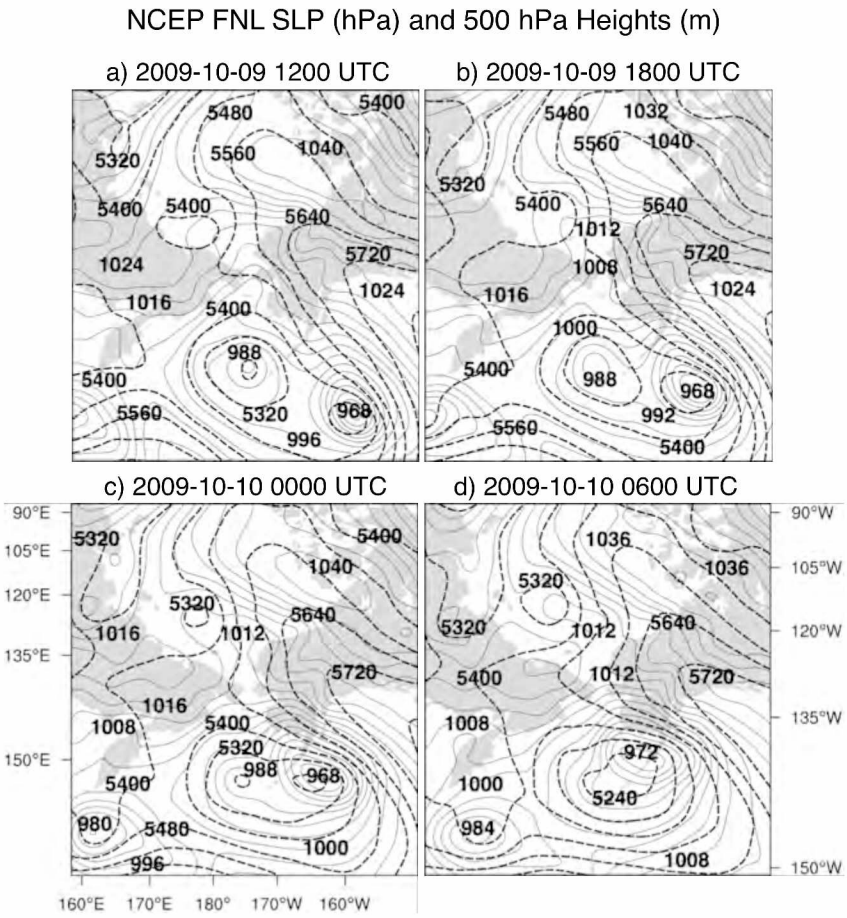

Figure 1.9: Polar low evolution from NCEP FNL. Valid for October 9, 2009 at 1200 UTC (a) and 1800 UTC (b) and October 10, 2009 at 0000 UTC (c) and 0600 UTC (d). Solid lines are SLP contours at 4 hPa intervals. Dashed lines are 500 hPa isohypses at 80 m intervals.

On October 8, preceding the formation of the polar low, an intensifying Aleutian Low (AL) centered just south of the Aleutian chain, deepened to reach a minimum pressure of 966 hPa at 1200 UTC, after which it started losing strength. Associated with this low was a surface trough along the Alaska northern coast and an upper-level (UL) closed low over the eastern Siberian coast. This UL low cut off from the AL towards the end of this day. A strong Beaufort High (BH) could also be seen, with a central pressure

of 1048 hPa. This high-pressure system was being forced to move eastward and to weaken due to the development and movement of the surface and UL troughs. A second and stronger low centered over the NE Pacific (North Pacific Low) could also be seen moving northwestward and strengthened as it approached the Aleutian chain.

As seen from the FNL analyses (Figure 1.9), on October 9, 2009 the AL continued to weaken and the North Pacific Low moved until reaching the Aleutians with a central pressure of ~965 hPa. At this point, the AL had a central pressure of ~986 hPa (Figure 1.9b). All through the day on October 9 the surface trough along the Alaska coast kept developing and advancing towards the eastern Beaufort Sea, causing the BH to retreat. The 500 hPa trough was still present and moved northward positioning itself over the eastern Siberian ocean (Figure 1.9c). In the afternoon the first sign of a "comma" cloud structure started to develop, which became clear around 1800 UTC (Figure 1.7b). At this time the development phase began as the low-pressure center made its way through the Bering Strait and into the Chukchi Sea. Near 0000 UTC on October 10 the closed circulation at the surface could already be seen and the SLP was ~1010 hPa (Figure 1.9c). The dissipating phase started around 0400 UTC as is evidenced by satellite imagery and radiosonde pressure measurements. This phase was characterized by the mesoscale surface low finally cutting off from the synoptic-scale AL and moving northwestward to meet up with the 500 hPa closed low (Figure 1.9d).

Additional evidence for the development and movement of the CBS polar low can be seen from surface observations in Barrow, Alaska (71.287°N, 156.76°W) as shown in Figure 1.10. A significant drop in pressure of ~10 hPa in 24 hours was observed as the trough deepened along the Alaska North Slope as seen in Figure 1.9. A

southerly flow advected warm air and a rapid change in wind direction occurred after the passage of the low.

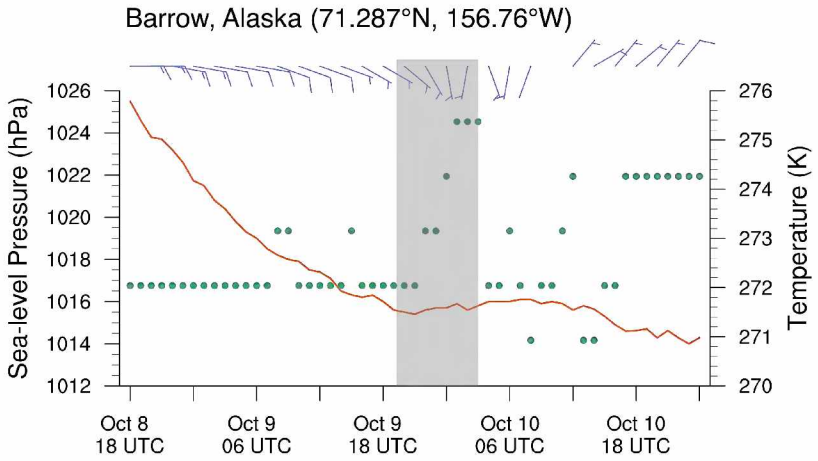

Figure 1.10: Hourly time series of observations in Barrow, Alaska. Coordinates are 71.287°N, 156.76°W. Variables are SLP (hPa; solid line), air temperature at 2 m (K; dots) and wind at 10 meters (m s^{-1}; wind barbs on top). The shaded column represents the time of polar low development.

Finally, sounding profiles obtained by the Japan Agency for Marine-Earth Science and Technology (JAMSTEC) ship expedition R/V MIRAI are shown in Figure 1.11. These observations indicate a dramatic lowering of the tropopause from ~220 hPa (a) to ~460 hPa (b), as well as a very stable lower atmosphere. Below ~800 hPa, all ship soundings indicate a predominance of isothermal or inversion temperature profiles. The inversions were often shallow but strong. The strongest one was observed on October 10, 2009 at 0900 UTC (not shown) from 962 to 950 hPa, with a lapse rate of ~2.8 K km^{-1}.

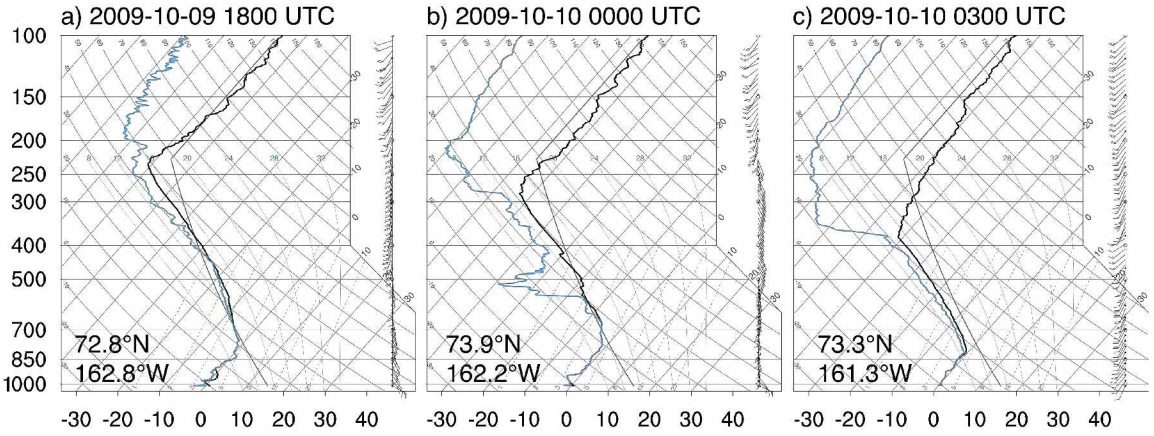

Figure 1.11: Soundings from the R/V MIRAI JAMSTEC expedition. Valid for October 9, 2009 at 1800 UTC (a) and October 10, 2009 at 0000 UTC (b) and 0300 UTC (c). Coordinates at bottom left corners indicate the launching location.

1.3 Motivation and Goals

Polar lows not only have small spatial and temporal scales, but they also happen in regions with limited data coverage. This fact results in a system that not only is hard to forecast, but is also poorly reproduced in coarse reanalysis products (e.g., Condron et al. 2006). Therefore, detailed studies and accurate forecasts must rely on high-resolution simulations to provide a realistic and continuous representation of such systems. On that account, before attempting to conduct detailed analyses of this polar low it is advantageous to determine the model configuration that yields the most realistic results.

Since polar lows are uncommon in the CBS and because of their manifold dynamics, knowledge is very limited about their formation and development in this region. Understanding the mechanisms responsible for their formation and possibly identifying potential precursors would ultimately improve the quality of the forecasts for

such extreme events, which is very important considering the vulnerability of coastal Alaska. Moreover, ship soundings launched in the Chukchi Sea on October 2009 by the JAMSTEC MIRAI expedition provided an unusual opportunity to accurately study the storm profile and to validate the model results. Therefore, the circumstances offer an extraordinary possibility of conducting a reliable case study of this system.

Based on the discussion presented, the main purpose of this work is to investigate the mechanisms responsible for the development of the CBS polar low. However, before that can be accomplished, it is necessary to obtain a high-resolution realistic simulation of the system. This thesis is divided into two parts. The first part covers a series of modeling experiments (Chapter 2) while the second part encompasses a diagnostic analysis of the polar low based on model data (Chapter 3).

Chapter 2: Model Simulations of the Polar Low: Optimization of Model Physics and Validation of Model Results

This chapter presents a description of the mesoscale model used in this study, the general configuration used for the simulations and the results of three sensitivity experiments. Experiment "MP/BL" assesses the sensitivity of the modeled fields to model physics and is presented in Section 2.3. Similarly, experiment "IC/BC" tests the model sensitivity to initial and boundary conditions and is discussed in Section 2.4. Experiment "SN" investigates improvement in results associated with the use of spectral nudging techniques and is presented in Section 2.5. The purpose of these experiments is to determine a model configuration that produces the most realistic simulation of the CBS polar low and to obtain a solid simulation that can be used for further analyses.

2.1 General Model Configuration

In order to achieve the stated goals, we have conducted a series of modeling experiments. They were all performed with version 3.2.1 of the Weather Research and Forecasting (WRF) model on the Advanced Research WRF (ARW) core (e.g., Michalakes et al. 2005; Skamarock et al. 2005; Skamarock and Klemp 2008). WRF is a fully compressible and non-hydrostatic Eulerian model that can be used for both idealized and real data applications. It is a limited area model that can be applied for the Arctic (e.g., Bromwich et al. 2009; Cassano et al. 2011; Mölders et al. 2011). It uses terrain-following vertical coordinates and is integrated on an Arakawa-C horizontal grid. The time integration is done through a third order Runge-Kutta scheme and the model supports one-way and two-way nesting as well as moving nests.

The polar low simulations were initialized on October 8, 2009 at 1200 UTC, approximately 30 hours before the system started to develop. They ran for 60 hours, up to October 11, 2009 at 0000 UTC. Two domains with 18 km (235 x 240 grid points) and 6 km (370 x 370 grid points) grid increments (Figure 2.1a) were set up using a two-way nesting approach. The time steps were 90 s and 30 s, respectively. The initial data was interpolated to 40 vertical levels, with a top pressure of 50 hPa. The physical parameterizations common to all experiments were the Rapid Radiative Transfer Model longwave radiation (Mlawer et al. 1997), Dudhia shortwave radiation (Dudhia 1989), Noah Land Surface Model (Chen and Dudhia 2001), and Grell 3-D cumulus scheme (Grell and Dévényi 2002). All runs were made with sea-surface temperature (SST) updates and fractional sea ice. The sea-ice concentration fields used to force the model were from the same dataset used as initial and boundary (IC/BC) conditions for the other fields. The SST was from the NCEP real-time daily global analyses with a spatial resolution of 0.5° and a temporal resolution of one day.

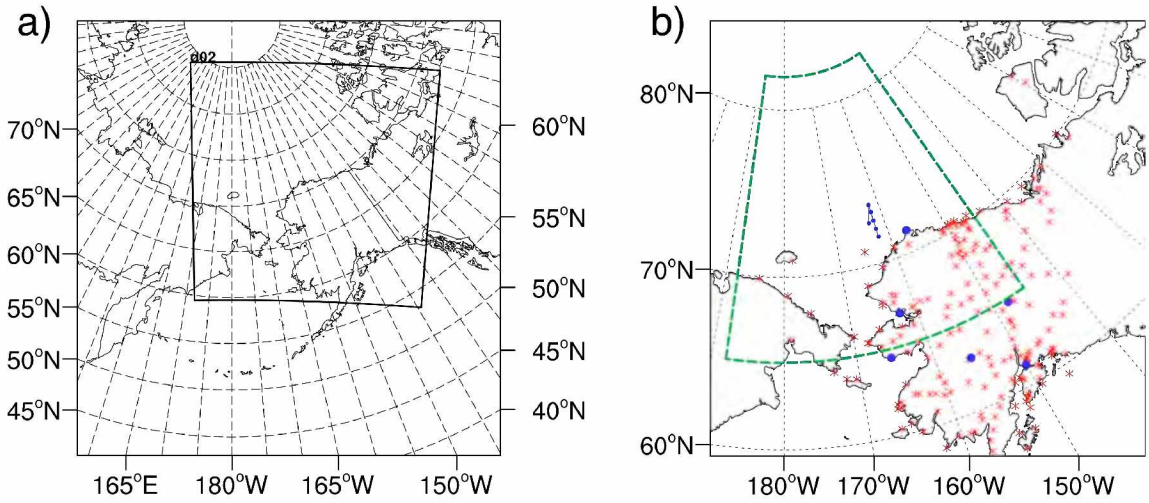

Figure 2.1: Simulation domains and data used for model evaluation. Simulation domains (a) where parent and nested domains have a grid increment of 18 km and 6 km, respectively. Observational data used for model evaluation (b), where red stars represent surface stations and blue dots sounding sites. The green dashed polygon represents the area chosen for validation against QuikSCAT winds.

The first experiment tested the model sensitivity to different microphysics (MP) and boundary layer (BL) parameterizations. The second and third experiments assessed the sensitivity of the results to large-scale forcings, which was done by varying the dataset used to provide IC/BC and by testing various spectral nudging (SN) configurations. Table 2.1 summarizes the configurations that differ among these three experiments. Deviations from the general setup discussed in this section will be clearly stated when applicable. Detailed descriptions specific to each experiment will be provided in the relevant sections.

Table 2.1: Variations in model setup among experiments. The nudging setup "No Temperature" refers to a default nudging configuration for all variables except temperature, and will be discussed in Section 2.5. The final proposed configuration is also given.

	Experiment MP/BL	**Experiment IC/BC**	**Experiment SN**	**Proposed Configuration**
Number of Simulations	13	5	13	1
Initial and Boundary Conditions	ERA-Interim	ERA-Interim; JCDAS; NNRP 1; NNRP 2; FNL	ERA-Interim	ERA-Interim
Microphysics Scheme	Morrison; WSM5; WSM6; WSM3; ETA; Goddard; Thompson; Lin	Morrison	Morrison	Morrison
Boundary Layer Scheme	ACM2; QNSE; MYNN 2.5; MYJ; YSU; MRF	YSU	YSU	YSU
Spectral Nudging Setup	"No Temperature" (see Section 2.5)	"No Temperature"	See Table 2.4	"No Temperature"

2.2 Data and Methods Used to Validate Model Simulations

The modeling experiments presented in Chapter 2 were evaluated against observational data from surface stations, sounding sites and satellite-derived 10-meter winds over the ocean (see Figure 2.1b for the geographical location of these data within the nested domain). In order to quantify the errors and allow for a comparison among

variables, a normalized root mean squared error (NRMSE) was calculated by normalizing the bias to the standard deviation (σ_O) of the observations as given by Eq. 2.1, where N is the total number of points, x_s is the simulated value and x_o the observed value. Root mean squared errors (RMSE) and unbiased RMSE (URMSE) were also used, especially for the evaluation against QuikSCAT data, for which σ_O could not be obtained since the observations are irregularly spaced spatially and temporally.

$$NRMSE = \sqrt{\frac{\sum_{i=1}^{n}\left(\frac{x_{S_i} - x_{O_i}}{\sigma_O}\right)^2}{N}} \qquad \text{Eq. 2.1}$$

The simulations with the smallest errors were deemed best-performing. The evaluation was based on dynamic parameters such as wind speed, wind direction, SLP, and geopotential height. All analyses accounted for a 6-hour spin-up period. The surface analysis over the continent was based on 205 stations located in Alaska, Canada and Russia. These data come from various sources: 167 National Climate Data Center (NCDC) stations; 18 Remote Automated Weather Stations (RAWS); 15 Water and Environmental Research Center (WERC) stations, 3 Bureau of Ocean Energy Management, Regulation and Enforcement (BOEMRE) stations, 1 buoy and 1 well site. The surface analysis over the ocean was based on 12.5 km resolution winds obtained through the QuikSCAT satellite sensor. The area chosen for QuikSCAT evaluation is illustrated by the dashed polygon in Figure 2.1.

The vertical analysis considered profiles from 925 hPa to 300 hPa from seven radiosonde sites, six of which are 12-hourly National Weather Service observations from

Alaska sites located in Anchorage, Barrow, Fairbanks, Kotzebue, McGrath and Nome. The last site is offshore in the Chukchi Sea and is part of the R/V MIRAI (from now on MIRAI) expedition undertaken by JAMSTEC in 2009. The frequency of this data is 3-hourly and each launching time corresponds to a different location. The analysis of the MIRAI data is important for two main reasons: its launching location and its 3-hourly frequency. This provides an unusual opportunity to evaluate the performance of the model when simulating the CBS polar low. The locations and elevations of the sounding sites are given in Table 2.2.

Table 2.2: Sounding station names, coordinates and elevation.

Station Name	**Location**	**Latitude**	**Longitude**	**Elevation**
PABR	Barrow, AK	71.30	-156.77	4.0
PAOT	Kotzebue, AK	66.86	-162.63	5.0
PAOM	Nome, AK	64.50	-165.42	7.0
PAFA	Fairbanks, AK	64.81	-147.86	138.0
PANC	Anchorage, AK	61.16	-150.01	40.0
PAMC	McGrath, AK	62.96	-155.61	103.0
MIRAI	Chukchi Sea	Variable	Variable	18.0
		Time	**Lat**	**Lon**
		2009-10-09 1800 UTC	72.46	-163.02
		2009-10-10 0000 UTC	73.50	-162.00
		2009-10-10 0300 UTC	73.05	-161.98
		2009-10-10 0600 UTC	72.53	-162.02
		2009-10-10 0900 UTC	72.02	-162.03
		2009-10-10 1200 UTC	71.53	-162.01

2.3 Sensitivity to Microphysics and Boundary Layer Parameterizations

MP parameterizations are needed for resolving precipitation processes, water vapor, cloud droplets and ice. According to Wu and Petty (2010), a realistic treatment of cloud and precipitation processes is a critical factor when performing numerical simulations of polar lows. In this study, we consider the sensitivity of WRF simulations of the CBS polar low to eight different MP parameterizations (Table 2.3). The abbreviations listed in Table 2.3 were used to name the simulations according to the MP and BL schemes used, where MORRI-ACM2 refers to the control simulation run with Morrison MP (Morrison et al. 2009) and Assymetric Convective Model version 2 (ACM2; Pleim 2007) BL. Most of the bulk MP schemes available in WRF are single-moment and predict only mixing ratios. In this study, only Morrison and Eta Ferrier (Zhao et al. 1997) are double-moment, which means that they also predict the number concentrations of the species (e.g., Lim and Hong 2009).

Surface forcing is commonly an important factor in the development of polar lows (e.g., Bresch et al. 1997; Pagowski and Moore 2001). Therefore, when attempting to numerically simulate these systems it is also crucial to realistically reproduce the lower atmosphere and BL processes. This goal is achieved through BL parameterizations, which account for vertical diffusion and for heat, moisture, and momentum fluxes. The control simulation in this experiment was run with ACM2. Five additional parameterizations were considered in the sensitivity study, as listed in Table 2.3.

Table 2.3: Parameterizations used in experiment "MP/BL." Names (left), reference (middle) and the abbreviations used in the text and figures (right).

	Scheme	Reference	Abbreviation
Microphysics Schemes	Morrison	Morrison et al. 2009	MORRI
	WRF Single Moment 6-class	Hong and Lim 2006	WSM6
	WRF Single Moment 5-class	Hong and Lim 2006	WSM5
	WRF Single Moment 3-class	Hong et al. 2004	WSM3
	Eta Ferrier	Zhao et al. 1997	ETA
	Goddard	Tao and Simpson 1993	GODD
	Thompson	Thompson et al. 2004	THOMP
	Lin	Chen and Sun 2002	LIN
Boundary Layer Schemes	Asymmetric Convective Model version 2	Pleim 2007	ACM2
	Quasi-Normal Scale Elimination	Sukoriansky et al. 2006	QNSE
	Mellor-Yamada Nakanishi and Niino Level 2.5	Nakanishi 2001	MYNN2.5
	Mellor-Yamada-Janjic	Mellor and Yamada 1982; Janjic 2000	MYJ
	Yonsei University	Hong et al. 2006	YSU
	Medium-Range Forecast	Hong and Pan 1996	MRF

For a synoptic-scale evaluation of the modeled fields we can consider the domain-averaged NRMSE values for the 13 simulations in this experiment (Figure 2.2). We can see that the largest spread among simulations is seen for wind speed, where WSM3-ACM2 presents the smallest errors. However, the smallest errors for all other variables correspond to the MORRI-YSU simulation. For a meso-scale evaluation we can consider the NRMSE values averaged over the two sounding sites closest to the Chukchi Sea (Figure 2.3), which are PABR (Barrow, Alaska) and MIRAI (JAMSTEC ship sounding). From Figure 2.3, we can see that MORRI-YSU presented the smallest errors for wind speed and direction, and the second smallest errors for SLP and geopotential height where it was preceded by MORRI-MYJ. When looking specifically at the MIRAI site (not shown), there is a considerable spread in performance among simulations and MORRI-YSU again presents the smallest error values. This evaluation based on surface stations and sounding sites indicates that overall MORRI-YSU yielded the least errors and therefore the most realistic simulation over land.

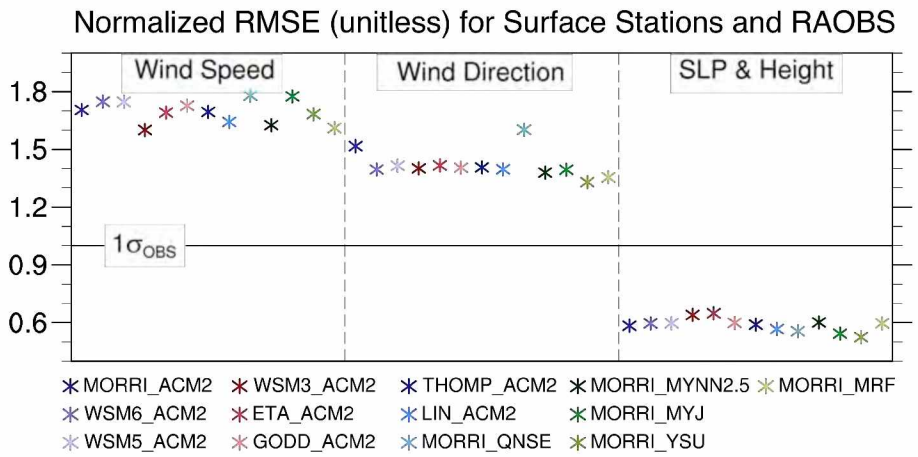

Figure 2.2: Synoptic-scale evaluation for experiment "MP/BL." NRMSE averaged over 205 surface stations and 7 sounding sites over time. Variables are wind speed (left), wind direction (middle), and an average of SLP and geopotential height (right).

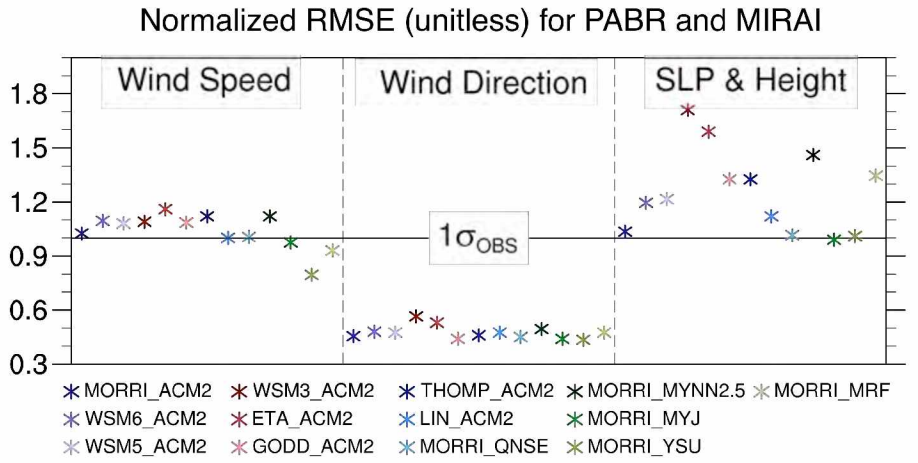

Figure 2.3: Meso-scale evaluation for experiment "MP/BL." NRMSE for PABR and MIRAI sounding sites. Variables are wind speed (left), wind direction (middle), and an average of SLP and geopotential height (right).

The model evaluation against 10-meter winds over the ocean is also a meso-scale evaluation since it is centered on the Chukchi Sea. In this case, the best-performing

simulations were MORRI-YSU for wind speed and MORRI-ACM2 for wind direction (not shown). Unlike what is seen for the evaluation against surface stations and sounding sites, the spread among simulations is largest for wind direction when evaluating the performance against QuikSCAT winds. This finding is due to simulation errors in the meridional component of the wind, as can be observed in Figure 2.4. When considering all times and all data points available from the QuikSCAT observations within the area selected for the evaluation, the correlations for zonal wind range from 0.89 to 0.91 among the simulations, while for meridional wind they are as low as 0.66 and only as high as 0.69. The biases in the simulation of the wind components are similar among the simulations and are illustrated for MORRI-YSU in Figure 2.4, which considers all available observations within a 24-hour period starting on October 9 at 1200 UTC and covers the developing and dissipating stages of the low. Unfortunately, there is a large gap in the data during the polar low mature stage, hindering any evaluation at those times.

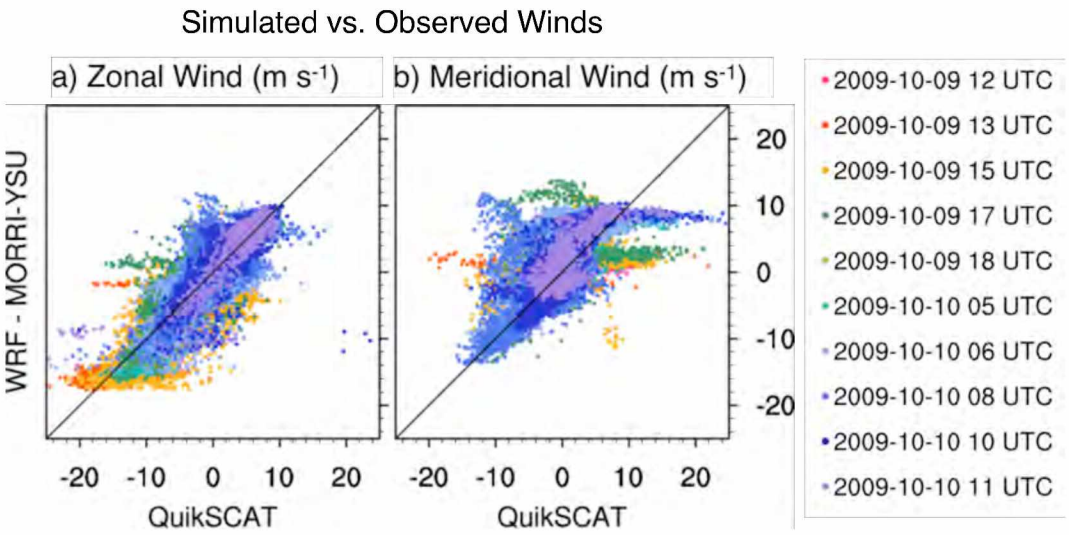

Figure 2.4: Simulated vs. observed winds for simulation MORRI-YSU. Shown separately for zonal (a) and meridional (b) components. Different colors represent different observation times as indicated by the legend. Axes vary from -25 to 25 m s^{-1}.

The evaluation presented indicates Morrison (MORRI) microphysics and Yonsei University (YSU) boundary layer as the best-performing physical schemes. These results are different, but complementary to those presented by Wu and Petty (2010). They also investigated the sensitivity of polar low simulations to MP parameterizations in WRF. Differently from our study, their evaluation focused on thermodynamic parameters such as precipitation and cloud top temperatures. They considered five MP schemes (including Morrison) and found that the WRF Single Moment 6-class (WSM6; Hong and Lim 2006) provided the most realistic results. This difference in results might be due to the different criteria of evaluation, since our study is focused on dynamic parameters. The main difference between Morrison and most other MP schemes is that it is a double-moment scheme, and therefore predicts not only mixing ratios but also number concentrations.

With regard to the BL sensitivity results, the main difference between YSU and the other BL schemes is that it explicitly resolves entrainment processes at the top of the BL (Hong et al. 2006). The fact that it performed consistently better than the other schemes might indicate the importance of entrainment processes for the case being simulated.

2.4 Sensitivity to Initial and Boundary Conditions

Regional models require IC and BC to be defined, which are usually obtained from reanalysis products or global model outputs. This IC/BC experiment consists of five simulations. In each of them, different datasets were used as large-scale forcing for the model. The datasets are 6-hourly and differ in their horizontal and vertical resolution, model physics and data assimilation techniques, which causes them to yield somewhat different products. These five datasets are:

1) European Re-Analysis (ERA) Interim, produced by the European Center for Medium-Range Weather Forecasts (ECMWF) with T255 resolution (approximately 0.7°x 0.7°) and available in 37 vertical levels, from 1989 to present;

2) Japanese Meteorological Agency (JMA) Climate Data Assimilation System (JCDAS) produced by the JMA in collaboration with the Central Research Institute of Electric Power Industry (CRIEPI) with T106 resolution (approximately 1.125°x 1.125°) and available in 40 vertical levels, from 2005 to present;

3) NCEP and National Center for Atmospheric Research (NCAR) Reanalysis Project (NNRP 1) produced by NCEP in collaboration with NCAR, with T62 resolution (approximately 2.5°x 2.5°) and available in 28 vertical levels, from 1948 to present;

4) NCEP and U.S. Department of Energy (DOE) Reanalysis Project 2 (NNRP 2) which is a similar product to NNRP 1, but with updated parameterizations and corrections to known errors, available from 1979 to present; and

5) NCEP final analyses (FNL) produced operationally by NCEP, with 1°x1° resolution and available in 26 vertical levels, from 1999 to present.

Figure 2.5a shows the domain-averaged NRMSE values considering all surface stations and sounding sites. It is clear from this synoptic-scale evaluation that the simulation run with ERA as IC/BC provides the most realistic results in almost all instances, being 1.3 σ for wind direction and 0.5 σ for SLP and geopotential height. For wind speed, the JCDAS simulation shows a slightly smaller error than the ERA simulation. The highest error is seen for NNRP 1, where the wind speed mean NRMSE is close to 2 σ. The meso-scale evaluation based on the PABR and MIRAI sounding data is shown in Figure 2.5b. It indicates FNL and ERA as the best-performing large-scale forcings. In this evaluation, we can observe a large spread in error values for wind speed and the average of SLP and geopotential height, with differences of up to ~1 σ among the simulations.

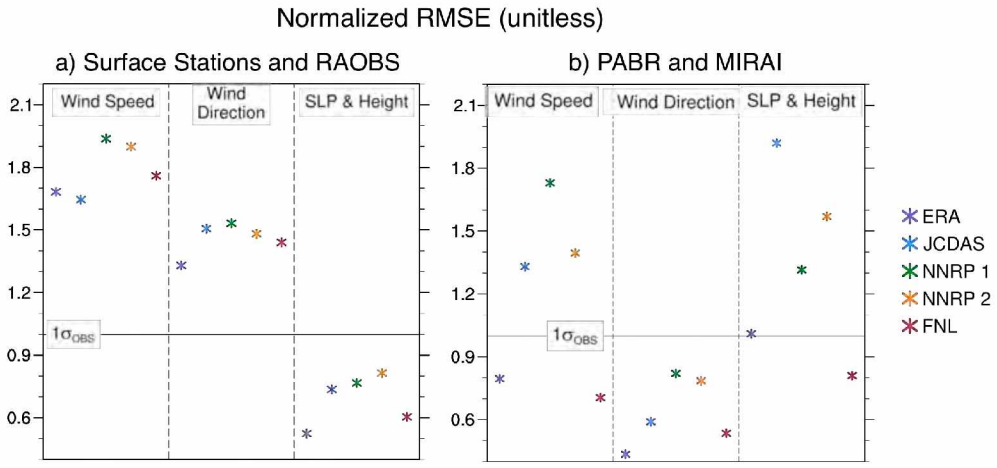

Figure 2.5: Synoptic- and meso-scale evaluations for experiment "IC/BC." NRMSE averaged over 205 surface stations and 7 sounding sites over time (a). NRMSE for PABR and MIRAI sounding sites (b). Variables are wind speed (left), wind direction (middle), and an average of SLP and geopotential height (right).

The meso-scale evaluation of modeled surface winds over the ocean against QuikSCAT data shows a similar spatial distribution of errors among the simulations. This fact is illustrated in Figure 2.6, which shows the wind speed error for the ERA (a) and NNRP 2 (b) simulations for each 12.5 km observation point within the polygon in Figure 2.1. The evaluation time is October 9, 2009 at 1500 UTC, which was chosen for having a larger number of points available for evaluation from the QuikSCAT satellite swath (Figure 2.6c). A temporal average of error values points again to the ERA simulation as the best-performing one, while the largest errors are found for the NNRP 1 and NNRP 2 simulations. Based on the results presented, ERA seems to be the best-performing large-scale forcing dataset, followed by FNL and JRA.

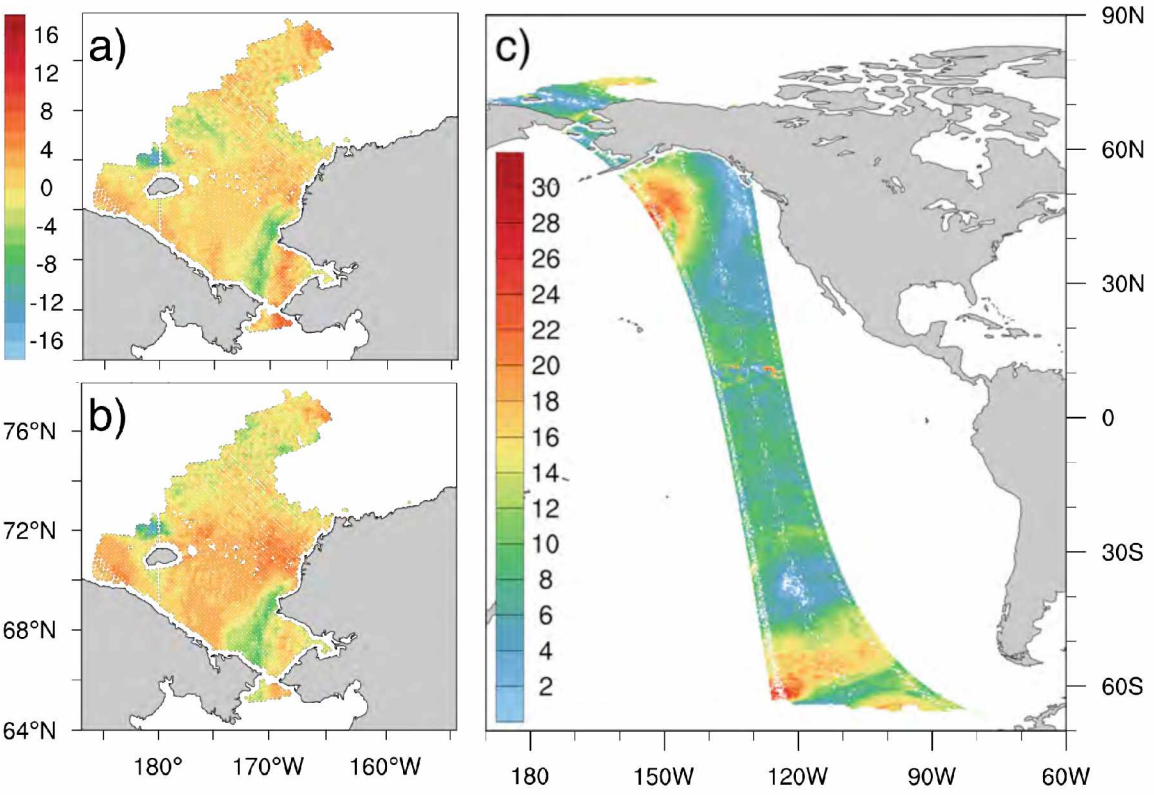

Figure 2.6: Wind speed errors and QuikSCAT wind speed. Unit: m s^{-1}. Errors are for the ERA (a) and NNRP 2 (b) simulations based on the QuikSCAT swath started on October 9, 2009 at 14:18 UTC (c).

2.5 Sensitivity to Spectral Nudging Techniques

This sensitivity experiment tests for an improvement in performance associated with the use of SN techniques. The term "nudging" refers to a category of four-dimensional data assimilation (Stauffer and Seaman 1990). Up to version 3.1, WRF allowed only two kinds of nudging: observational nudging and grid nudging (also called analysis nudging). Since then, a third one was implemented called spectral nudging.

In the case of observational nudging, observations are used to estimate the model error and then define relaxation terms that aim at reducing these errors. A radius of

influence determines how much each observation point will impact the surrounding grid points. On the other hand, for grid nudging and for SN the model fields are nudged at every grid point towards an analysis. The nudging term is once more dependent on the error between the model and the analysis and is an artificial tendency term added to the prognostic equations (e.g., Stauffer and Seaman 1990). What is exclusive in SN is the ability to relax only the long waves in the spectrum towards the analysis (Kanamaru and Kanamitsu 2007). Nudging only the larger scales in a parent domain is particularly advantageous because it still allows the model to freely develop small-scale variability in the nest (Miguez-Macho et al. 2004).

Previous studies have found SN to be a useful technique for various applications, including the simulation of polar lows (e.g., Zahn et al. 2008). Using a regional climate model, Zahn et al. found that their polar lows did not even develop when SN was not applied. As other examples, the use of SN was also found to yield better results for wind hindcasts (e.g., Weisse and Feser 2003), cloudiness simulations (Meinke et al. 2006) and climate downscaling (e.g., Lo et al. 2008). The sensitivity of simulated fields to different user-defined SN parameters has also been previously studied, and the parameters often considered are nudging strength and vertical extent (e.g., Weaver et al. 2002; Lo et al. 2008; Alexandru et al. 2009).

These previous studies have either focused on the role of SN for polar low simulations, or on the model sensitivity to various nudging parameters. No work has been done on the sensitivity of polar low simulations to different nudging parameters.

Such is the topic of this experiment, with the main purpose of correcting biases that were identified in the simulation when no nudging was present.

Several user-specified parameters control SN in WRF. Depending on the configuration chosen, the simulations may yield fairly different results. For example, the elimination of nudging below a specified vertical level may be useful to limit the assimilation of coarse resolution analyses that may inhibit or not capture the simulation of some features (e.g., Deng et al. 2007). With that in mind, this experiment analyzes 13 simulations with different nudging setups. The parameters varied are duration, frequency, strength and vertical extent. The experiment is based on a default simulation that is built up from the default WRF nudging configurations. This default run consisted of nudging only the parent domain at all vertical levels and at every time step during the 60 simulation hours. WRF allows the user to nudge up to four variables: horizontal wind, water vapor mixing ratio, potential temperature and geopotential height. All allowed variables were nudged for the "Default" simulation. The nudging coefficient (or strength) was 3×10^{-4} s^{-1}, which represents a timescale of ~56 minutes. Only spatial scales with wave number larger than three were nudged. An additional 11 simulations test the model sensitivity to SN parameters. Finally, a simulation with no nudging was also included in order to assess the general improvements when nudging is applied. Table 2.4 presents a description of the simulations, listing only the specifications that differ from "Default."

Table 2.4. Spectral nudging configurations. Naming and description of the spectral nudging configurations used for the 13 simulations in this experiment. Note that only the settings that differ from the default setup are listed. The colors correspond to those used in Figures 2.7 and 2.8.

Simulation Name	**Modification from Default Setup**
No Nudging	No Nudging
Default	Default Setup
1/2 Duration	Duration = 30 hours
1/3 Duration	Duration = 20 hours
1/2*Frequency	Frequency = 3 minutes
1/4*Frequency	Frequency = 6 minutes
1/10*Frequency	Frequency = 15 minutes
1/3 Strength	Coefficient = 1×10^{-4} s^{-1} ~166 minutes
2/3 Strength	Coefficient = 2×10^{-4} s^{-1} ~83 minutes
4/3 Strength	Coefficient = 4×10^{-4} s^{-1} ~42 minutes
No water vapor	No mixing ratio nudging
No temperature	No temperature nudging
No boundary layer	No nudging in boundary layer

The analysis performed for this experiment is similar to the one performed for the MP/BL and IC/BC experiments in Sections 2.3 and 2.4. The synoptic-scale evaluation is based on Figure 2.7. It indicates a relatively small spread, but a general improvement in performance when nudging is applied, except for the simulations where the duration of nudging is limited ("1/2 Duration" and "1/3 Duration"). This overall improvement associated with SN is especially evident for wind speed (left panel). Duration was the most sensitive parameter, where shorter duration yielded larger errors. No sensitivity was

found to the frequency of nudging, and the sensitivity to strength and vertical extent was very low and therefore not conclusive.

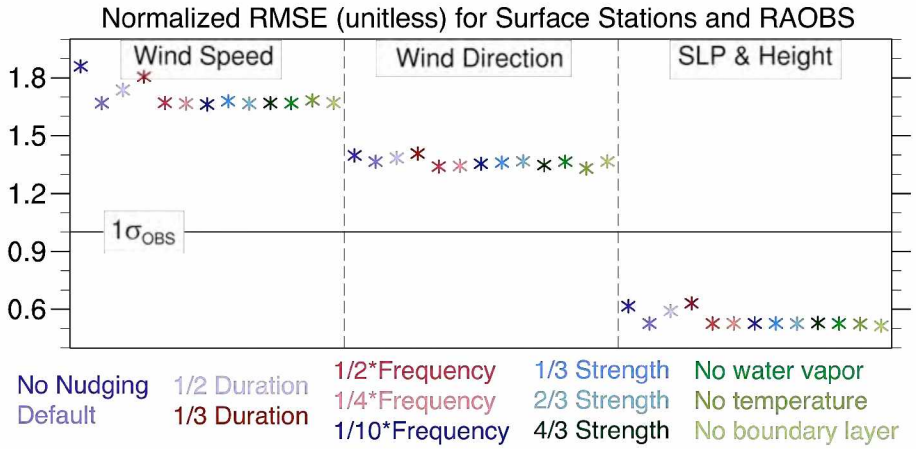

Figure 2.7: Synoptic-scale evaluation for experiment "SN." NRMSE averaged over 205 surface stations and 7 sounding sites over time. Variables are wind speed (left), wind direction (middle), and an average of SLP and geopotential height (right).

The meso-scale evaluation based on QuikSCAT winds also indicated an overall improvement in performance when SN was applied (Figure 2.8). The "1/3 Duration" simulation interestingly presented the smallest errors for wind speed, but still the largest errors for wind direction. The next best-performing simulation is "No Temperature" which produced the smallest RMSE values for both wind speed and wind direction. The improvement associated with the use of SN is illustrated spatially in Figure 2.9. For "No Nudging" (left), the closed circulation associated with the polar low could not be seen on October 9, 2009 at 2300 UTC. However, when nudging is applied (right) the circulation

developed. Another example that illustrates the difference between simulations with and without SN can be seen in Figure 2.10, which shows the temperature, humidity and wind profiles through the polar low during its mature stage on October 10, 2009 at 0000 UTC. Note that the dry layer observed at 500 hPa was captured by the simulation with nudging (green) at 400 hPa, but was not present in the simulation without nudging (blue). On the other hand, "No Nudging" captured the southeasterly winds between 500 hPa and 250 hPa well, while the simulation with nudging simulated south winds. Both simulations were still able to capture the veering near the tropopause from 300 hPa to 150 hPa.

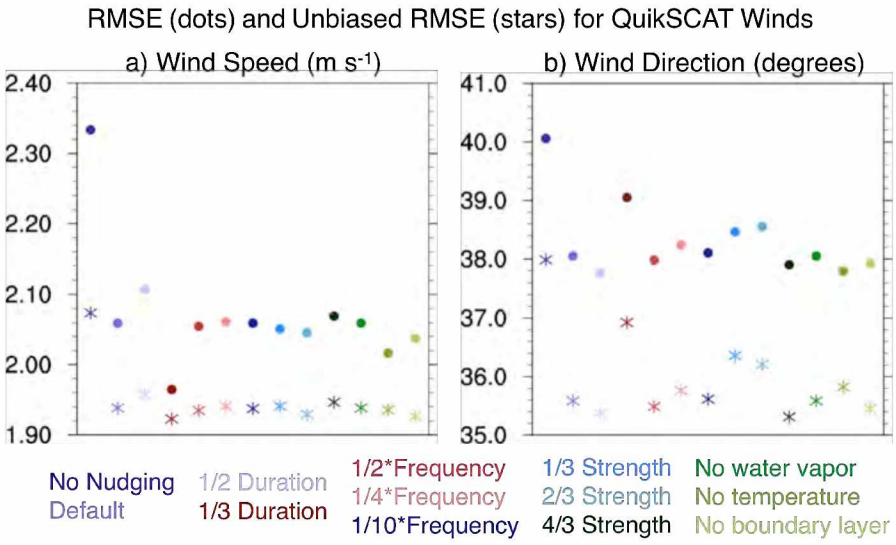

Figure 2.8: Meso-scale evaluation for experiment "SN." RMSE (squares) and URMSE (triangles) for the 13 simulations (horizontal axis) calculated against QuikSCAT ocean winds. Wind speed (left), unit: m s^{-1}. Wind direction (right), unit: degrees.

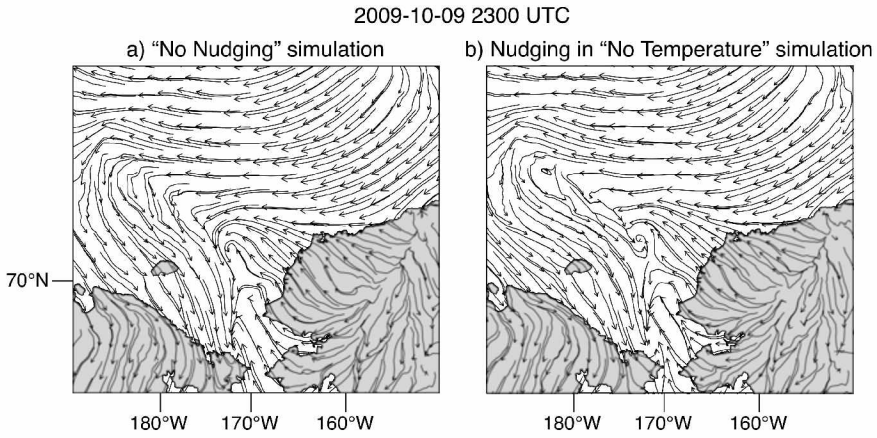

Figure 2.9: Nudging vs. non-nudging polar low simulation. Wind circulation at 10 m. Valid for October 10, 2009 at 2300 UTC. For simulations "No Nudging" (a) and "No Temperature" (b).

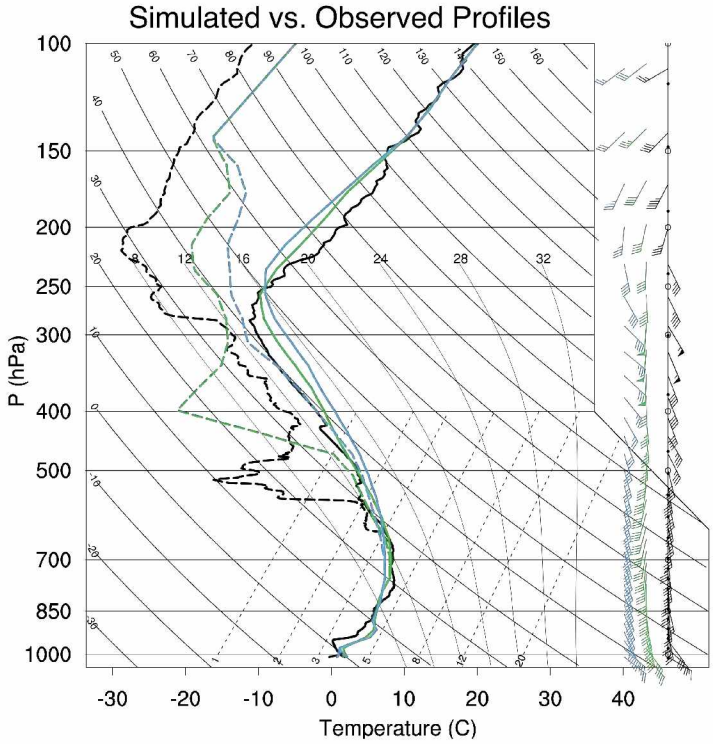

Figure 2.10: Skew-T Log-P plot at 73.9°N, 162.2°W. Valid for October 10, 2009 at 0000 UTC. Profiles from observed data (black; MIRAI sounding) and simulated data from "No Temperature" (green) and "No Nudging" (blue) simulations. Wind barbs are in m s^{-1}. Vertical axis is pressure (hPa) and horizontal axis is temperature (°C).

2.6 Proposition and Validation of Optimized Model Configuration

Once all sensitivity experiments had been completed, we were able to propose a model configuration that would yield the most reliable and realistic results when attempting to simulate the CBS polar low. This configuration consists of choosing the Morrison MP and YSU BL, using ERA-Interim as large-scale forcing and performing nudging only on the larger scales and on the parent domain, during all simulation hours. This configuration is the one used for the following experiments and analyses in this thesis, unless otherwise stated.

In this section, we test whether the proposed model configuration can be used to realistically simulate other polar low cases in the CBS region. The case being simulated is that of a polar low in the Chukchi Sea in early fall 1985 (Fett 1992; Rasmussen and Turner 2003). The validation is done against the discussion, satellite images and analyses provided by Rasmussen and Turner (2003) based on the research conducted by Fett (1992). This case was chosen for being the only published record of a polar low in the CBS region before 2009 for which satellite imagery and analyses were available. It developed between October 11-13, 1985 and dissipated on October 14, 1985. It was a cold-core polar low with a spiraliform cloud structure of mainly open cells (Figure 2.11b). The following description is based on that of Rasmussen and Turner (2003).

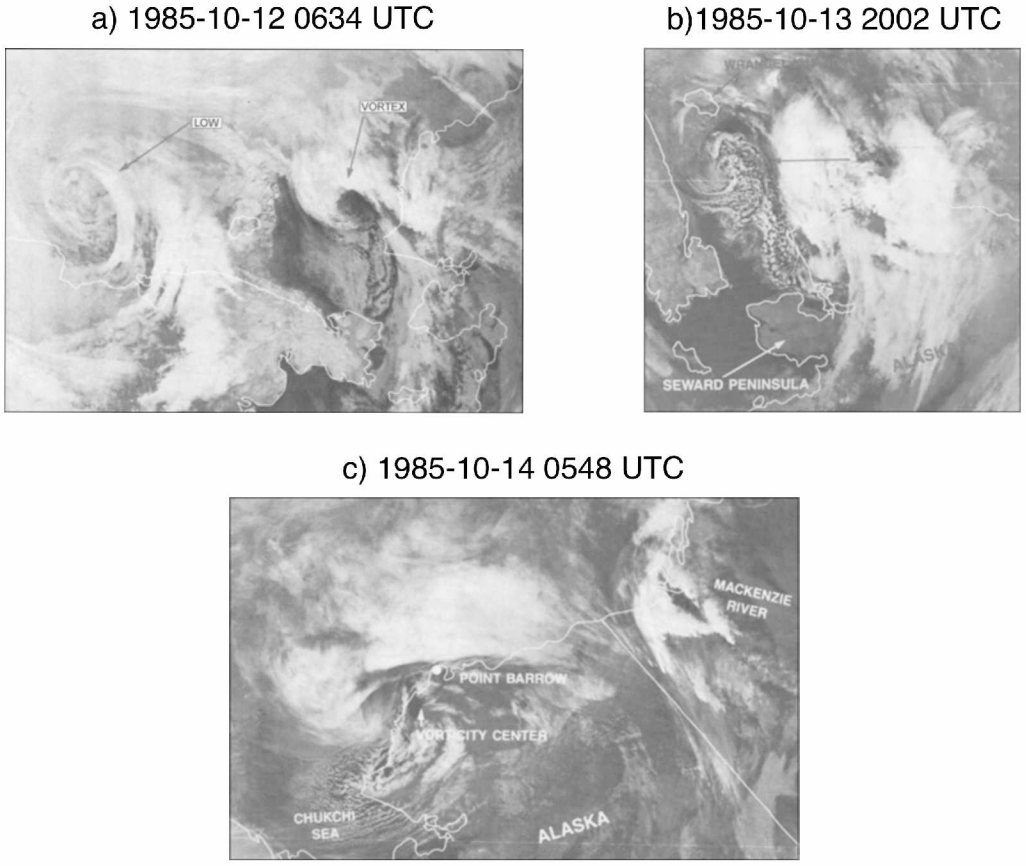

Figure 2.11: Evolution of the 1985 polar low from satellite images. DMSP IR images valid for October 12, 1985 at 0634 UTC (a), October 13, 1985 at 2002 UTC (b) and October 14, 1985 at 0548 UTC (c). Originally from Fett (1992); obtained from Rasmussen and Turner (2003).

The early sign of a possible mesocyclone development could be first identified on October 11 by a small cloud vortex underneath an UL cold low. These features could still be seen on October 12, along with a second vortex over the Chukchi Sea associated with an UL trough (Figure 2.11a and Figure 2.12a). However, the complete storm development only occurred on October 13. By the end of this day (Figure 2.11b and Figure 2.12b) the polar low had reached its mature phase and was vertically aligned with

the 500 hPa cold low, which had temperatures as low as 228 K. On the satellite image in Figure 2.11b, the polar low is the spiraliform circulation west of the convective cloud shield. On October 14 around 0000 UTC and near Barrow, Alaska the 1985 polar low came upon a U.S. Coast Guard icebreaker called *Polar Sea* which reported winds of 60 knots (~30 m/s) and a rapid pressure decrease right after having received a forecast for undisturbed weather. This inaccurate forecast illustrates the difficulty of capturing the rapid onset of such small-scale systems and reaffirms the importance of being able to identify possible preceding features, such as an UL cold low tracking along with a surface vortex. The storm dissipation took place on October 14, 1985 when the polar low and the deep convective cloud formation began to merge (Figures 2.11c and 2.12c).

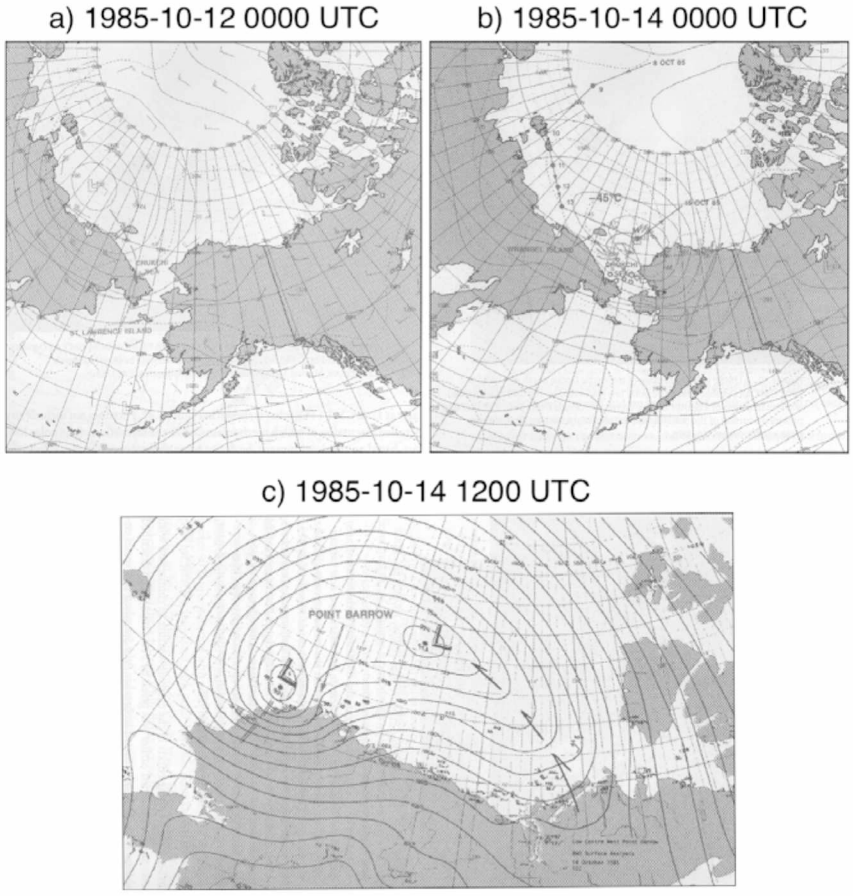

Figure 2.12: Analysis charts for the 1985 polar low. 500 hPa analyses valid for October 12, 1985 at 0000 UTC (a) and October 14, 1985 at 0000 UTC (b). Surface analysis valid for October 14, 1985 at 1200 UTC (c). Originally by Fett (1992); obtained from Rasmussen and Turner (2003).

The WRF simulation for this case was initialized on October 10, 1985 at 1200 UTC and ran for 108 hours up to October 15 at 0000 UTC. This simulation was significantly longer than the one for the 2009 case (which ran for 60 hours) because some important features that preceded its formation were identified two days before the onset, which took place on October 13, 1985. Aside from that, the only difference between the 1985 and the 2009 simulations is the dataset used as large-scale forcing. The ERA-

Interim dataset, which was used for the 2009 case, is not available for 1985. Therefore, the model was initialized with ERA-40 data (Uppala et al. 2005), which is the predecessor of ERA-Interim. This dataset was also produced by ECMWF. It has a T159 resolution (approximately 1.125° x 1.125°) and is available in 24 vertical levels, from 1957 to 2002. It uses a three-dimensional variational assimilation system as opposed to a four-dimensional one, which is used by the more recent ERA-Interim.

Overall, the development of the 1985 polar low was captured well by the WRF simulation both at the surface and at upper levels. On October 12, we can see the two cloud systems (Figure 2.13a) beneath the cold low at 500 hPa (Figure 2.14a). The center of this low was to the NW of Wrangel Island and presented a temperature of ~228 K. The two cloud systems were associated with two low-pressure centers that showed a closed circulation at the surface (Figure 2.15a). On October 13, these two cloud systems and the 500 hPa cold low moved eastward (Figure 2.13b and Figure 2.14b) and the two low-pressure centers merged (Figure 2.15b). On October 14, we can also see the merging of the two surface vortices (Figure 2.15c), followed by that of the two cloud structures (Figure 2.13c), signaling the start of the dissipating stage. As was perceived by the icebreaker *Polar Sea*, the low-pressure center reached Point Barrow, Alaska on October 14 near 0000 UTC as the mesocyclone moved through the Chukchi Sea towards the NW Alaska coast. At this point, the UL cold low had caught up with the surface circulation and the system was vertically stacked.

We can also clearly notice that although the large shield of convective clouds is well captured in the outgoing longwave radiation (OLR) field (Figure 2.13), the same is

not true for the open-cell spiraliform cloud structure of the polar low. This fact might be due to the small scale and fine structure of this system, which are very different from the 2009 comma-shaped low after which the model configuration was determined.

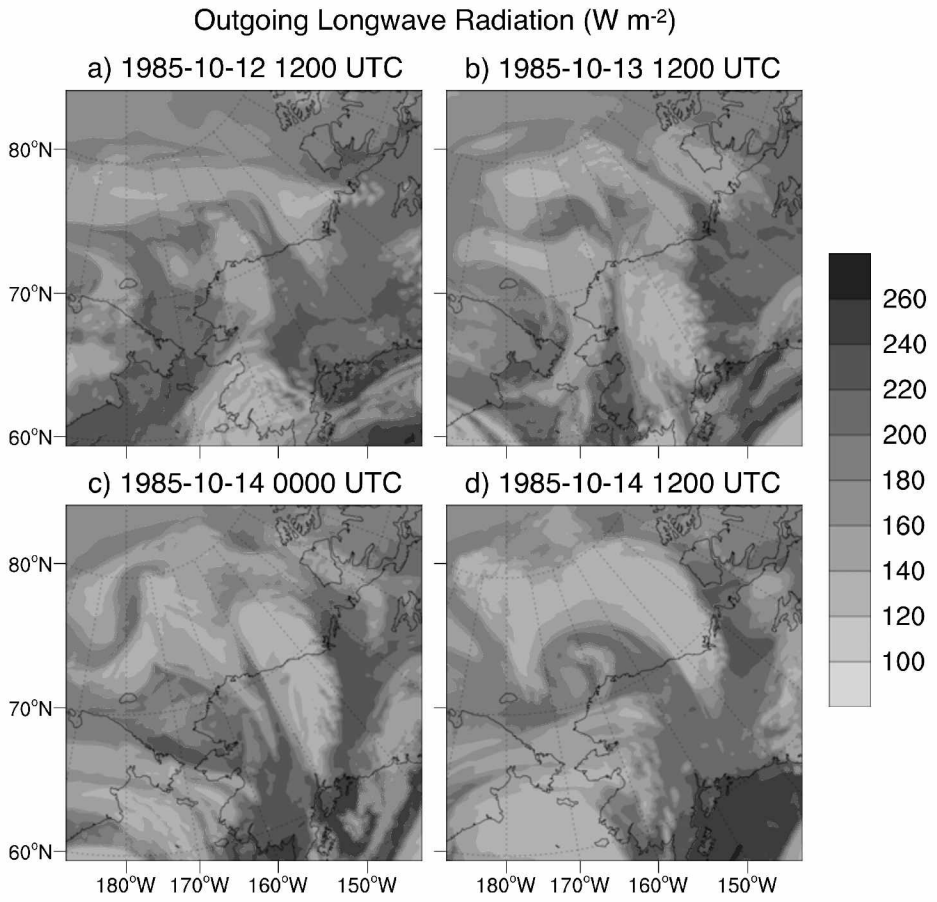

Figure 2.13: Modeled OLR for 1985 polar low. Valid for October 12, 1985 at 1200 UTC (a), October 13, 1985 at 1200 UTC (b), October 14, 1985 at 0000 UTC (c) and 1200 UTC (d). Unit: W m^{-2}.

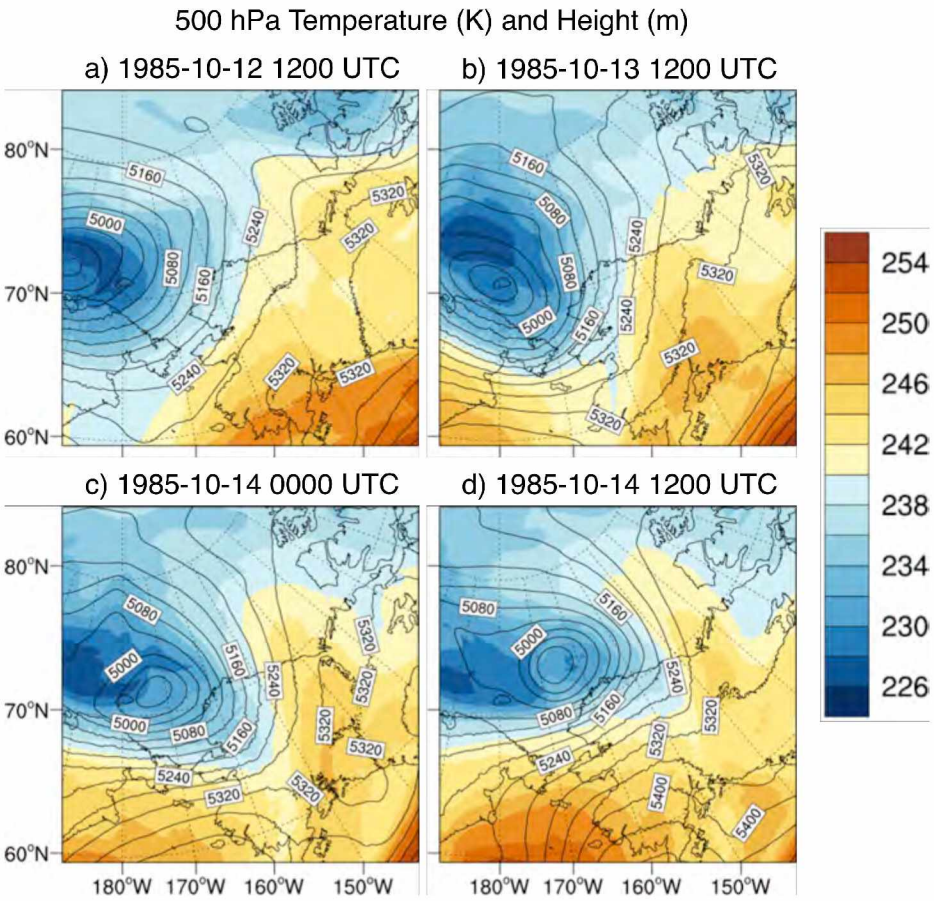

Figure 2.14: Modeled 500 hPa temperature and heights for 1985 polar low. Valid for October 12, 1985 at 1200 UTC (a), October 13, 1985 at 1200 UTC (b), October 14, 1985 at 0000 UTC (c) and 1200 UTC (d). Temperature (shaded), unit: K. Height (black contours), unit: m.

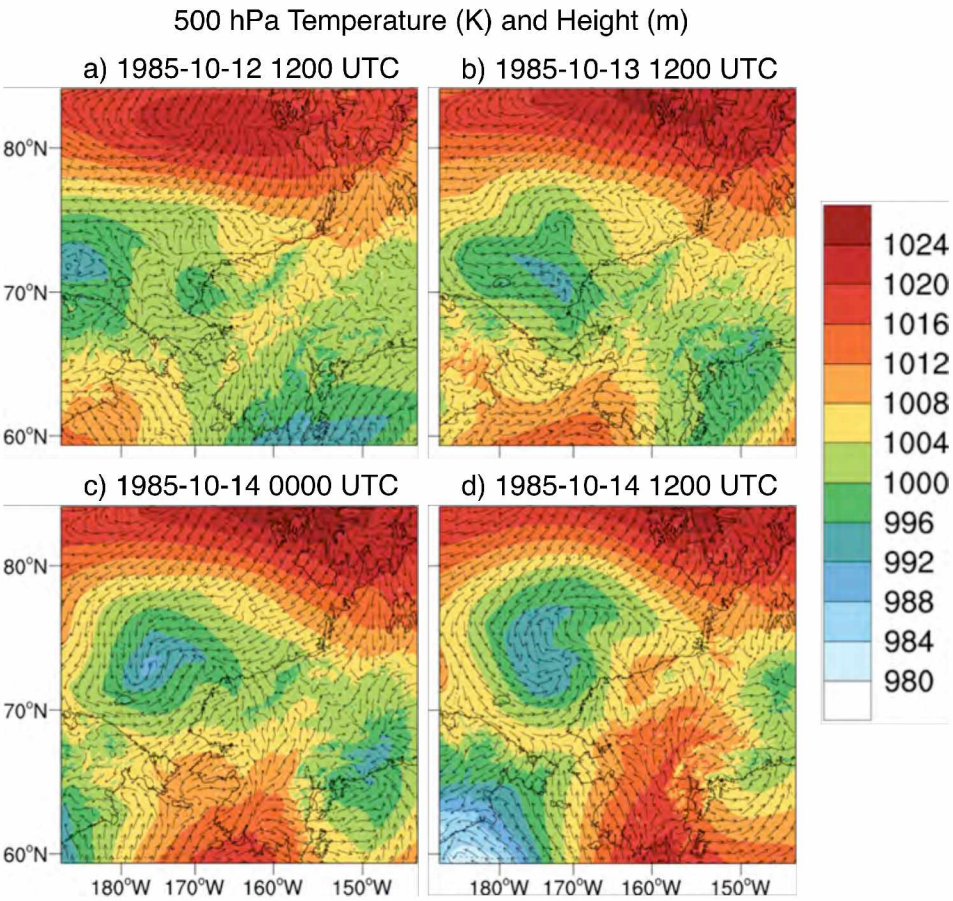

Figure 2.15: Modeled SLP and surface wind field for 1985 polar low. Valid for October 12, 1985 at 1200 UTC (a), October 13, 1985 at 1200 UTC (b), October 14, 1985 at 0000 UTC (c) and 1200 UTC (d). Unit: hPa.

The icebreaker *Polar Sea* was in the Chukchi Sea near Barrow when it reported winds of 30 m s^{-1}. Since its exact location is unknown, let us consider the time series for Barrow, Alaska (Figure 2.16) in order to evaluate the model simulation of wind speeds. The model captured well the evolution of wind speeds for most of the time series, except for two peaks in the observed data. These peaks are seen on October 12, 1985 at 1400

UTC and early on October 14, 1985 from 0200 UTC to 0900 UTC. The mean bias for this time series is -0.4 m s^{-1} and the RMSE is 3 m s^{-1}.

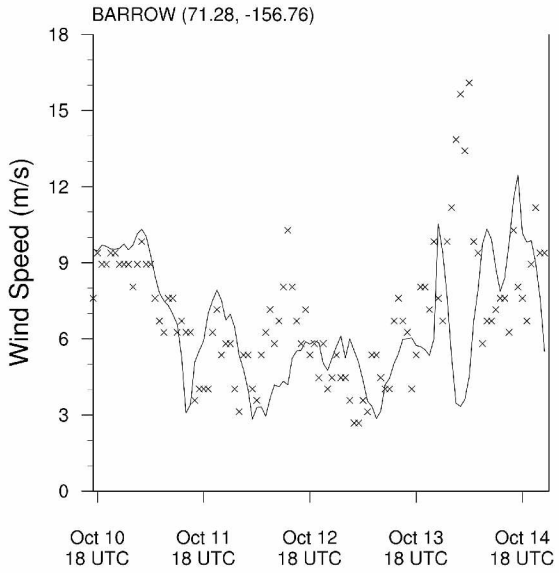

Figure 2.16: Wind speed time series in Barrow, AK. Data is in 1-hourly intervals from October 10, 1985 at 1800 UTC up to October 15, 1985 at 0000 UTC. Modeled (solid line) and observed (stars) data. Unit: m s^{-1} .

We can conclude from this brief analysis that the model configuration chosen for simulating the CBS polar low can also realistically reproduce the surface and UL fields of a very different case in the same region. The only clear inaccuracies found in this study pertained to the OLR fields and to strong wind events observed in Barrow. This evaluation validates the results obtained in the previous chapters and suggests that they can be employed when attempting to simulate other polar low cases in the region of the CBS.

Chapter 3: Analyzing the Chukchi and Beaufort Seas Polar Low

The discussion presented in this chapter has the main purpose of identifying the chief mechanisms responsible for the development of the CBS polar low. Three hypotheses were tested, in which we considered the role of surface forcings (Section 3.3), potential vorticity anomalies (Section 3.4) and baroclinicity (Section 3.5) to the development of the system. The analyses consider model data, which were obtained based on the proposed model configuration that resulted from the research efforts presented in Chapter 2.

3.1 Fundamental Analysis

This section presents a fundamental discussion of the modeled fields and serves as a basis for the following sections in this chapter. Fundamental atmospheric variables as well as a few diagnostics are briefly analyzed in order to illustrate how WRF simulated the synoptic conditions in which the system developed.

The overall synoptic situation that led to the development of the polar low was discussed in Section 1.2. It can also be seen from the modeled fields shown in Figure 3.1. At the surface, the AL moved towards the Bering Strait, advecting lower pressures towards the CBS and causing the BH to weaken and retreat. At 500 hPa, a closed low (also originated from the AL) positioned over the eastern Siberian Sea intensified as it sustained the development of the polar low and helped driving the BH further eastward. The polar low minimum pressure was between 1008 and 1012 hPa (b). The BH went from a center pressure of ~1044 hPa (a) to ~1036 hPa (c).

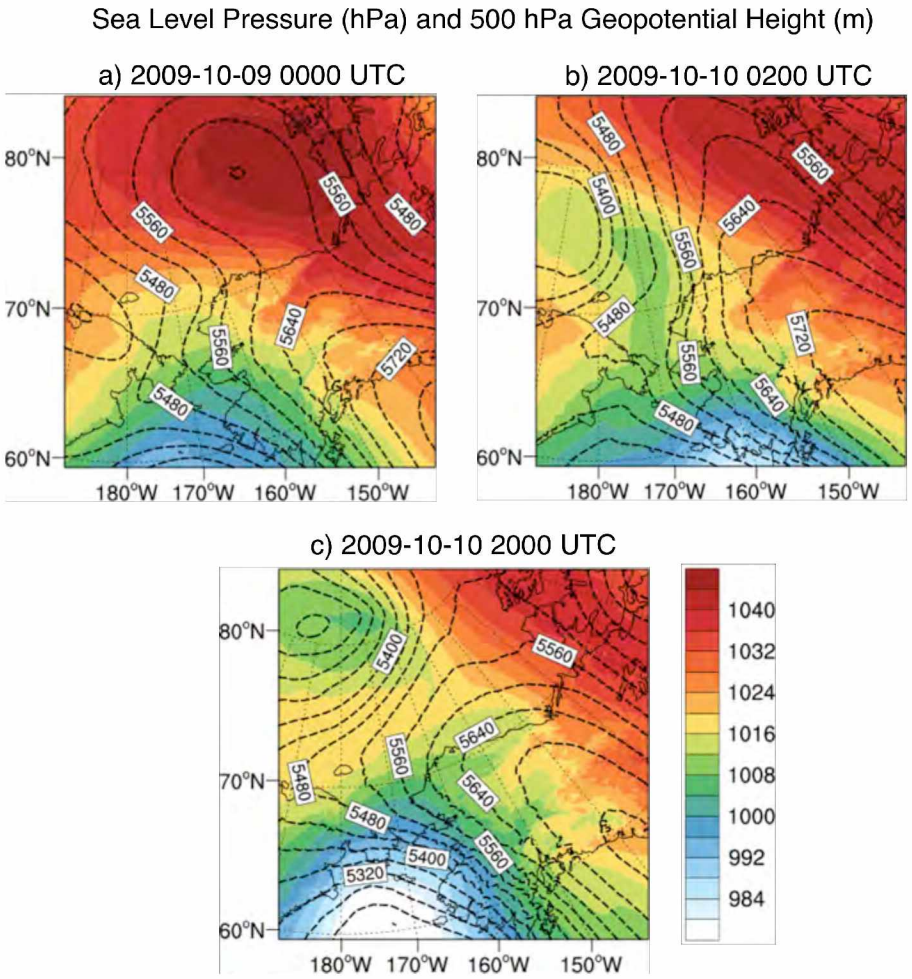

Figure 3.1: Simulated SLP and 500 hPa heights. Valid for October 9, 2009 at 0000 UTC (a), October 10, 2009 at 0200 UTC (b) and 2000 UTC (c). SLP (shaded), unit: hPa. Heights (dashed contours), unit: m.

The cloud structure associated with this situation is illustrated by the OLR fields shown in Figure 3.2. The comma-shaped cloud was well reproduced by the model (b) and was also reflected in the total column precipitable water field (Figure 3.3a). The total column integrated snow revealed values of up to 1.6 kg m^{-2} and indicated that most of the precipitation occurred in the northern flank of the cloud structure (Figure 3.3b).

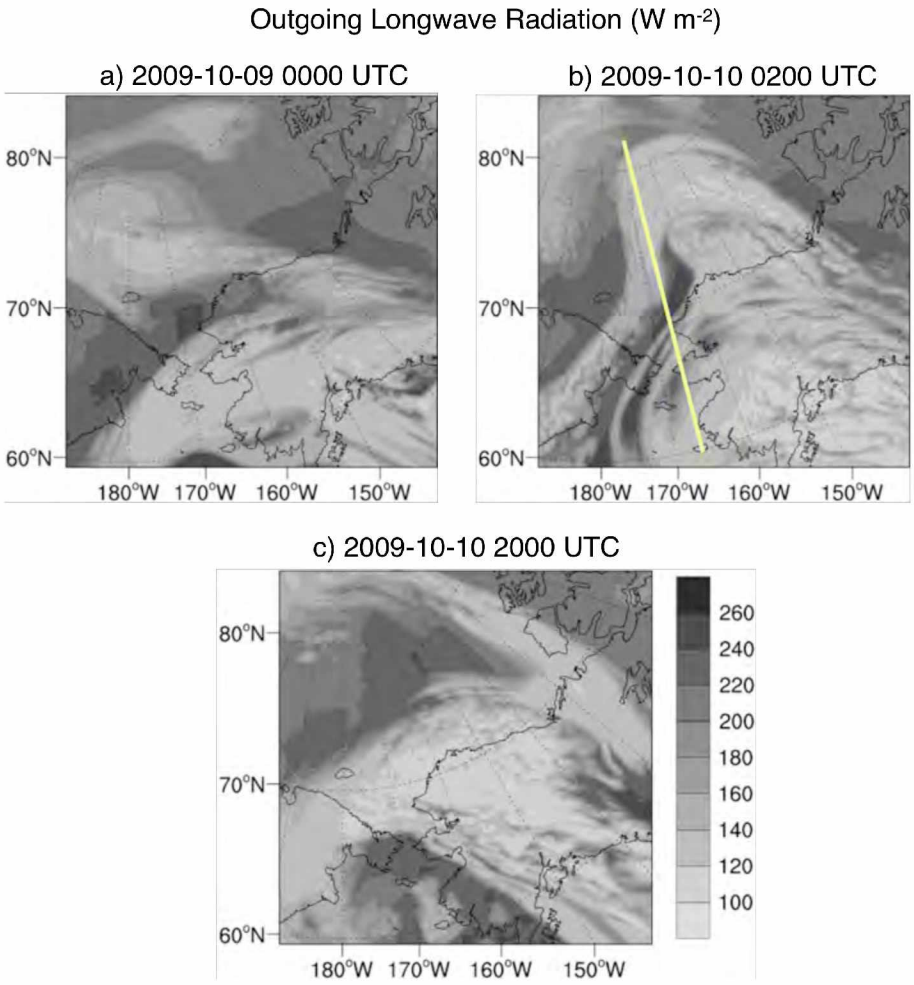

Figure 3.2: Simulated OLR. Valid for October 9, 2009 at 0000 UTC (a), October 10, 2009 at 0200 UTC (b) and 2000 UTC (c). Unit: W m^{-2}. The yellow line on (b) illustrates the cross section shown in Figure 3.8.

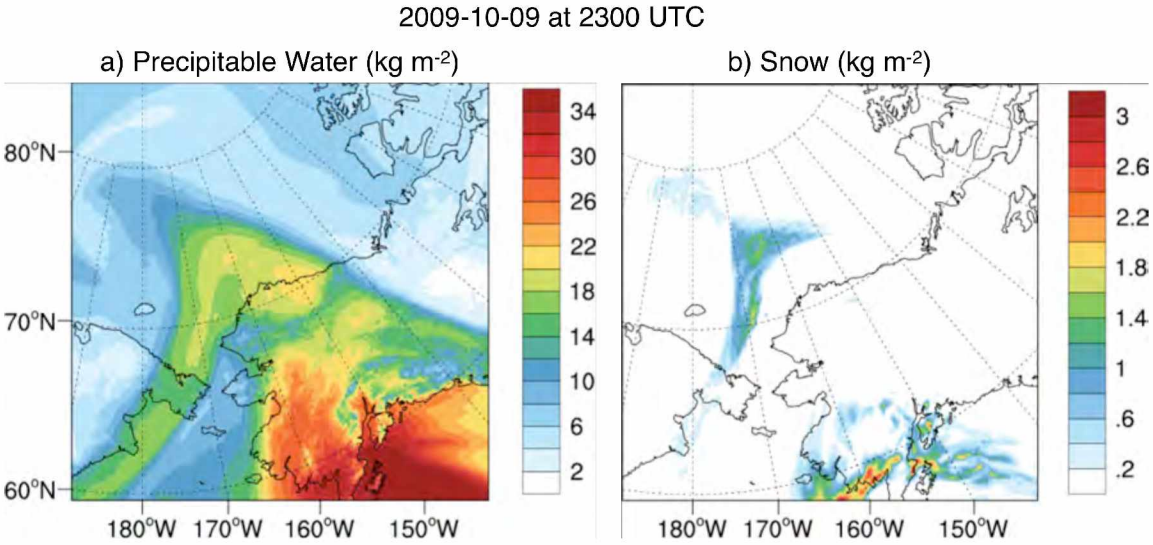

Figure 3.3: Simulated precipitable water and snow. Total column precipitable water (a) and column integrated snow (b). Valid for October 9, 2009 at 2300 UTC. Unit: kg m^{-2}.

Before the polar low onset, the surface winds were predominantly easterlies (Figure 3.4a) and were associated with the BH circulation. A meridional component was introduced on October 9, 2009, associated with the convergence zone between the BH and the developing AL. This feature led to S-SE winds and warm advection in the Chukchi Sea. By October 10, 2009 (Figure 3.4b), the polar low circulation had developed and could be clearly distinguished over the Chukchi Sea. As the low dissipated, it moved northward into the Arctic Ocean (Figure 3.4c and Figure 3.1c). Warm advection into the CBS region was continuous throughout most of the simulation and was associated with the E-SE winds, which could be seen both at the surface (Figure 3.4) and at upper levels (Figure 3.5).

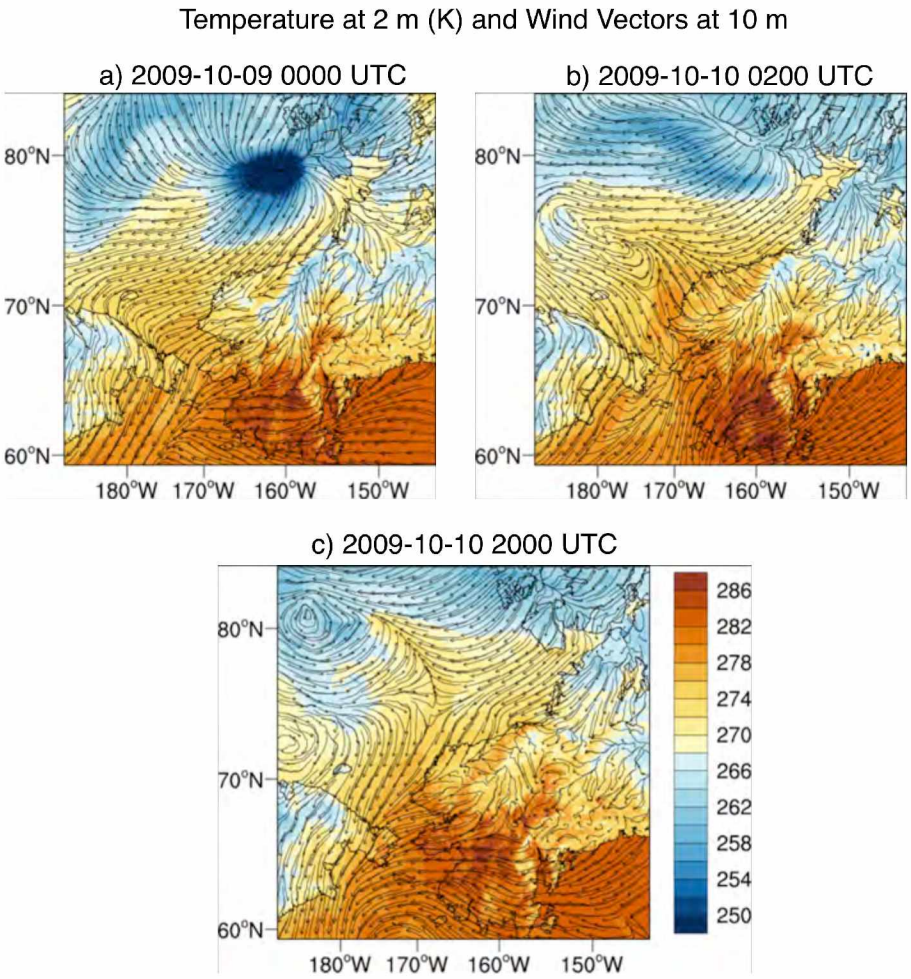

Figure 3.4: Simulated temperature at 2 m and wind vectors at 10 m. Valid for October 9, 2009 at 0000 UTC (a), October 10, 2009 at 0200 UTC (b) and 2000 UTC (c). Unit: K.

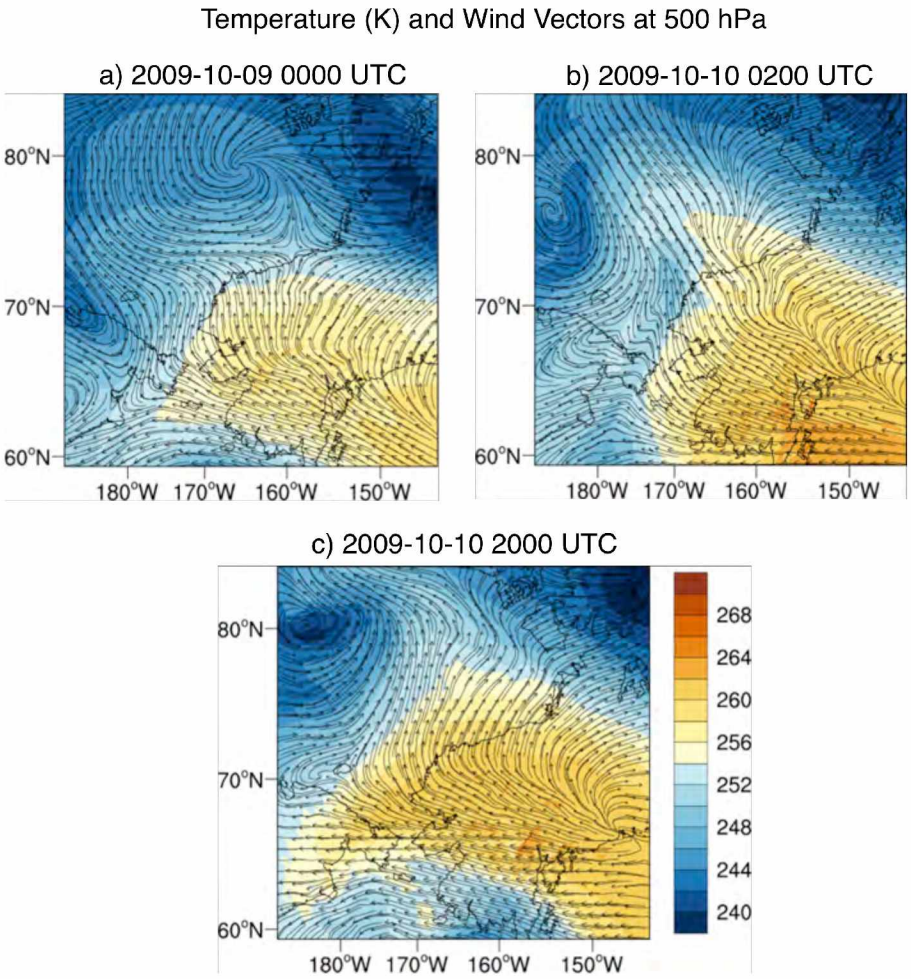

Figure 3.5: Simulated temperature and wind vectors at 500 hPa. Valid for October 9, 2009 at 0000 UTC (a), October 10, 2009 at 0200 UTC (b) and 2000 UTC (c). Unit: K.

At upper levels and before the PL development, the wind field at 500 hPa was dominated by the BH anticyclonic circulation (Figure 3.5a). During the polar low mature stage (b), the main feature is the 500 hPa closed low. Throughout the simulation, the 500 hPa temperatures were relatively warm (Figure 3.5). Nowhere in the domain did they reach 231 K, which is the threshold proposed by Rasmussen and Turner (2003) for an UL cold low to dynamically force a surface low over an ice edge (Moore and Vonder

Haar 2003), in what is commonly referred to as a marine cold-air outbreak. The fact that this was not the case for this polar low can be further confirmed by calculating the Marine Cold Air Outbreak Index (MCAOI; Kolstad and Bracegirdle 2008) within the domain, given by Eq. 3.1 where θ_{SKIN} is the potential temperature calculated from skin temperature, θ_{700} is the potential temperature at 700 hPa, p_{MSL} is the mean SLP in bar and p_{700} is 0.7 bar. The units K bar^{-1} will be preserved for consistency with the original MCAOI definition. For a conversion to S.I. units (K Pa^{-1}) multiply by 1x10^{-4}. For the CBS polar low this calculation results in large negative values, since θ_{700} is much larger than θ_{SKIN}. This indicates high stability and is in agreement with the 95th quantile MCAOI calculations performed by Kolstad and Bracegirdle (2008) for the Beaufort Sea region based on 1961-2000 ERA-40 data.

$$MCAOI = \frac{\theta_{SKIN} - \theta_{700}}{p_{MSL} - p_{700}} \qquad \text{Eq. 3.1}$$

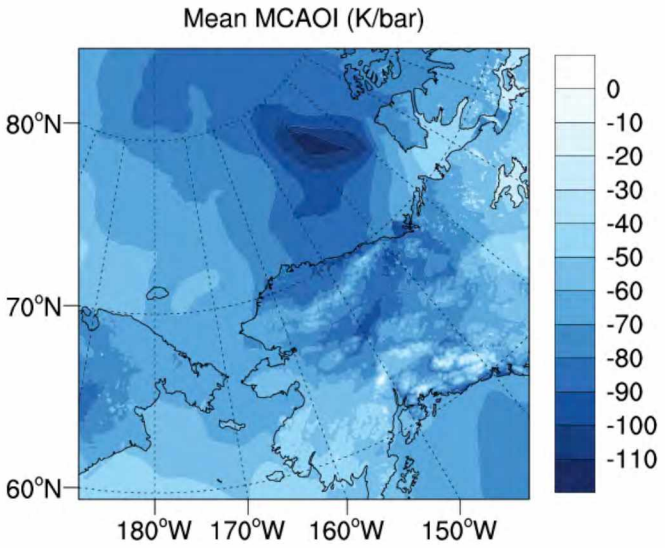

Figure 3.6: Temporal mean of MCAOI. Mean considers output from October 8, 2009 at 1800 UTC up to October 11, 2009 at 0000 UTC. Unit: K bar^{-1} (for S.I. units K/Pa multiply by 1 x 10^{-4}).

The strongest wind speeds associated with the polar low did not occur over the continent, but over the Beaufort Sea. They were caused by the previously mentioned strong convergence zone in this region. As illustrated in Figure 3.7, gusts reached magnitudes of up to ~25 m s^{-1} (a) while the base wind at the same location topped at ~18 m s^{-1} (b).

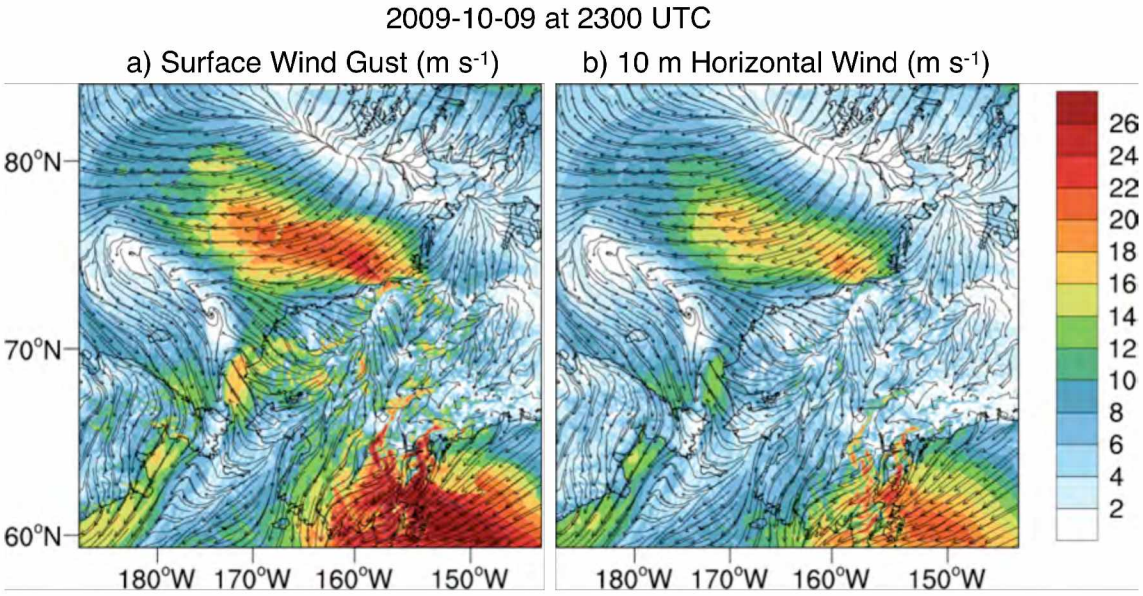

Figure 3.7: Simulated surface wind gust and mean wind. Wind speed (shaded) and full vectors. Valid for October 09, 2009 at 2300 UTC. Unit: m s^{-1}.

The cross-sections shown in Figure 3.8 go through the center of the low near the mature stage, as depicted by the yellow line in Figure 3.2b. The isentropic contours show a cold dome at upper levels from ~69°N to ~75°N (a). The specific humidity values indicate wet air up to 500 hPa (a). The dry column at ~68°N (a) can be explained by the downdrafts (b) and can also be seen as a dark, dry region in the OLR field (Figure 3.2b). An UL positive vorticity maximum south of the storm center seemed to support the development of the low. The positive maximum from ~71°N to ~75°N that extends from the surface to almost 400 hPa represents the circulation of the low itself and is collocated with updrafts.

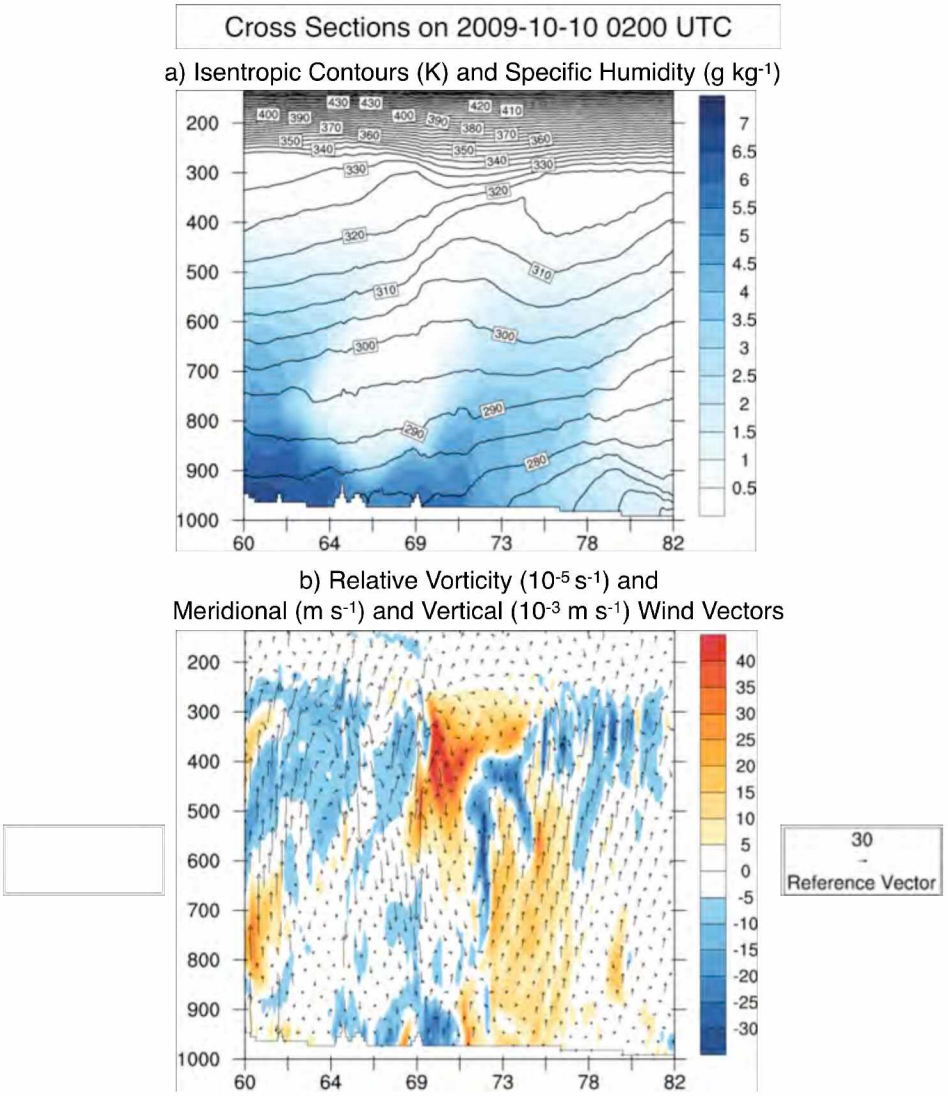

Figure 3.8: Simulated cross sections along 166°W. Potential temperature (contours, unit: K) and specific humidity (shaded, unit: g kg^{-1}) (a). Relative vorticity (shaded, unit: 10^{-5} s^{-1}) and meridional (unit: m s^{-1}) and vertical (unit: 10^{-3} m s^{-1}) wind vectors. Valid for October 10, 2009 at 0200 UTC.

Another useful parameter to consider in this analysis is the moist static energy (MSE) as expressed by Eq. 3.2, where c_p is specific heat, T is temperature, g is gravity, z is height, L_v is latent heat of evaporation and q is water vapor mixing ratio (e.g., Back and Bretherton 2006). It quantifies sensible and latent heat and potential energy. The model data indicates significant advection of MSE from lower latitudes into the CBS region prior to and during the development of the polar low. This advection is most clearly seen at 850 hPa (Figure 3.9), where the horizontal gradients are larger. The MSE maximum in the CBS region follows the shape of the PL clouds (b), indicating that this transport of moisture and energy might have played an important role in sustaining the PL cloud development.

$$MSE = c_p T + gz + L_v q \qquad \text{Eq. 3.2}$$

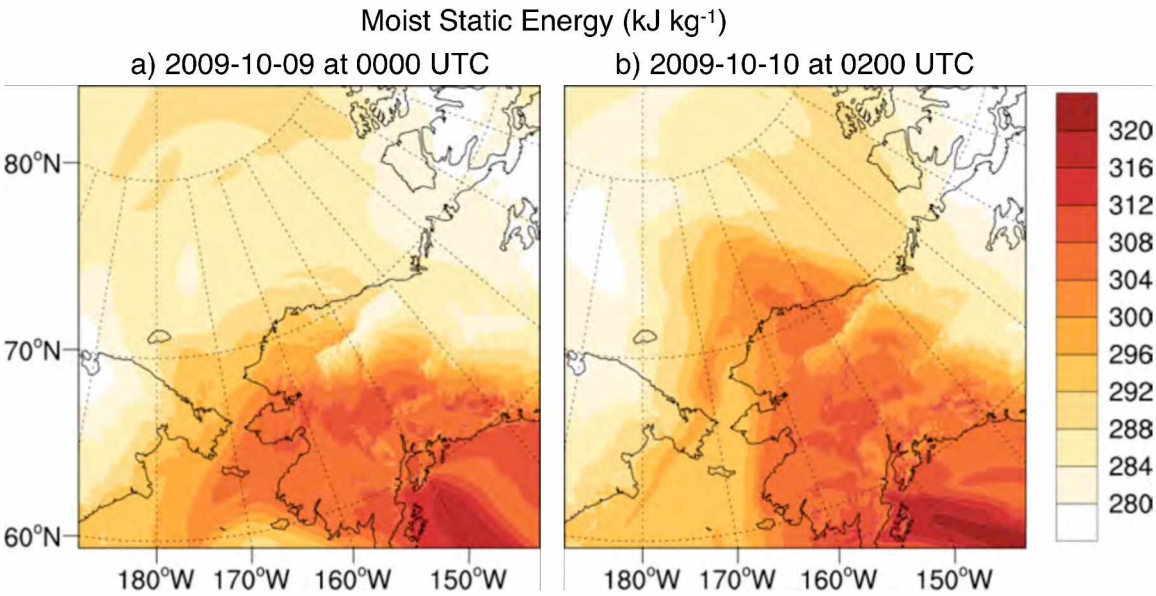

Figure 3.9: Moist Static Energy at 850 hPa. Unit: kJ kg^{-1}. Valid for October 09, 2009 at 0000 UTC (a) and October 10, 2009 at 0200 UTC (b).

3.2 Ensemble Analysis

In order to assess the validity of the analyzed fields and the robustness of the polar low simulation, an analysis was performed on an ensemble set of 25 simulations. These simulations were obtained by perturbing the initial conditions prescribed to the model based on initialization time. Therefore, each simulation was initialized at a different time following 1-hourly intervals. The first ensemble member was started on October 8, 2009 at 0000 UTC and the last one on October 9, 2009 at 0000 UTC. All of the simulations ran up to October 11, 2009 at 0000 UTC and therefore initialization time and run time were the only differences among them. The analysis performed in this section considers output from October 9 at 0600 UTC onwards, in order to allow for a spin up period of at least 6 hours for all of the simulations. The ERA-Interim and NCEP

SST datasets were used for prescribing the large-scale forcings. Since these datasets have 6-hourly and daily frequencies respectively, the 1-hourly input files used to initialize the ensemble members were generated using weighted linear interpolation.

The ensemble analysis presented here is based on 42-hour time series of various atmospheric variables for a point on the Chukchi Sea (73.7°N, 162.2°W). This point was chosen for being within the polar low development location. Some measures used to evaluate the ensemble set are described in the next paragraphs.

The ensemble spread represents the variability across ensemble members for each time point, and is calculated as the standard deviation of the data across the 25 simulations. Therefore, the mean ensemble spread (MES) for the time series of a variable x is given by Eq. 3.3, where t is the simulation hour, nt is the total number of hours included in the time series, s is the simulation (i.e., the ensemble member), ns is the total number of simulations considered, x_S is the value of variable x for simulation s and $\overline{x}$ is the mean value of x across the 25 simulations given at each time t (Storch and Zwiers 2002).

$$MES = \overline{\sigma}_t = \frac{1}{nt}\sum_{t=1}^{nt}\left[\frac{1}{ns-1}\sum_{s=1}^{ns}\left(x_s - \overline{x}\right)^2\right]^{\frac{1}{2}} \qquad \text{Eq. 3.3}$$

The temporal variability of a time series for any individual ensemble member is given by its standard deviation over time (σ_S). We calculated this temporal variability for each simulation and averaged the resulting 25 values to obtain a mean temporal

variability ($\bar{\sigma}_S$) for each variable across the simulations. This quantity was then used to normalize the mean ensemble spread values (MES_R), as expressed by Eq. 3.4. This dimensionless quantity is useful to compare the ensemble spread among different atmospheric fields.

$$MES_R = \frac{MES}{\bar{\sigma}_S} = \frac{\bar{\sigma}_T}{\bar{\sigma}_S} \qquad \text{Eq. 3.4}$$

Another measure used to quantify the quality of the ensemble is the signal to noise ratio (SNR, Eq. 3.5), which is a dimensionless quantity expressed by a quotient of the root mean square (RMS, the signal) and the standard deviation (σ_T, the noise), both of which were calculated for each time across the simulations. The RMS was used in this case rather than the mean in order to give a more accurate measure of the average for fields with both negative and positive values, such as sensible heat flux and wind components. The fields with strictly positive values were not affected by this choice. To simplify the analysis, we considered only the temporal mean SNR_{MEAN} and not the entire SNR time series. It is important to note that although both MES_R and SNR_{MEAN} include information about the ensemble spread, they do so in a different manner. While the MES_R quantifies the spread (σ_T) relative to the mean variability of each ensemble series (σ_S), the SNR_{MEAN} uses the same spread (σ_T) to quantify the signal (RMS).

$$SNR = \frac{RMS}{\sigma_T} \qquad \text{Eq. 3.5}$$

Figure 3.10 shows time series for several surface variables, from which we can clearly see that there are no large phase shifts and amplitude differences among the simulations. The larger disagreements are seen for boundary layer height (i), which is a very dynamic quantity in itself. The mid- and upper-level fields also seemed to produce relatively solid results as can be evaluated in Figure 3.11. The largest spread in this case is seen for tropopause height (d) and meridional wind at 300 hPa (f).

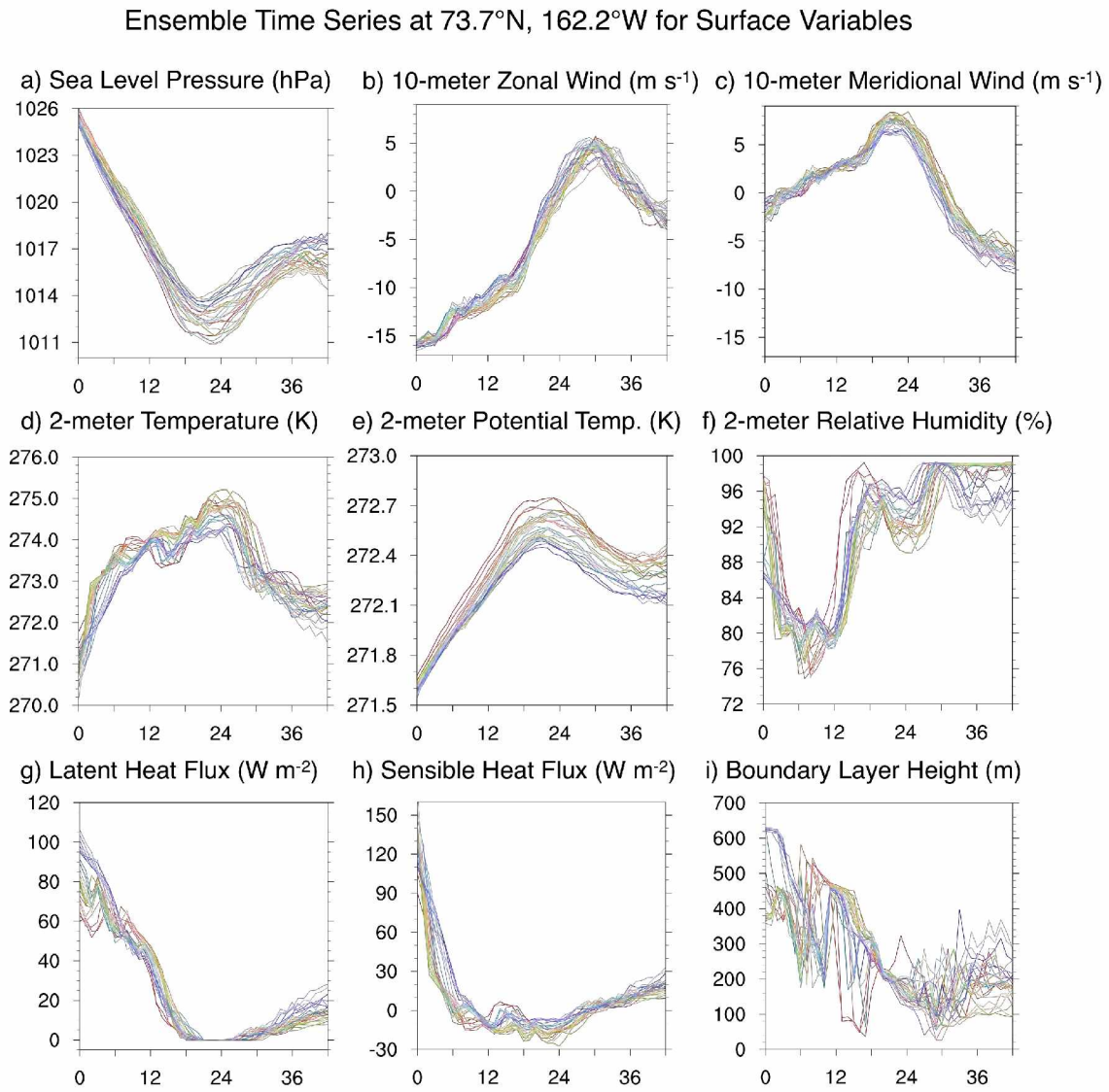

Figure 3.10: Ensemble time series at 73.7°N, 162.2°W for surface variables. Colored lines represent ensemble members. (a) SLP (hPa), (b) zonal and (c) meridional wind at 10 m (m s^{-1}), (d) temperature at 2 m (K), (e) surface potential temperature (K), (f) relative humidity at 2 m (%), (g) latent and (h) sensible heat fluxes at the surface (W m^{-2}) and (i) boundary layer height (m). Horizontal axis is time (hours) since October 9, 2009 at 0600 UTC.

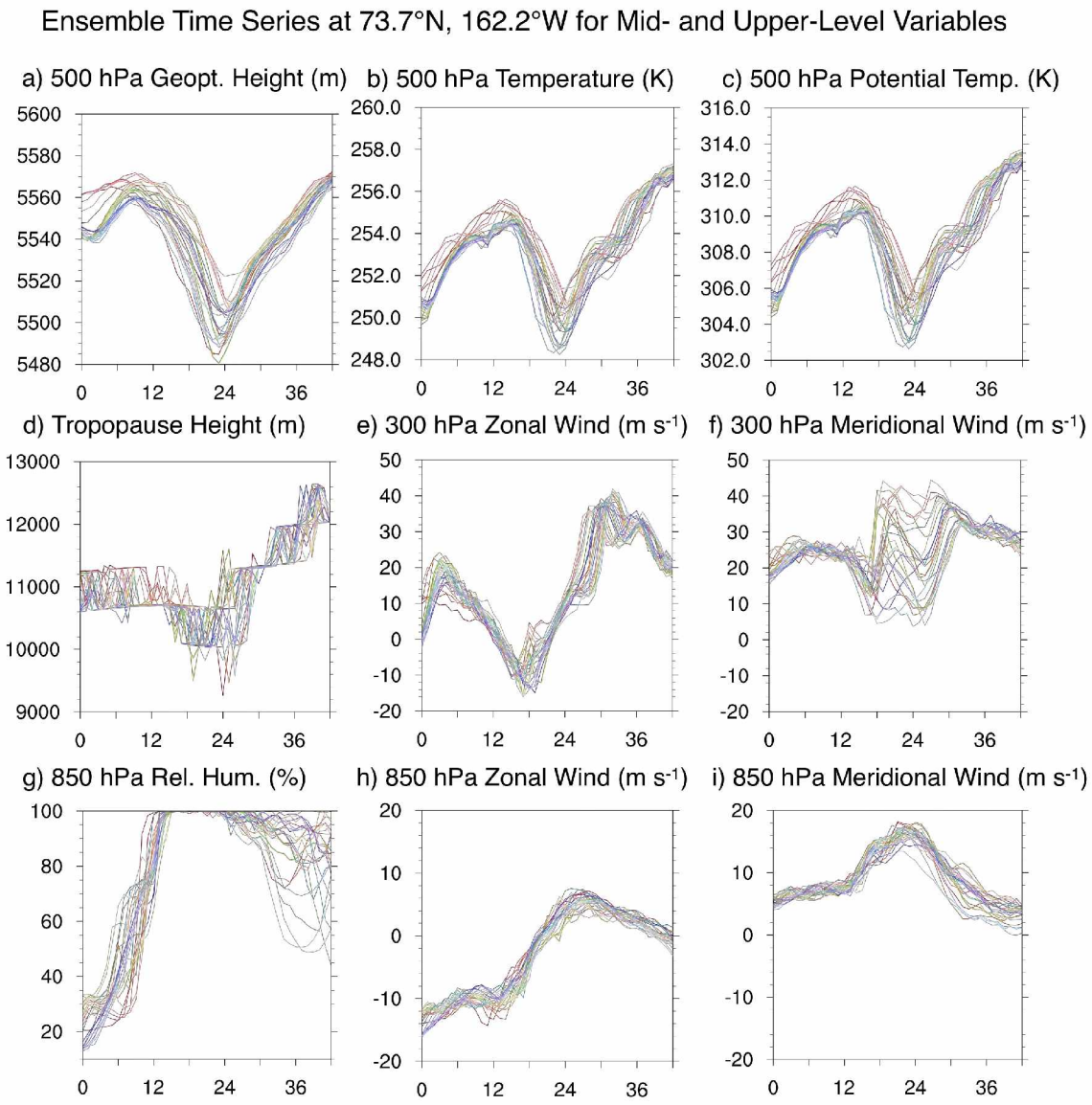

Figure 3.11: Ensemble time series at 73.7°N, 162.2°W for mid- and upper-level variables. Colored lines represent ensemble members. (a) geopotential height at 500 hPa (m), (b) temperature at 500 hPa (K), (c) potential temperature at 500 hPa (K), (d) tropopause height (m), (e) zonal and (f) meridional wind at 300 hPa (m s^{-1}), (g) relative humidity at 850 hPa (%), (h) zonal and (i) meridional wind at 850 hPa (m s^{-1}). Horizontal axis is time (hours) since October 9, 2009 at 0600 UTC.

These initial statements can be evaluated quantitatively by examining the values presented in Table 3.1 and Table 3.2. The MES_R calculations confirm the expected and relatively small spread for most of the variables. The highest MES_R is seen for meridional wind at 300 hPa, where it is ~65% of the mean variability within the time series. However, this spread is relatively small. The SNR_{MEAN} also indicates a small amount of noise for this variable, even smaller than that for zonal wind at the same level.

Table 3.1: Measures of ensemble spread for surface variables.

Surface Variables	**MES**	**MES_R**	**SNR_{MEAN}**
Sea-level pressure	0.73 hPa	~0.21	1554.89
Zonal wind at 10 m	0.77 m s^{-1}	~0.11	12.49
Meridional wind at 10 m	0.67 m s^{-1}	~0.15	6.14
Temperature at 2 m	0.30 K	~0.32	1100.28
Potential temperature at 2 m	0.07 K	~0.27	4378.50
Relative humidity at 2 m	2.13 %	~0.29	50.70
Latent heat flux at the surface	4.04 W m^{-2}	~0.15	4.64
Sensible heat flux at the surface	6.45 W m^{-2}	~0.22	2.75
Boundary layer height	65.65 m	~0.49	5.69

Table 3.2: Measures of ensemble spread for mid- and upper-level variables.

Mid- and Upper-level Variables	**MES**	**MES_R**	**SNR_{MEAN}**
500 hPa geopotential height	6.89 m	~0.34	1002.36
500 hPa temperature	0.57 K	~0.29	543.80
500 hPa potential temperature	0.70 K	~0.29	543.69
Tropopause height	255.17 m	~0.41	79.34
300 hPa zonal wind	3.31 m s^{-1}	~0.24	5.91
300 hPa meridional wind	4.35 m s^{-1}	~0.65	12.41
850 hPa relative humidity	6.90 %	~0.26	247.27
850 hPa zonal wind	1.10 m s^{-1}	~0.16	5.71
850 hPa meridional wind	1.23 m s^{-1}	~0.29	8.21

Based on the discussion presented so far, it is possible to confidently pursue a more detailed analysis based on the simulated fields. The purpose now is to investigate the mechanisms responsible for the development of the polar low. In the following sections, a few hypotheses are proposed and investigated.

3.3 Sea-Ice Extent and Sea-Surface Temperatures

As mentioned in Chapter 1, the CBS sector is known to present a minimum of cyclone frequency and intensity (Lynch et al. 2003) due to the elevated sea-ice concentration (SIC) and the presence of the BH during the winter months. According to the National Snow and Ice Data Center (Fetterer et al. 2002), the Northern Hemisphere sea-ice extent anomaly for October 2009 (when the CBS polar low developed) was close to -20%, being the third largest negative anomaly for October since 1979 (Figure 3.12). It seems intuitive to suppose that this maritime system was able to develop precisely due to the increased area of open water brought on by the lower ice extent. This open water with

relatively warmer SST could be responsible for providing the moisture and heat fluxes necessary to trigger and sustain the development of an intense maritime mesocyclone. Therefore, the first hypothesis to be tested in this chapter assesses the role of sea-ice extent and sea-surface temperatures for the development of the polar low.

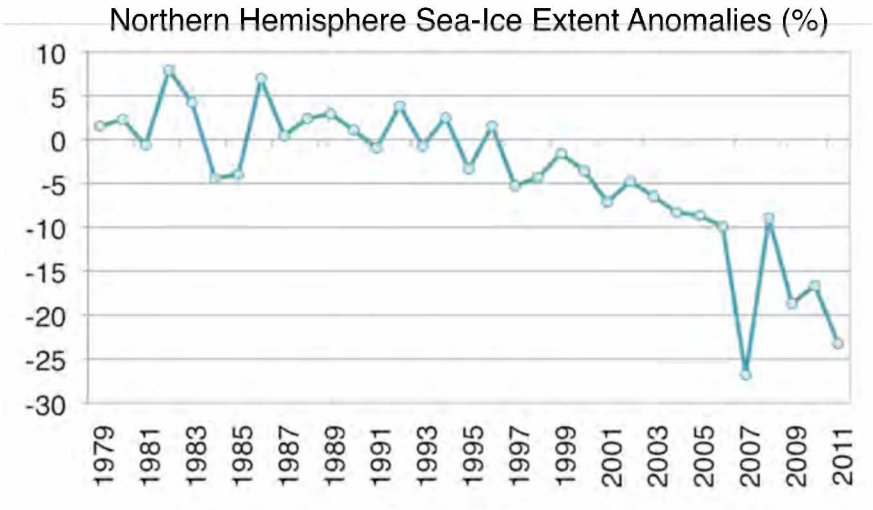

Figure 3.12: Northern Hemisphere sea-ice extent anomalies for October. Values from 1979 to 2011 based on the 1979-2000 mean of 9.28 million km^2. Unit: %.

In order to achieve this purpose, a model simulation was run with climatological SST and SIC fields. These climatological fields were calculated using daily values from 1981 to 2009, obtained from the NOAA Optimum Interpolation Analyses version 2. This data is on a global grid of 0.25°. Figure 3.13 shows the calculated climatological fields for October 9 for half of the northern hemisphere. This dataset was chosen for being the

only long term SST and SIC dataset with a high spatial (0.25°) and temporal (daily) resolution.

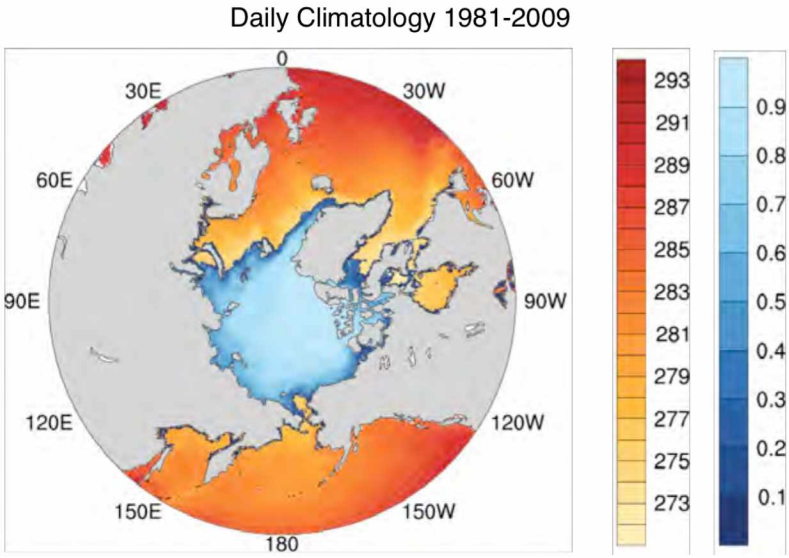

Figure 3.13: Daily 1981-2009 climatology for SST and SIC. Valid for October 9. Shown for latitudes 45°N to 90°N. SST (red contours), unit: K. SIC (blue contours), unit: sea-ice fraction.

Figure 3.14 shows the difference between the fields used as BC for the non-climatology (NOT_CLIM) and for the climatology (CLIM) simulations. Note that all of the difference plots shown in this section refer to the NOT_CLIM anomalies having the CLIM fields as a reference. As expected, the climatological values are considerably different from the ones observed in 2009. It is evident that there is a large negative anomaly in the SIC field in the region of the CBS where the storm developed (a). Similarly, a positive anomaly is seen in the same region for the SST field (b). Using the

climatological fields as boundary conditions for the CLIM simulation can help determine if the 2009 SIC and SST anomalies were important for allowing the development of the low. Both simulations analyzed in this section (CLIM and NOT_CLIM) were run without spectral nudging. This procedure was done in order to avoid the assimilation of analyses in the CLIM simulation, provided that the atmospheric state in these analyses is based on the 2009 observed BC. This assimilation could introduce a bias in the CLIM simulation and thus compromise the validity of the experiment.

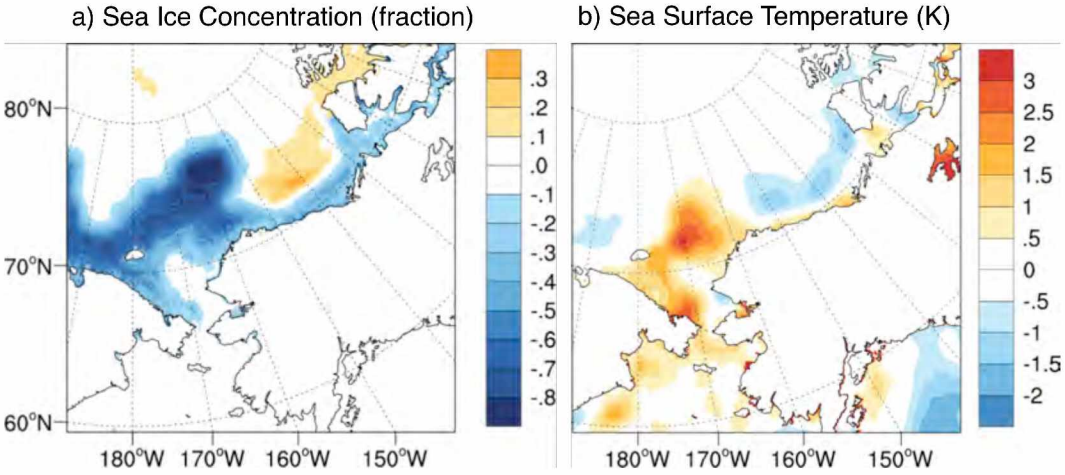

Figure 3.14: NOT_CLIM – CLIM mean difference for SIC and SST. SIC (a). Unit: sea ice fraction. SST (b). Unit: K.

By analyzing the SLP and wind circulation fields (Figure 3.15), we can see that the polar low development was not hindered by the modified boundary conditions. That is not to say those fields were not affected by the lower SIC and higher SST values. The mean difference shown in Figure 3.16a indicates that the 2009 simulation had lower SLP

values in the Chukchi Sea and eastern Siberian Sea of up to 0.8 hPa (a more intense polar low) as well as a slightly more intense BH. However, no differences can be seen in the geopotential height field at any level, as exemplified by Figure 3.16b. The differences are also very small for the wind field (Figure 3.17). In the region where the low developed, the zonal component was less intense in the NOT_CLIM simulation and no distinct differences can be seen for the meridional component. In general, the mean wind differences do not exceed 1 m s^{-1} at any level.

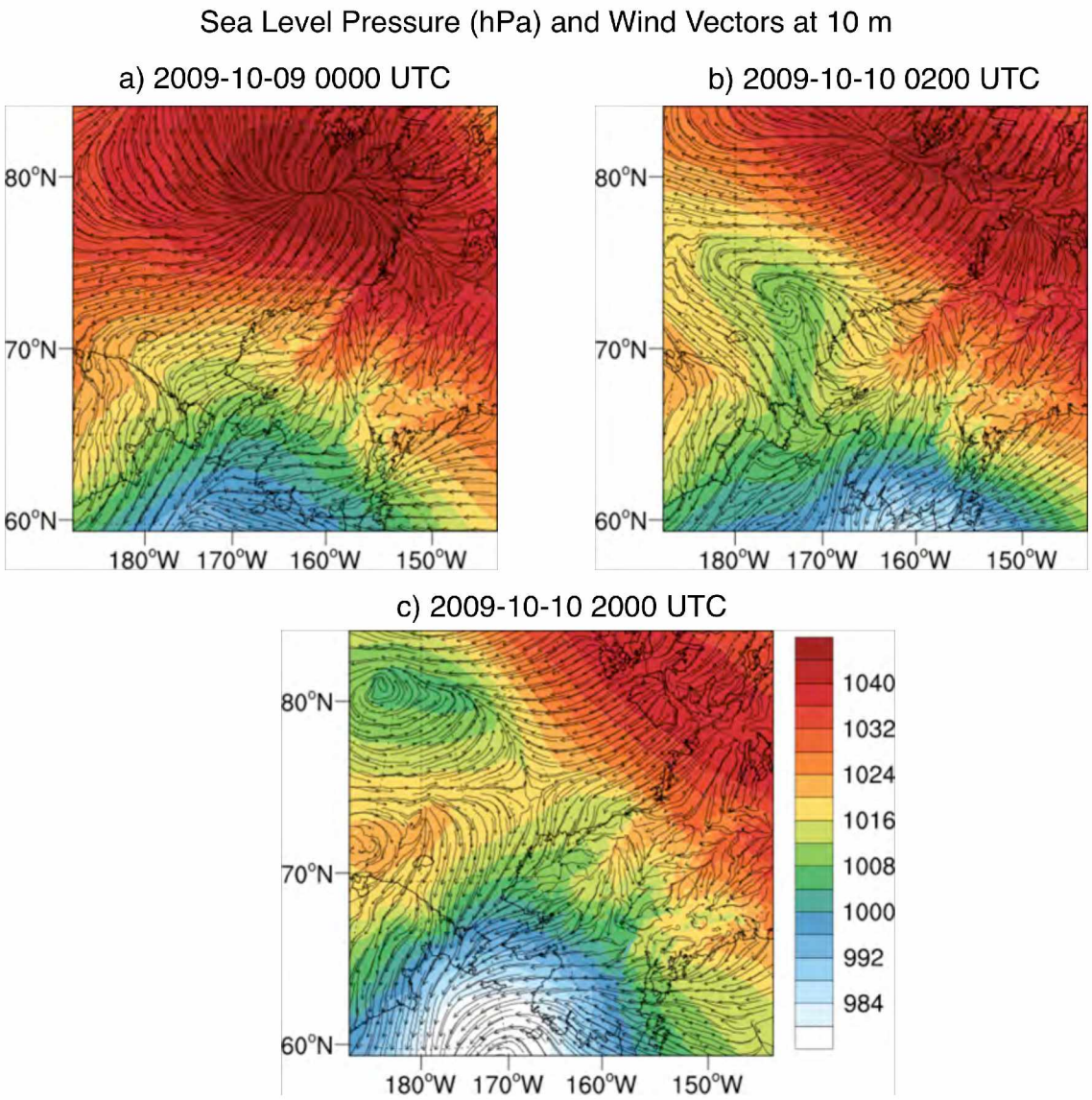

Figure 3.15: Polar low evolution in CLIM simulation. SLP and wind vectors. Unit: hPa. Valid for October 9, 2009 at 0000 UTC (a), October 10, 2009 at 0200 UTC (b) and 2000 UTC (c).

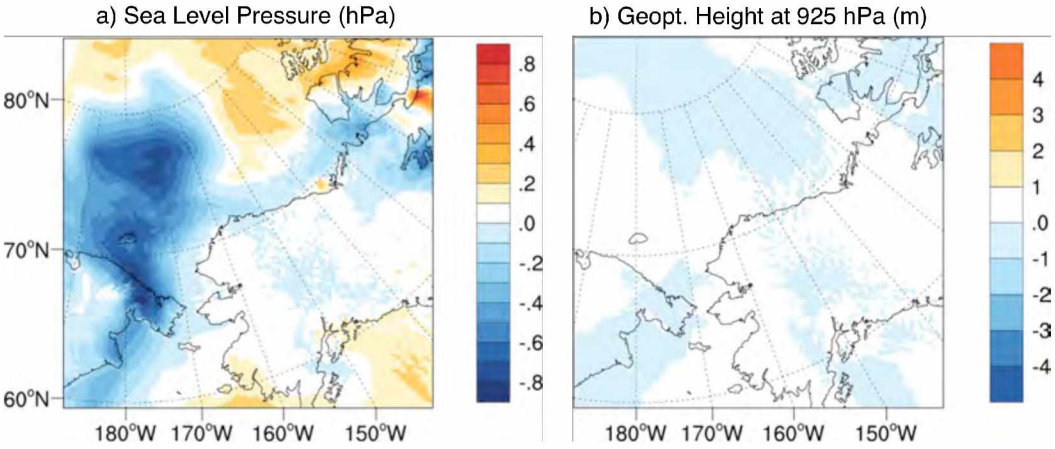

Figure 3.16: NOT_CLIM – CLIM mean difference for SLP and 925 hPa geopotential height. SLP (a). Unit: hPa. Geopotential height (b). Unit: m.

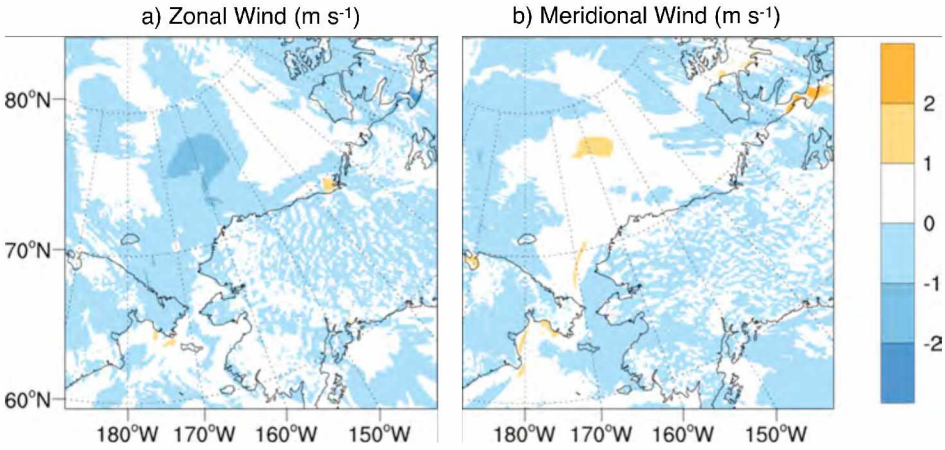

Figure 3.17: NOT_CLIM – CLIM mean difference for horizontal wind at 10 m. Zonal (a) and meridional (b) components. Unit: m s^{-1}.

The climatology simulation also presents differences in the surface fluxes (Figure 3.18), which were inhibited in the CLIM simulation in the region of the Chukchi Sea due to the higher sea-ice extent. The three fluxes considered in this analysis present regions of maxima centered around 75°N, 160°W on the Chukchi Sea, which is where the 2009

SIC anomaly is most pronounced (Figure 3.14). In this region, the sensible heat flux was ~60 W m^{-2} weaker (Figure 3.18a), the latent heat flux was ~30 W m^{-2} weaker (Figure 3.18b) and the moisture flux was ~0.01 g m^{-2} s^{-1} weaker (Figure 3.18c). The negative maxima east of the positive maxima indicate enhanced surface fluxes, brought on by the lower sea-ice concentration in the climatological boundary conditions for that small area. This behavior can be explained by the fractional nature of the SIC field and the fact that in the NOT_CLIM simulation the ice is thicker at that location than what is seen in the climatological field (Figure 3.14).

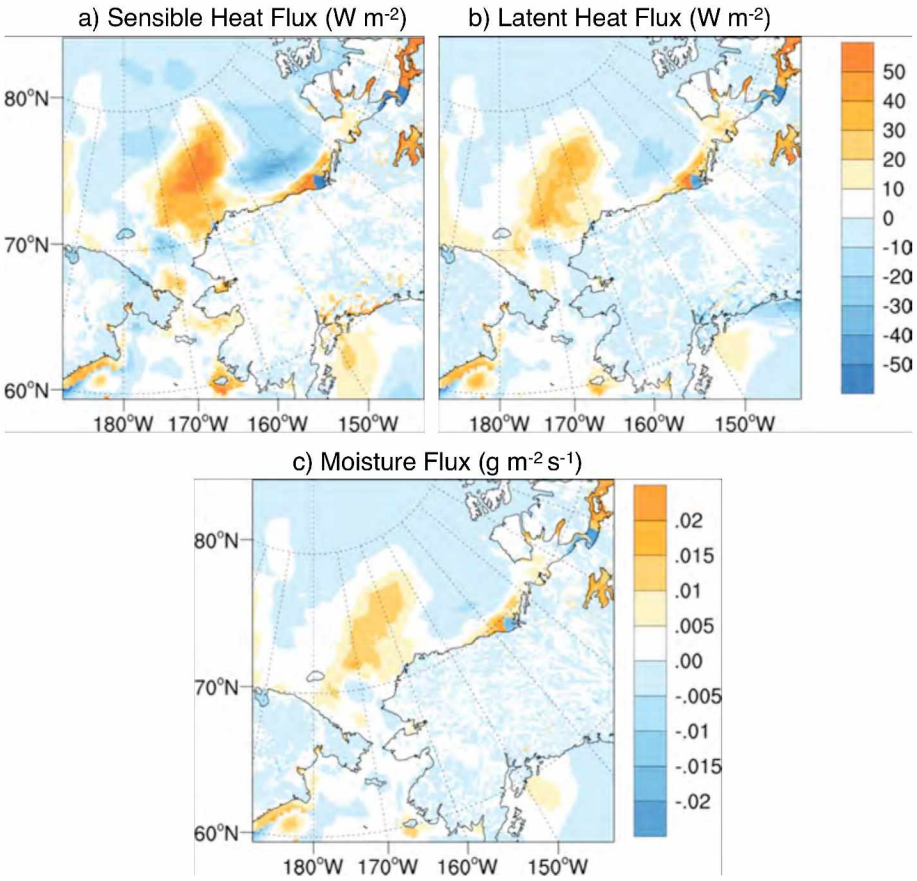

Figure 3.18: NOT_CLIM – CLIM mean difference for surface fluxes. Sensible heat (a) and latent heat (b) fluxes. Unit: W m^{-2}. Moisture flux (c). Unit: g m^{-2} s^{-1}.

Similar differences can also be seen for other surface variables. The NOT_CLIM simulation presented warmer air temperatures at 2 m (Figure 3.19) and, as expected, the region of maximum difference is colocated with that for the surface fluxes. The same can be said for specific humidity at 2 m (Figure 3.20). The mean differences for these variables do not exceed 4 K and 0.6 g kg^{-1} in magnitude. In both cases, the magnitude of the difference decreases substantially with height and disappears by 850 hPa. The time series in Figure 3.21 illustrates the difference between CLIM and NOT_CLIM for SLP

and 2 m temperature for a point underneath the storm. As was also indicated by the spatial plots, the CLIM simulation presents a slightly less intense polar low and higher 2 m air temperatures.

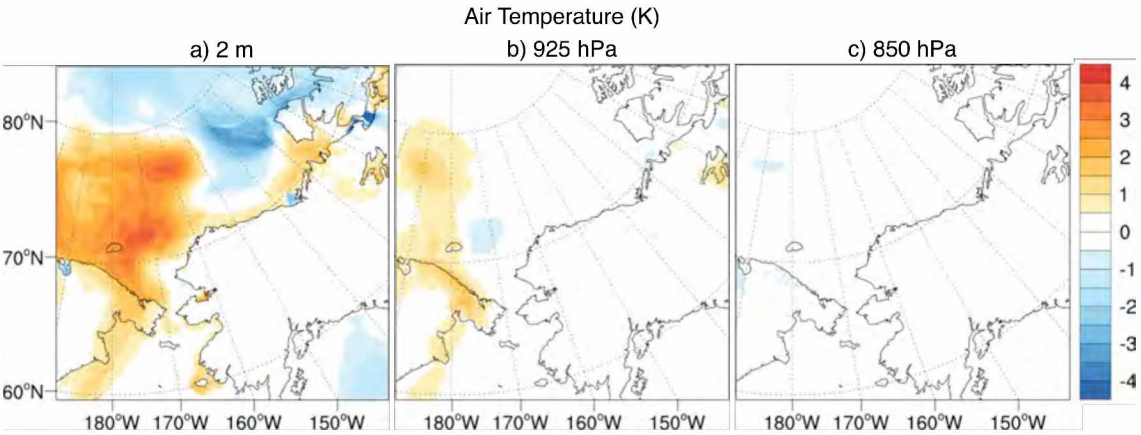

Figure 3.19: NOT_CLIM – CLIM mean difference for air temperature. At 2 m (a), 925 hPa (b) and at 850 hPa (c). Unit: K.

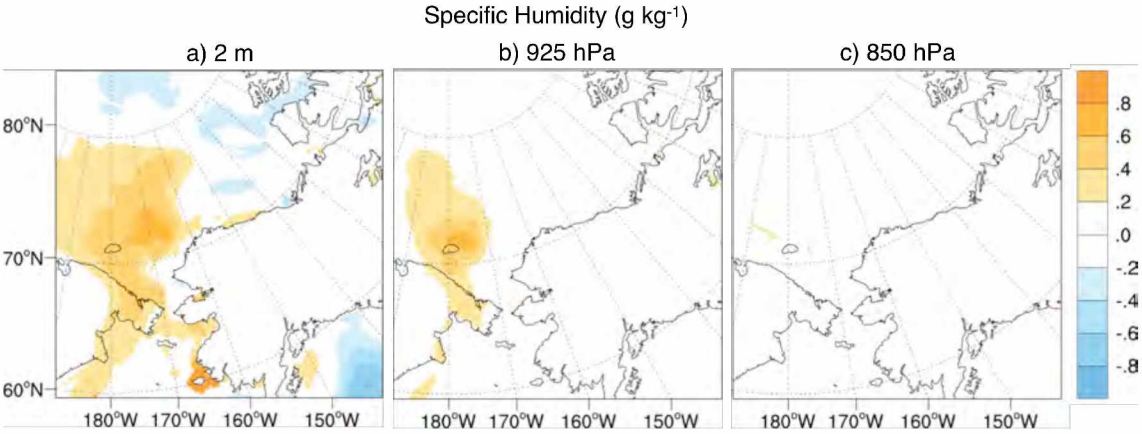

Figure 3.20: NOT_CLIM – CLIM mean difference for specific humidity. At 2 m (a), 925 hPa (b) and 850 hPa (c). Unit: g kg^{-1}.

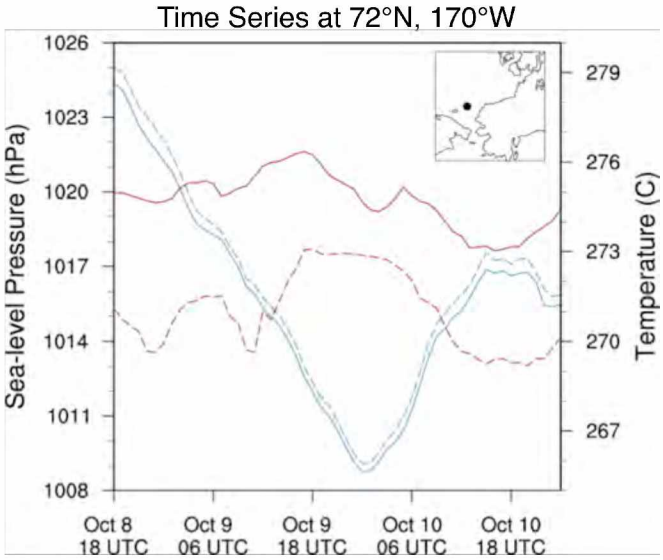

Figure 3.21: Temperature and SLP time series at 72°N, 170°W. NOT_CLIM (solid) and CLIM (dashed) simulations. SLP (blue). Unit: hPa. Air temperature at 2 m (red). Unit: K. Horizontal axis is time from October 8, 2009 at 1800 UTC to October 11, 2009 at 0000 UTC. Location relative to simulation domain is shown by black dot on upper-right corner.

According to this analysis, the effects of the modified boundary forcings on the polar low simulation were minor and could not penetrate above 850 hPa. This can be explained by a very stable lower atmosphere, which was observed in the Chukchi Sea when the polar low developed (Figure 1.11). These results indicate that surface forcings were not crucial for the development of the CBS polar low and presented a small contribution to its intensification. This finding is in accordance with the idealized study of Yanase and Niino (2007) who found that for polar lows with a strong baroclinic development, surface diabatic forcings were not major contributors and only acted to enhance the vortex growth rate. The findings discussed in this section are very important since they present realistic evidence that polar lows are able to develop without the

contribution of maritime heat and moisture fluxes and in a stably stratified lower atmosphere.

3.4 Potential Vorticity

As well as assessing the role of lower boundary forcings, it is important to understand if and how UL parameters acted on the development of the system. A common and important parameter in sustaining the formation and growth of polar lows are UL potential vorticity (PV) anomalies (e.g., Bresch et al. 1997; Claud et al. 2007; Blechschmidt et al. 2009; Bracegirdle and Gray 2009). On that account, this section investigates the presence of PV anomalies (PVA) and their possible contribution to the development of the system being studied.

In simple terms as expressed by Holton (2004), PV is a "measure of the ratio of the absolute vorticity to the effective depth of the vortex." The Ertel (also referred to as "full") PV is given by Eq. 3.6, where ρ is the air density, $\vec{\zeta}_a$ is the full vorticity vector and θ is potential temperature. The isentropic PV (IPV) is given by Eq. 3.7, where g is gravity, ζ_θ is the relative vorticity and f is the planetary vorticity. IPV is simply a product of absolute vorticity (a dynamic parameter) and static stability (a thermodynamic parameter) and is a useful quantity for tracking atmospheric motions in space and time because it is conserved for an adiabatic frictionless flow in a homogeneous incompressible fluid (Holton 2004).

$$PV = \frac{1}{\rho}\left(\vec{\zeta}_a \cdot \nabla\theta\right) \qquad \text{Eq. 3.6}$$

$$IPV = -g\left(\zeta_\theta + f\right)\frac{\partial\theta}{\partial P} \qquad \text{Eq. 3.7}$$

The first step towards determining a possible role of PV in the development of the polar low is to look for any PVAs at upper levels. Indeed, a pronounced anomaly could be seen north of Siberia (Figure 3.22), with values of ~4 PVU at 305 K. The approximate height of this surface at the location of the anomaly was 350 hPa. A second and smaller PV maximum can also be seen in the area where the storm developed on the eastern Chukchi Sea by the Alaska coast.

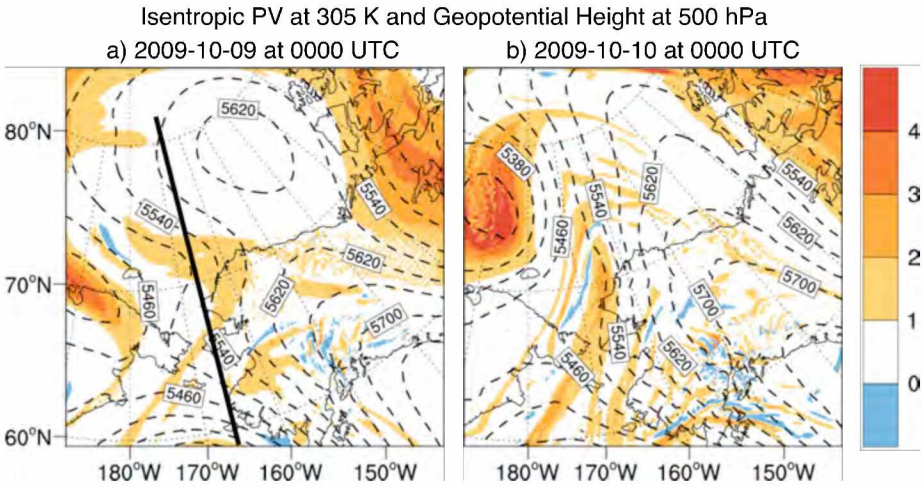

Figure 3.22: Isentropic PV at 305 K and geopotential height at 500 hPa. Valid for October 9, 2009 at 0000 UTC (a) and October 10, 2009 at 0000 UTC (b). PV (shaded). Unit: PVU. Geopotential height (dashed). Unit: m.

The time series in Figure 3.23 are for two points centered at the anomalies discussed above. They reveal a considerably lower tropopause near the time of polar low development, around October 10, 2009 at 0000 UTC. This tropopause lowering indicates the stratospheric origin of the PVAs. It is more dramatic and lasts longer for the larger anomaly (dashed line). The difference in tropopause pressure during and after the polar low is ~150 hPa for the larger anomaly and ~100 hPa for the smaller one.

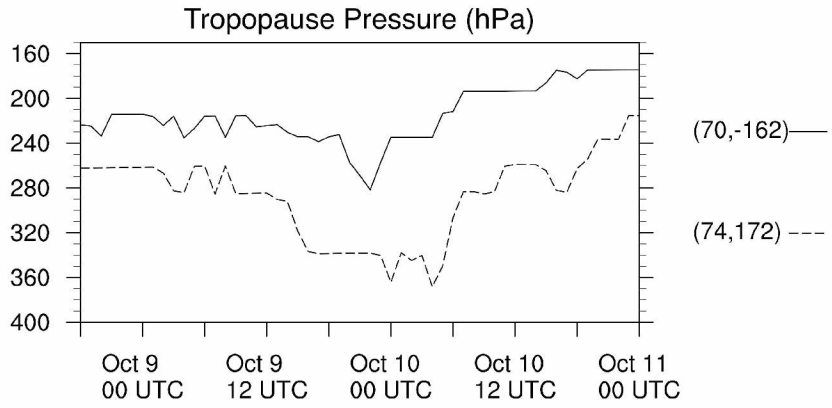

Figure 3.23: Time series of tropopause pressure. Valid from October 8, 2009 at 1800 UTC up to October 11, 2009 at 0000 UTC. Unit: hPa. Locations: 70°N, 162°W (solid) and 74°N, 172°E (dashed).

The larger anomaly was present in the domain since the beginning of the simulation. As its location suggests, it was associated with the previously mentioned UL closed low (see Section 3.1), and followed it as it moved northward (Figure 3.22). The smaller anomaly was advected from lower latitudes. As evidenced by Figure 3.24, it split off a larger anomaly (a) that was associated with the AL and was also present in the

domain since the start of the simulation. This "split" coincided with the arrival of the jet stream, just before the polar low development took place (b). The UL circulation associated with the arrival of the jet is illustrated in Figure 3.25. As the jet moved northward, so did the PV maximum (Figure 3.24c). Near the time of storm development the PVA had reached ~70°N and was positioned right above the storm genesis region. It penetrated almost as deep as 600 hPa. The penetration depth of a PVA indicates how much its associated cyclonic circulation influences the surface temperature field (Martin 2006). In this case, this deep penetration indicates that the PVA may significantly affect the lower levels, interacting with thermodynamic features such as a pre-existing low-level (LL) baroclinic zone. This topic will be discussed in the following section.

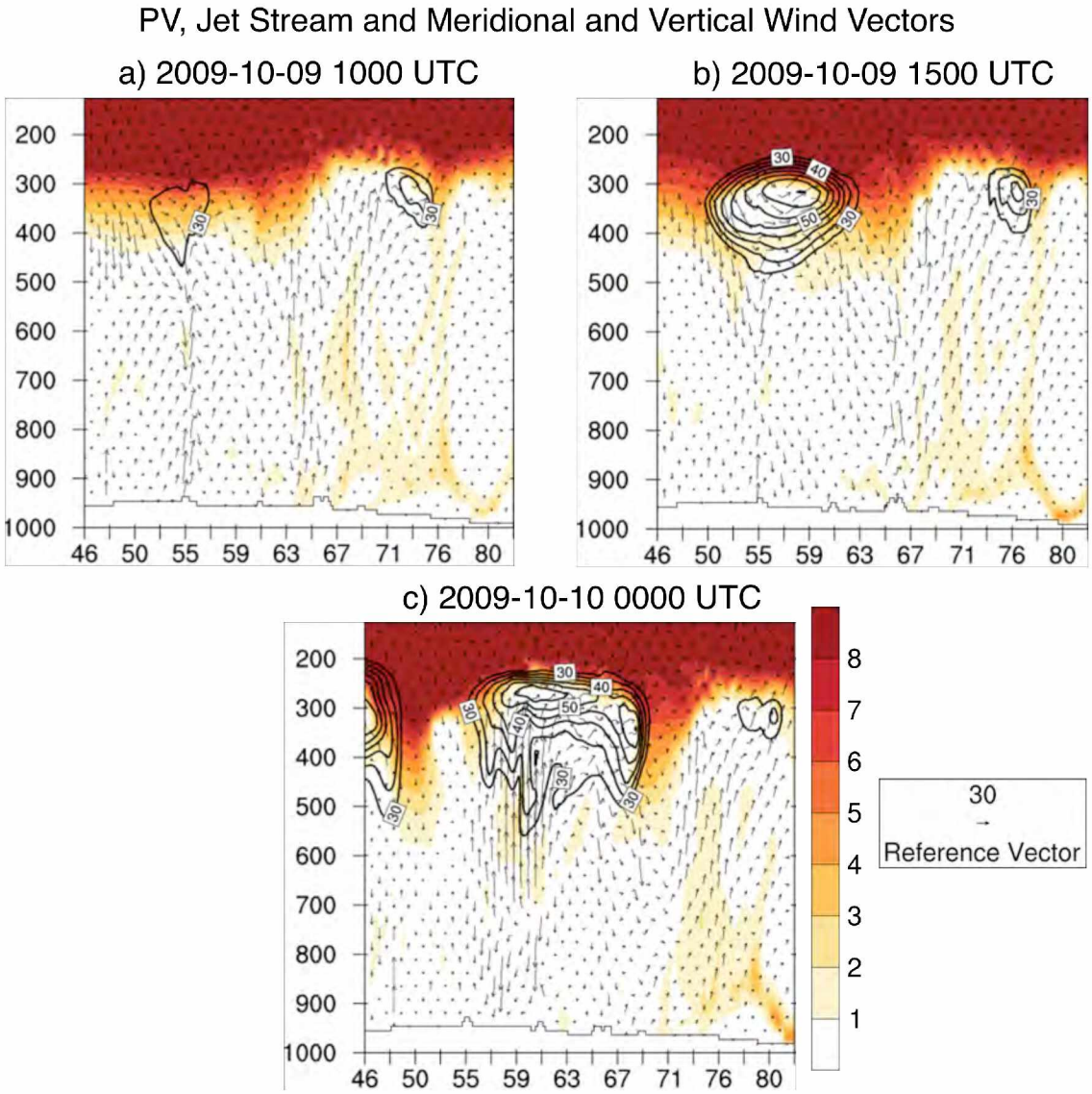

Figure 3.24: Parent domain cross sections along 166°W. Latitudes from 46°N to 82°N. Valid for October 9, 2009 at 1000 UTC (a) and 1500 UTC (b) and October 10, 2009 at 0000 UTC (c). Potential vorticity (shaded). Unit: PVU. Jet stream (contours). Unit: m s^{-1}. Meridional and vertical wind (vectors). Unit: m s^{-1}. Vertical wind is scaled by 10^3.

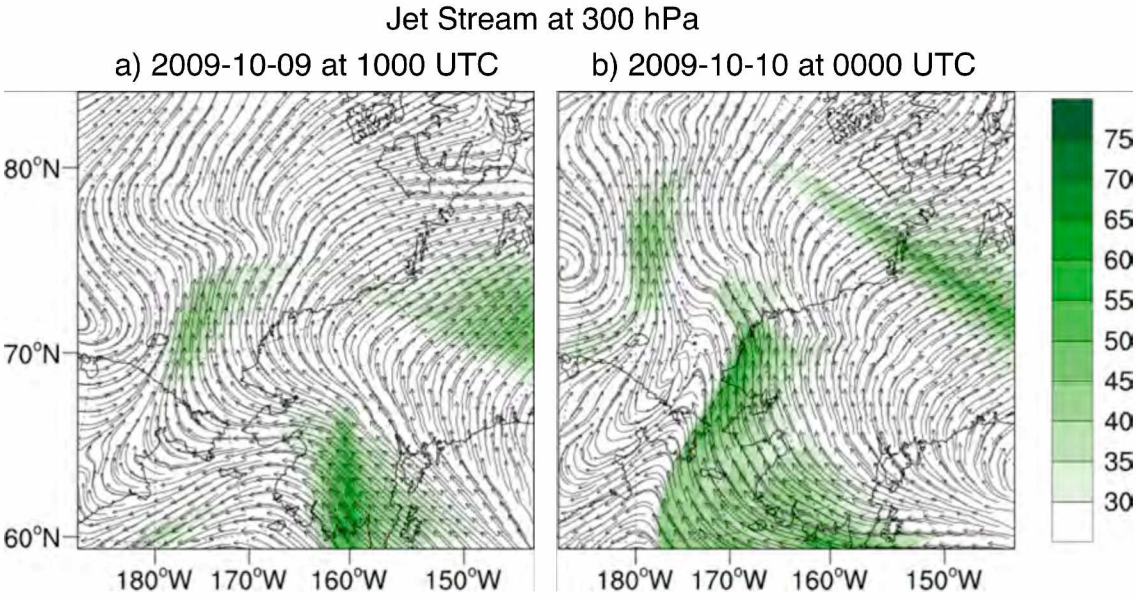

Figure 3.25: Simulated jet stream at 300 hPa. Valid for October 09, 2009 at 1000 UTC (a) and October 10, 2009 at 0000 UTC (b). Unit: m s^{-1}.

3.5 Baroclinicity

Comma-shaped systems are very often linked to deep baroclinicity near the polar front (e.g., Rasmussen and Turner 2003). The CBS polar low was not only comma shaped, but it formed in a region of very strong thermal contrasts between the cold polar air over the ice and the warm air being advected by southerly winds (see Section 3.1). These facts led us to speculate the existence and importance of a LL baroclinic zone for the development of the polar low.

As previously mentioned, UL PVAs may have a considerable cyclonic influence on the LL thermal field or baroclinic zone (e.g., Martin 2006). They can interact with warm anomalies, which are by definition LL positive PVAs. In turn, these LL anomalies can also influence the UL anomaly, leading to a reciprocal amplification mechanism, as

illustrated schematically in Figure 3.26 (Hoskins et al. 1985). The penetration depth of these anomalies determines to what extent they will affect each other.

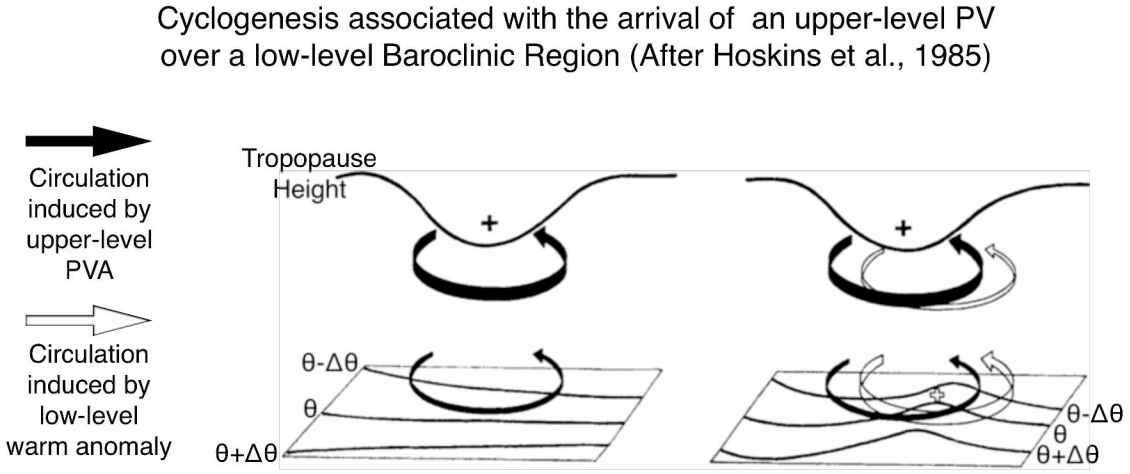

Figure 3.26: Cyclogenesis associated with the arrival of an upper-level PVA over a low-level baroclinic zone. Solid line with plus sign represents tropopause height and an upper-level PVA. Solid arrows represent the circulation induced by the PVA. Lower contours are potential temperature. Hollow plus sign represents a warm temperature anomaly at lower levels. Hollow arrows indicate the circulation induced by the low-level warm anomaly. Modified after Hoskins et al. (1985).

Considering the evidence presented for an UL PVA, this section investigates the existence of a LL baroclinic zone as well as its interaction with the PVA. The main parameter in this analysis is the Eady Growth Rate (EGR). It quantifies the baroclinicity by considering wind shear and static stability (Hoskins and Valdes 1990). As expressed by Lindzen and Farrell (1980), it is a "simple, powerful approximate result for the growth rate of the most rapidly growing instability" and is "linearly proportional to the surface meridional temperature gradient." It is expressed by Eq. 3.8, where f is the

Coriolis parameter, N is the Brunt-Vaisala frequency and $\vec{V}$ is the horizontal wind. The Brunt-Vaisala frequency is a measure of static stability and is given by Eq. 3.9, where g is gravity and θ is potential temperature.

$$EGR = 0.31 \frac{f}{N} \left| \frac{\partial \vec{V}}{\partial z} \right| \qquad \text{Eq. 3.8}$$

$$N^2 = \frac{g}{\theta} \frac{d\theta}{dz} \qquad \text{Eq. 3.9}$$

According to Rasmussen and Turner (2003), shallow baroclinic instability is often confined to a shallow boundary layer, below 850 hPa. This fact is not the case for the CBS polar low. The observed baroclinic zone extended from ~850 hPa to ~700 hPa, indicating a relatively deep baroclinicity. The maximum values were found near 800 hPa (Figure 3.27). Near the time of polar low development (a) the UL PVA was centered at ~70°N, 165°W, just downstream of the LL baroclinic zone. As the low continued to develop and mature (b-c), the baroclinic zone intensified and advanced northward along with the PVA. Even as they moved, the baroclinic zone continued to follow the PVA. This behavior indicates a relationship between these features.

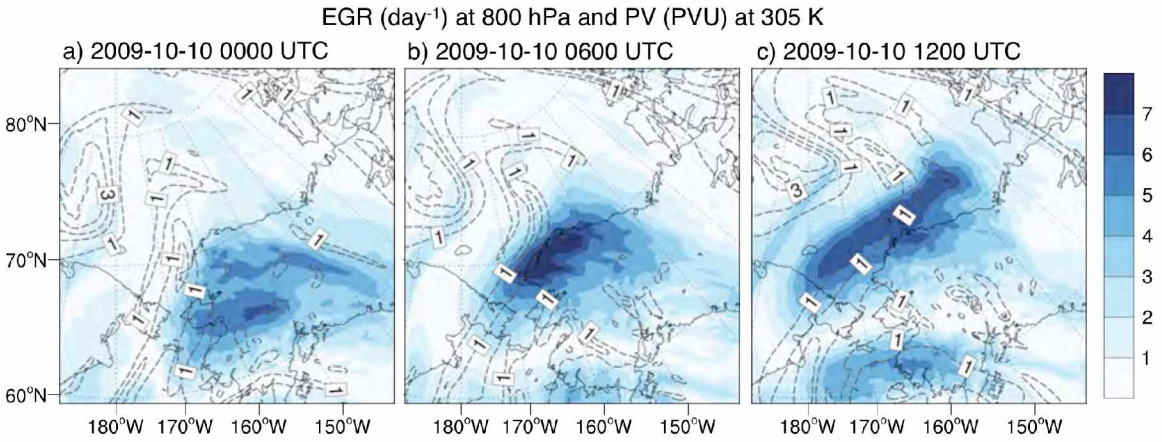

Figure 3.27: EGR at 800 hPa and PV at 305 K. Valid for October 10, 2009 at 0000 UTC (a), 0600 UTC (b) and 1200 UTC (c). EGR (blue shaded contours). Unit: day^{-1}. Potential vorticity (black dashed contours at 1 PVU intervals). Unit: PVU.

As indicated by the expression for EGR, baroclinic instability is closely related to the vertical shear. It can be related to either forward or reverse shear. Forward shear baroclinicity is the most common type, where the thermal wind and the mean wind at low levels are almost parallel and from the same direction. The warm air lies to the right of both the thermal wind and the mean flow. In a reverse shear situation the thermal and mean winds are still parallel, but from opposite directions. The warm air is still to the right of the thermal wind, but to the left of the mean flow (e.g., Kolstad 2006).

In order to investigate the characteristics of the LL shear, thermal wind was calculated as expressed by Eq. 3.10 for the layer from 925 hPa to 700 hPa. It can be derived from Figure 3.28 that in the Chukchi Sea region the thermal wind (a) and the environmental wind (b) were almost parallel and from the same direction, indicating a classic case of forward shear baroclinic instability.

$$\vec{V}_T = \frac{1}{f}\hat{k} \times \nabla \phi \qquad \text{Eq. 3.10}$$

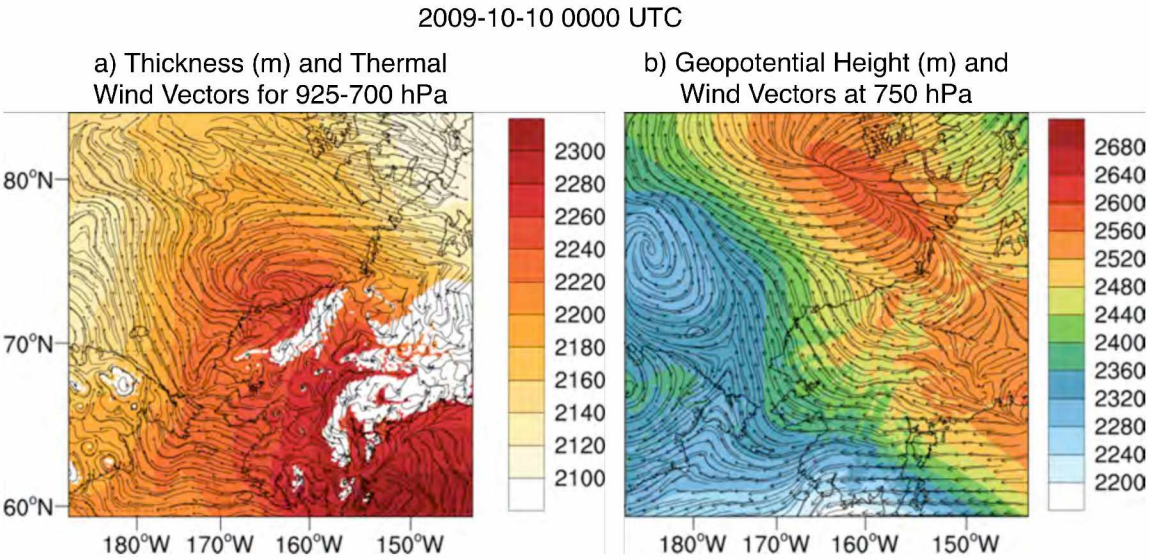

Figure 3.28: Forward shear in 925-700 hPa layer. Valid for October 10, 2009 at 0000 UTC. Thickness (unit: m) and thermal wind vectors for the 925-700 hPa layer (a). Geopotential height (unit: m) and wind vectors at 750 hPa (b).

3.6 Synoptic and Dynamic Summary

The analysis conducted throughout this chapter indicates that the CBS polar low had a hybrid development, since several forcings acted together towards its formation and intensification. This section presents a synoptic and dynamical summary of the polar low development based on the discussions presented so far. The diagrams presented consider four time frames, as shown in Table 3.3.

Table 3.3: Polar low phases.

Phase	Approximate Starting Time	Approximate Ending Time
Before	October 9, 2009 1000 UTC	October 9, 2009 1600 UTC
Developing	October 9, 2009 1700 UTC	October 9, 2009 2200 UTC
Mature	October 9, 2009 2300 UTC	October 10, 2009 0300 UTC
Dissipating	October 10, 2009 0400 UTC	October 10, 2009 1200 UTC

A simplified diagram of the synoptic situation associated with the polar low development can be seen in Figure 3.29. Before the low formed (a), two precursors could be identified: an UL closed low and a surface trough. Both were induced by the AL. The surface trough was likely further enhanced by the southerly flow encountering the Brooks Range in the Alaska North Slope. As a second synoptic low approached (b), the surface trough along the Alaska coast intensified and the BH retreated. The convergence zone between the high and lows established a steady southeasterly flow that brought moisture and heat from lower latitudes into the Chukchi Sea (c). This energy and moisture supply was present throughout the atmosphere and was maximum near ~850 hPa as evidenced from moist static energy calculations (Figure 3.9). After cutting off from the synoptic low, the polar low moved northwestward towards the UL closed low. Once they connected (d), the system was vertically stacked and had dissipated.

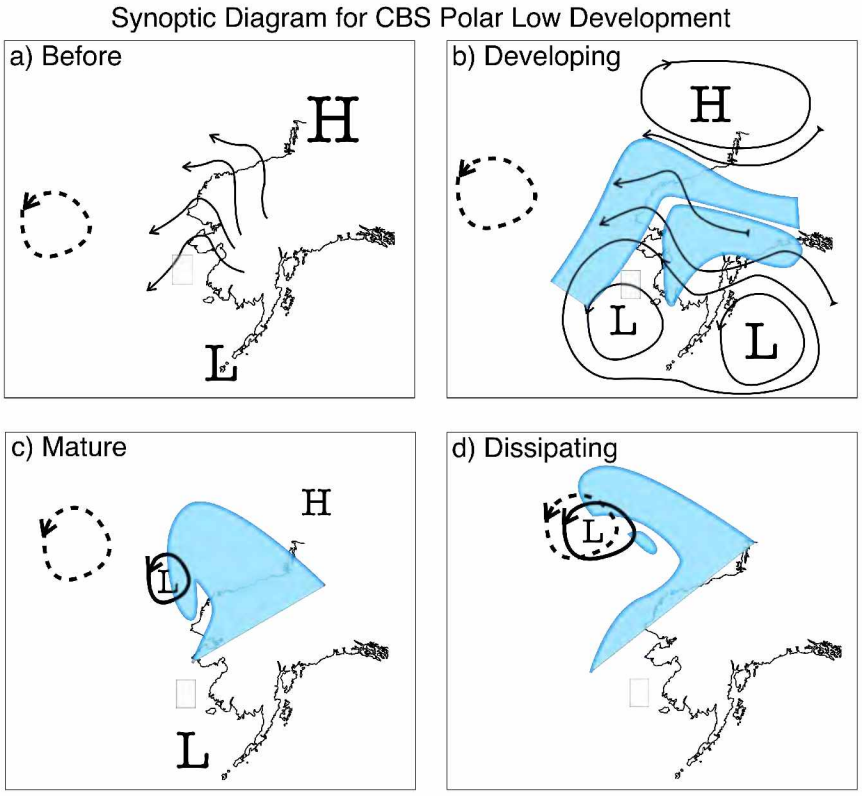

Figure 3.29: Synoptic diagram associated with CBS polar low development. Time frames are before (a), developing phase (b), mature phase (c) and dissipating phase (d). Dashed (solid) lines are UL (surface) circulation. Blue shaded areas represent the approximate cloud structure associated with the polar low as derived from simulated OLR.

A more specific summary can be derived from the dynamical diagram shown in Figure 3.30. Before the low formed (a), the only obvious precursor was a southerly flow into the Chukchi Sea that brought heat and moisture into the region, as previously mentioned. Associated with the synoptic Aleutian low we could also see a baroclinic zone and an UL PVA. The arrival of the jet stream (b) brought the baroclinic zone further north and caused this PVA to split in two. The southern portion of the PVA remained behind and the northern portion was released from the synoptic low. Meanwhile, the

continuous advection of heat and moisture brought on by the synoptic flow provided favorable conditions for the polar low formation and contributed to the development of a low-level warm anomaly and the intensification of the baroclinic zone, which was maximized near ~800 hPa. As the jet stream intensified and moved northward, it also drove the PVA and the baroclinic zone further north (c) and these two features tracked together towards the Chukchi Sea. The PVA was located right above the polar low closed circulation at lower levels and penetrated deep to ~600 hPa. This PVA likely interacted with the LL warm anomaly resulting in the polar low cyclogenesis. As the jet further developed (d) the PVA lost strength and the polar low was released. The polar low moved northward towards the UL closed low, which also had an associated UL PVA. Once the surface low reached the UL disturbance, the system was vertically stacked and had dissipated.

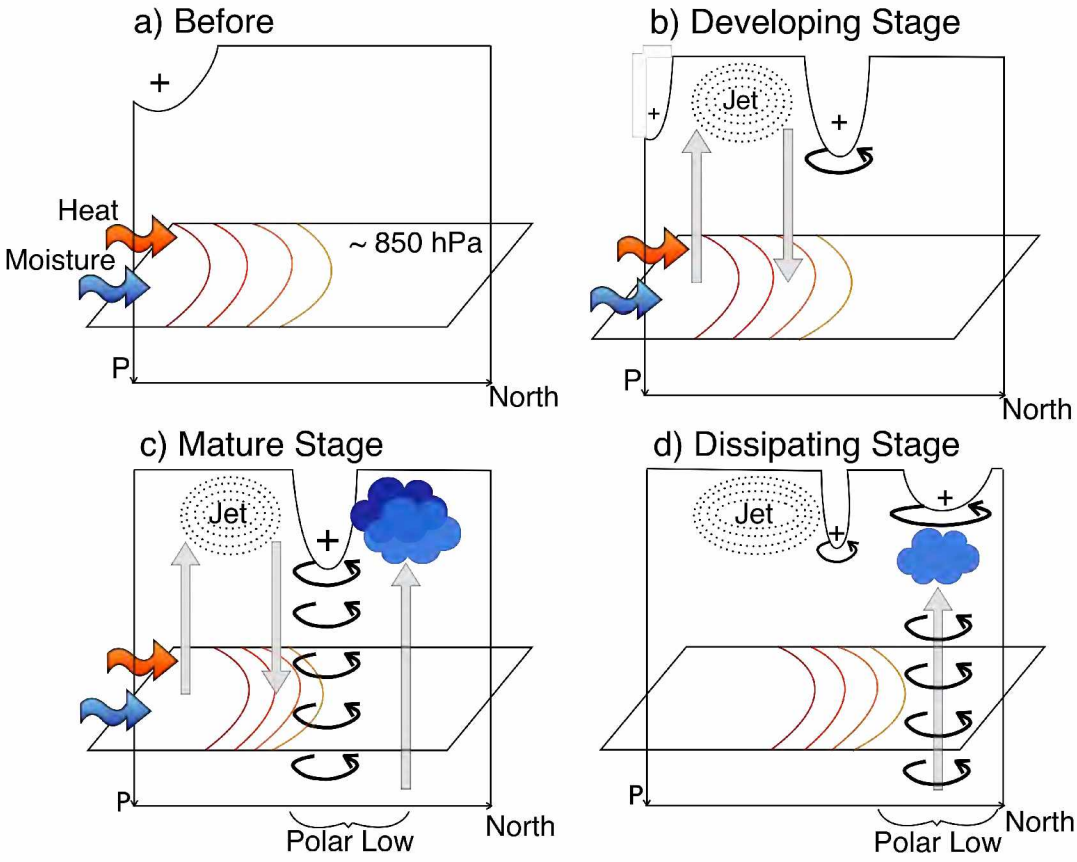

Figure 3.30: Dynamical diagram associated with CBS polar low development. Time frames are before (a), developing phase (b), mature phase (c) and dissipating phase (d). Cross sections have pressure in the vertical axes and latitude in the horizontal axis. Solid line topping each panel represents the tropopause height and associated PVAs. Dotted lines are isotachs. Colored lines are isotherms at the 850 hPa surface. Orange (blue) arrows represent southerly winds and advection of heat (moisture). Black (gray) arrows represent horizontal (vertical) circulation.

Chapter 4: Summary and Conclusions

The work presented in this thesis indicates that it is possible to obtain a realistic simulation of this small-scale polar low system, and that spectral nudging is a valuable technique for improving the quality of simulations. The diagnostic analyses indicate that this polar low had a hybrid development and that surface forcings were not important for its formation and intensification. The polar low was likely triggered by the interaction of an upper-level potential vorticity anomaly over a low-level baroclinic zone, and the presence of these features was favored by the synoptic environment in which the polar low formed. In this chapter, we provide a brief summary of the research presented in this thesis and of the main findings.

4.1 Research Summary

Overall, no single theoretical model can be applied for explaining the development of polar lows. The forcing mechanisms involved vary depending on the location where the system occurs and even from case to case. Since polar lows are infrequent in the Chukchi and Beaufort Seas, very few polar low studies have given attention to this region. This work intends to fill in this gap by studying the unusual event of a polar low that developed in this sector on October 9-10, 2009. Modeling experiments were conducted with WRF in order to determine the most appropriate model configuration for obtaining a realistic simulation of the storm. The model data was evaluated against observational data from conventional weather stations, radiosonde sites and the QuikSCAT satellite sensor. The validity of the selected WRF configuration was further tested by application to a second polar low case and in an ensemble analysis. Data

from the best-performing simulation was used for carrying out diagnostic analyses. Mechanisms known to be important for polar low development such as ocean forcings, potential vorticity anomalies and baroclinicity were examined and their role in this case was investigated.

4.2 Results Summary and Outlook

Modeling experiments have demonstrated that it is possible to obtain a realistic and reliable simulation of the polar low. The model revealed sensitivity to physical parameterizations, especially for wind speed. The Morrison microphysics and Yonsei University boundary layer schemes were proven to provide the smallest errors. The main difference between Morrison and the other microphysics options in WRF is that it is a double-moment scheme that predicts not only mixing ratios but also number concentrations. The distinguishing feature for Yonsei University is the fact that it explicitly resolves entrainment processes at the top of the boundary layer.

With regard to large-scale forcings, the most suitable dataset for providing initial and boundary conditions to the model was found to be ERA-Interim. The model was also sensitive to the use of spectral nudging techniques. The largest sensitivity was again seen for wind. The use of spectral nudging was found to improve the simulation as long as nudging was performed throughout the entire simulation duration. It additionally corrected model biases regarding the location and time of surface cyclogenesis. Considering all of the analyses, the selected simulation had nudging enabled for the parent domain at all simulation hours, at every time step, at all levels and with the default

coefficient of $3x\ 10^{-4}\ s^{-1}$ for wind, geopotential height and mixing ratio. Only wave numbers greater than three were nudged.

Two main synoptic features can be considered important precursors for the development of the polar low, and could be identified more than 24 hours before its development. The first was the presence of an UL closed low west of the region where the polar low developed. This UL low originated from the synoptic (Aleutian) low and its cyclonic circulation penetrated downwards with time, reaching as far down as 850 hPa immediately before the onset of the polar low at the surface. The second precursor was a convergence zone formed between the AL and the BH. The associated southerly flow continually brought warm and moist air creating a favorable environment for the development of convection and contributing to the intensification of the low-level baroclinic zone and the development of a warm anomaly.

A sensitivity experiment using climatological lower boundary conditions indicated that SST and SIC did not play an important role for the storm development. The impacts of these surface forcings were not able to penetrate above 850 hPa due to a stably stratified lower atmosphere. Their effects were limited to a shallow layer above the surface. Even at lower levels, their effect was not substantial. Differences in intensity can be seen for a few surface fields such as surface fluxes, 10-meter winds, 2-meter temperatures and SLP. The SLP mean difference indicates that the polar low was less intense by ~0.8 hPa and the BH by ~0.2 hPa when the simulation was forced with the climatological fields. Additionally, the surface fluxes were less intense in the Chukchi Sea, where the SSTs were lower and the SIC was higher in the climatological fields.

Instead of lower boundary forcings, two other mechanisms seemed to have played the major role for the polar low to develop: an UL PVA and a LL baroclinic zone. They were both advected from lower latitudes, where they were associated with the advancing and intensifying synoptic low. Their movement into the Chukchi Sea was driven by the arrival and intensification of the jet stream into this region. The PVA was located just downstream of the jet and penetrated down to ~600 hPa. The baroclinic zone was positioned underneath the jet, extending from ~850 hPa to ~700 hPa with maximum intensity at ~800 hPa.

According to the discussion presented, the following points summarize the major findings:

- The results are sensitive to physical parameterizations and Morrison microphysics and Yonsei University boundary layer yield the most realistic results;
- ERA-Interim is the large-scale forcing dataset that yields the most realistic polar low simulation;
- The use of spectral nudging presents an overall improvement in the simulation, as long as it is performed during all simulation hours;
- Lower boundary forcings did not play an important role for the development of this polar low case and their effects were small and limited to a shallow layer below 850 hPa, likely due to a stably stratified lower atmosphere;

- The main precursors for the development were an upper-level closed low and the southerly winds associated with the convergence zone between the synoptic AL and BH;
- The polar low had a hybrid development, and the features that likely triggered and supported the polar low cyclogenesis were a deep-penetrating UL PVA (which was driven northward by the jet stream) and a LL baroclinic zone (which was intensified due to warm advection brought on by the synoptic configuration).

The results discussed in this thesis represent a first step towards understanding this unusual polar low occurrence in the Chukchi and Beaufort Seas. These findings provide an important introduction to the dynamics behind this polar low and may have significant implications for better understanding weather systems and extreme events in a changing Arctic climate system. A more detailed analysis along with energy budget considerations would be necessary in order to precisely determine the individual contributions of different forcings to the development of this unique storm. Likewise, in order to fully understand the relationship between this polar low and the recent changes in climate, it would be necessary to look beyond sea ice and sea-surface temperature forcings. Air temperature, large-scale synoptic patterns and changes in storm track dynamics are a few examples of additional parameters that can be linked to changes in climate and that might be connected to polar low developments in the CBS region. Understanding this connection would allow us to better assess future changes in the

genesis of polar lows and to improve the capabilities of operationally forecasting these intense systems.

References

Alexandru, A., R. de Elia, R. Laprise, L. Separovic, and S. Biner, 2009: Sensitivity Study of Regional Climate Model Simulations to Large-Scale Nudging Parameters. *Monthly Weather Review*, **137,** 1666-1686.

Auer, A. H., 1986: An Observational Study of Polar Air Depressions in the Australian Region. *Second International Conference on Southern Hemispheric Meteorology*, Boston, American Meteorological Society, 46-49.

Back, L. E., and C. S. Bretherton, 2006: Geographic variability in the export of moist static energy and vertical motion profiles in the tropical Pacific. *Geophys. Res. Lett.*, **33,** L17810.

Black, R. I., 1982: Beaufort Storm of July, 1982. Satellite and Beaufort Office, 18.

Blechschmidt, A. M., S. Bakan, and H. Grafll, 2009: Large-scale atmospheric circulation patterns during polar low events over the Nordic seas. *J. Geophys. Res.*, **114,** D06115.

Bracegirdle, T. J., and S. L. Gray, 2008: An objective climatology of the dynamical forcing of polar lows in the Nordic seas. *International Journal of Climatology*, **28,** 1903-1919.

——, 2009: The dynamics of a polar low assessed using potential vorticity inversion. *Quarterly Journal of the Royal Meteorological Society*, **135,** 880-893.

Bresch, J. F., R. J. Reed, and M. D. Albright, 1997: A Polar-Low Development over the Bering Sea: Analysis, Numerical Simulation, and Sensitivity Experiments. *Monthly Weather Review*, **125,** 3109-3130.

Bromwich, D. H., K. M. Hines, L. Bai, and Sheng, 2009: Development and testing of Polar Weather Research and Forecasting model: 2. Arctic Ocean. *J. Geophys. Res.*, **114,** D08122.

Brümmer, B., G. Müller, and G. Noer, 2009: A Polar Low Pair over the Norwegian Sea. *Monthly Weather Review*, **137,** 2559-2575.

Brunner, R., and Coauthors: University of Colorado Boulder Arctic Climate Project: Big Storms, Flooding and Erosion: Impacts of Climate Change in Barrow. [Available online at http://nome.colorado.edu/HARC/Seminar/senatorsposter.pdf.]

Businger, S., 1987: The synoptic climatology of polar-low outbreaks over the Gulf of Alaska and the Bering Sea. *Tellus A*, **39A,** 307-325.

Businger, S., and R. J. Reed, 1989: Cyclogenesis in Cold Air Masses. *Weather and Forecasting*, **4,** 133-156.

Cassano, E. N., A. H. Lynch, J. J. Cassano, and M. R. Koslow, 2006: Classification of synoptic patterns in the western Arctic associated with extreme events at Barrow, Alaska, USA. *Climate Research*, **30,** 83-97.

Cassano, J. J., M. E. Higgins, and M. W. Seefeldt, 2011: Performance of the Weather Research and Forecasting (WRF) Model for Month-long pan-Arctic Simulations. *Monthly Weather Review*.

Center, N. A. E., cited 2011: Oil and Gas Industry Toxic Spills 1996-2008 Map. [Available online at http://northern.org/news/oil-and-gas-industry-toxic-spills-1996-2008-map.]

Chen, F., and J. Dudhia, 2001: Coupling an Advanced Land Surface–Hydrology Model with the Penn State–NCAR MM5 Modeling System. Part I: Model Implementation and Sensitivity. *Monthly Weather Review*, **129,** 569-585.

Chen, S.-H., and W.-Y. Sun, 2002: A One-dimensional Time Dependent Cloud Model. *Journal of the Meteorological Society of Japan*, **80,** 99-118.

Claud, C., B. Duchiron, and P. Terray, 2007: Associations between large-scale atmospheric circulation and polar low developments over the North Atlantic during winter. *J. Geophys. Res.*, **112,** D12101.

Claud, C., G. Heinemann, E. Raustein, and L. McMurdie, 2004: Polar low le Cygne: Satellite observations and numerical simulations. *Quarterly Journal of the Royal Meteorological Society*, **130,** 1075-1102.

Comiso, J. C., C. L. Parkinson, R. Gersten, and L. Stock, 2008: Accelerated decline in the Arctic sea ice cover. *Geophys. Res. Lett.*, **35,** L01703.

Condron, A., G. R. Bigg, and I. A. Renfrew, 2006: Polar Mesoscale Cyclones in the Northeast Atlantic: Comparing Climatologies from ERA-40 and Satellite Imagery. *Monthly Weather Review*, **134,** 1518-1533.

Dannevig, P., 1954: *Meteorologi for Flygere*. Aschehoug.

Deng, A., D. R. Stauffer, J. Dudhia, T. Otte, and G. K. Hunter, 2007: Update on analysis nudging FDDA in WRF-ARW. *8th WRF Users' Workshop*, Boulder, CO.

Dudhia, J., 1989: Numerical Study of Convection Observed during the Winter Monsoon Experiment Using a Mesoscale Two-Dimensional Model. *Journal of Atmospheric Sciences*, **46,** 3077-3107.

Fett, R. W., 1992: Navy Tactical Applications Guide. Part 2: Arctic-East Siberian/Chukchi/Beaufort Seas. Weather Analysis and Forecast Applications., N. R. Laboratory, Ed.

Fetterer, F., K. Knowles, W. Meier, and M. Savoie, 2002: Sea Ice Index. National Snow and Ice Data Center, Boulder, CO, digital media. [Available online at http://nsidc.org/data/g02135.html].

Forbes, G. S., and W. D. Lottes, 1985: Classification of mesoscale vortices in polar airstreams and the influence of the large-scale environment on their evolutions. *Tellus A*, **37A,** 132-155.

Gang, F., 2001: *Polar Lows: Intense Cyclones in Winter* China Meteorological Press, 218 pp.

Grell, G. A., and D. Dévényi, 2002: A generalized approach to parameterizing convection combining ensemble and data assimilation techniques. *Geophys. Res. Lett.*, **29,** 1693.

Harrold, T. W., and K. A. Browning, 1969: The polar low as a baroclinic disturbance. *Quarterly Journal of the Royal Meteorological Society*, **95,** 710-723.

Heinemann, G., 1996: A wintertime polar low over the eastern Weddell Sea (Antarctica): A study with AVHRR, TOVS, SSM/I and conventional data. *Meteorology and Atmospheric Physics*, **58,** 83-102.

Holton, J. R., 2004: *An introduction to dynamic meteorology*. Vol. 88, Academic Press, 535 pp.

Hong, S.-Y., and H.-L. Pan, 1996: Nonlocal Boundary Layer Vertical Diffusion in a Medium-Range Forecast Model. *Monthly Weather Review*, **124**.

Hong, S.-Y., and J.-O. Lim, 2006: The WRF Single-Moment 6-Class Microphysics Scheme (WSM6). *J. Korean Meteor. Soc.*, **42,** 129-151.

Hong, S.-Y., J. Dudhia, and S.-H. Chen, 2004: A Revised Approach to Ice Microphysical Processes for the Bulk Parameterization of Clouds and Precipitation. *Monthly Weather Review*, **132,** 103-120.

Hong, S.-Y., Y. Noh, and J. Dudhia, 2006: A New Vertical Diffusion Package with an Explicit Treatment of Entrainment Processes. *Monthly Weather Review*, **134,** 2318-2341.

Hoskins, B. J., and P. J. Valdes, 1990: On the Existence of Storm-Tracks. *Journal of Atmospheric Sciences*, **47,** 1854-1864.

Hoskins, B. J., M. E. McIntyre, and A. W. Robertson, 1985: On the use and significance of isentropic potential vorticity maps. *Quarterly Journal of the Royal Meteorological Society*, **111,** 877-946.

Inoue, J., M. E. Hori, Y. Tachibana, and T. Kikuchi, 2010: A polar low embedded in a blocking high over the Pacific Arctic. *Geophys. Res. Lett.*, **37,** L14808.

Janjic, Z. I., 2000: Nonsingular implementation of the Mellor–Yamada level 2.5 scheme in the NCEP Meso model. NCEP Office Note No. 437, 61.

Kanamaru, H., and M. Kanamitsu, 2007: Scale-Selective Bias Correction in a Downscaling of Global Analysis Using a Regional Model. *Monthly Weather Review*, **135,** 334-350.

Kolstad, E., and T. Bracegirdle, 2008: Marine cold-air outbreaks in the future: an assessment of IPCC AR4 model results for the Northern Hemisphere. *Climate Dynamics*, **30,** 871-885.

Kolstad, E. W., 2006: A new climatology of favourable conditions for reverse-shear polar lows. *Tellus A*, **58,** 344-354.

Lim, K.-S. S., and S.-Y. Hong, 2009: Development of an Effective Double-Moment Cloud Microphysics Scheme with Prognostic Cloud Condensation Nuclei (CCN) for Weather and Climate Models. *Monthly Weather Review*, **138,** 1587-1612.

Linders, T., and Ø. Saetra, 2010: Can CAPE Maintain Polar Lows? *Journal of the Atmospheric Sciences*, **67,** 2559-2571.

Lindzen, R. S., and B. Farrell, 1980: A simple approximate result for the maximum growth rate of baroclinic instabilities. *Journal of Atmospheric Sciences*, **37,** 1648-1653.

Lo, J. C.-F., Z.-L. Yang, and R. A. Pielke, Sr., 2008: Assessment of three dynamical climate downscaling methods using the Weather Research and Forecasting (WRF) model. *J. Geophys. Res.*, **113,** D09112.

Lyall, I. T., 1972: The polar low over Britain. *Weather and Forecasting*, **27,** 378-390.

Lynch, A. H., E. N. Cassano, J. J. Cassano, and L. R. Lestak, 2003: Case Studies of High Wind Events in Barrow, Alaska: Climatological Context and Development Processes. *Monthly Weather Review*, **131,** 719-732.

Mailhot, J., D. Hanley, B. Bilodeau, and O. Hertzman, 1996: A numerical case study of a polar low in the Labrador Sea. *Tellus A*, **48,** 383-402.

Martin, J. E., 2006: *Mid-Latitude Atmospheric Dynamics*. Wiley, 336 pp.

Meinke, I., B. Geyer, F. Feser, and H. von Storch, 2006: The Impact of Spectral Nudging on Cloud Simulation with a Regional Atmospheric Model. *Journal of Atmospheric and Oceanic Technology*, **23,** 815-824.

Mellor, G. L., and T. Yamada, 1982: Development of a turbulence closure model for geophysical fluid problems. *Rev. Geophys.*, **20,** 851-875.

Michalakes, J., J. Dudhia, D. Gill, T. Henderson, J. Klemp, W. Skamarock, and W. Wang, 2005: The Weather Research and Forecast Model: Software Architecture and Performance. *Eleventh ECMWF Workshop on the Use of High Performance Computing in Meteorology*, World Scientific, 156-168.

Miguez-Macho, G., G. L. Stenchikov, and A. Robock, 2004: Spectral nudging to eliminate the effects of domain position and geometry in regional climate model simulations. *J. Geophys. Res.*, **109,** D13104.

Mlawer, E. J., S. J. Taubman, P. D. Brown, M. J. Iacono, and S. A. Clough, 1997: Radiative transfer for inhomogeneous atmospheres: RRTM, a validated correlated-k model for the longwave. *J. Geophys. Res.*, **102,** 16663-16682.

Mölders, N., H. N. Q. Tran, P. Quinn, K. Sassen, G. E. Shaw, and G. Kramm, 2011: Assessment of WRF/Chem to simulate sub–Arctic boundary layer characteristics during low solar irradiation using radiosonde, SODAR, and surface data. *Atmospheric Pollution Research* **2,** 283-299.

Moore, R. W., and T. H. Vonder Haar, 2003: Diagnosis of a Polar Low Warm Core Utilizing the Advanced Microwave Sounding Unit. *Weather and Forecasting*, **18,** 700-711.

Morrison, H., G. Thompson, and V. Tatarskii, 2009: Impact of cloud microphysics on the development of trailing stratiform precipitation in a simulated squall line: Comparison of one- and two-moment schemes. *Monthly Weather Review*, **137,** 991-1007.

Nakanishi, M., 2001: Improvement Of The Mellor Yamada Turbulence Closure Model Based On Large-Eddy Simulation Data. *Boundary-Layer Meteorology*, **99,** 349-378.

Nordeng, T. E., and E. A. Rasmussen, 1992: A most beautiful polar low. A case study of a polar low development in the Bear Island region. *Tellus A*, **44,** 81-99.

Owen Mason, W. J. N., Orrin H. Pilkey, Jane Bullock, Ted Fathauer, Deborah F. Pilkey, Douglas Swanston, 1997: *Living with the Coast of Alaska*. Duke University Press, 348 pp.

Pagowski, M., and G. W. K. Moore, 2001: A Numerical Study of an Extreme Cold-Air Outbreak over the Labrador Sea: Sea Ice, Air–Sea Interaction, and Development of Polar Lows. *Monthly Weather Review*, **129,** 47-72.

Parker, M. N., 1989: Polar Lows in the Beaufort Sea. *Polar and Arctic Lows*, A. Deepak, 323-330.

Pleim, J. E., 2007: A Combined Local and Nonlocal Closure Model for the Atmospheric Boundary Layer. Part I: Model Description and Testing. *Journal of Applied Meteorology and Climatology*, **46,** 1383-1395.

Rasmussen, E. A., and J. Turner, 2003: *Polar Lows: Mesoscale Weather Systems in the Polar Regions*. Cambridge Univ. Press, 612 pp.

Reed, R. J., 1979: Cyclogenesis in Polar Air Streams. *Monthly Weather Review*, **107,** 38-52.

Shapiro, M. A., L. S. Fedor, and T. Hampel, 1987: Research aircraft measurements of a polar low over the Norwegian Sea. *Tellus A*, **39A,** 272-306.

Skamarock, W., J. Klemp, J. Dudhia, D. Gill, D. M. Barker, W. Wang, and J. G. Powers, 2005: A description of the Advanced Research WRF Version 2. *NCAR Tech. Note NCAR/TN-468&STR*, 88.

Skamarock, W. C., and J. B. Klemp, 2008: A time-split nonhydrostatic atmospheric model for weather research and forecasting applications. *Journal of Computational Physics*, **227**.

Stauffer, D. R., and N. L. Seaman, 1990: Use of Four-Dimensional Data Assimilation in a Limited-Area Mesoscale Model. Part I: Experiments with Synoptic-Scale Data. *Monthly Weather Review*, **118,** 1250-1277.

Storch, H. v., and F. W. Zwiers, 2002: *Statistical Analysis in Climate Research*. Cambridge University Press

Sukoriansky, S., B. Galperin, and V. Perov, 2006: A quasi-normal scale elimination model of turbulence and its application to stably stratified flows. *Nonlin. Processes Geophys.*, **13,** 9-22.

Sumner, E. J., 1950: The significance of vertical stability in synoptic development. *Quarterly Journal of the Royal Meteorological Society*, **76,** 384-392.

Tao, W.-K., and J. Simpson, 1993: The Goddard Cumulus Ensemble Model Part I: model description. *Terrestrial, Atmospheric and Oceanic Sciences*, **4,** 35-71.

Thompson, G., R. M. Rasmussen, and K. Manning, 2004: Explicit Forecasts of Winter Precipitation Using an Improved Bulk Microphysics Scheme. Part I: Description and Sensitivity Analysis. *Monthly Weather Review*, **132,** 519-542.

Turner, J., T. A. Lachlan-Cope, and J. C. Moore, 1992: A comparison of satellite sounding data and aircraft measurements within a mature polar low. *Tellus A*, **44,** 119-132.

Turner, J., T. A. Lachlan-Cope, and J. P. Thomas, 1993: A Comparison of Arctic and Antarctic Mesoscale Vortices. *J. Geophys. Res.*, **98,** 13019-13034.

Uppala, S. M., and Coauthors, 2005: The ERA-40 re-analysis. *Quarterly Journal of the Royal Meteorological Society*, **131,** 2961-3012.

Weaver, C. P., S. Baidya Roy, and R. Avissar, 2002: Sensitivity of simulated mesoscale atmospheric circulations resulting from landscape heterogeneity to aspects of model configuration. *J. Geophys. Res.*, **107,** 8041.

Weisse, R., and F. Feser, 2003: Evaluation of a method to reduce uncertainty in wind hindcasts performed with regional atmosphere models. *Coastal Engineering*, **48,** 211-225.

Wilson, H. P., 1971: An Interesting Arctic Storm.

Workgroup, I. A., 2008: Recommendations Report to the Governor's Subcabinet on Climate Change.

Wu, L., and G. W. Petty, 2010: Intercomparison of Bulk Microphysics Schemes in Model Simulations of Polar Lows. *Monthly Weather Review*, **138,** 2211-2228.

Yanase, W., and H. Niino, 2007: Dependence of Polar Low Development on Baroclinicity and Physical Processes: An Idealized High-Resolution Numerical Experiment. *Journal of the Atmospheric Sciences*, **64,** 3044-3067.

Yanase, W., G. Fu, H. Niino, and T. Kato, 2004: A Polar Low over the Japan Sea on 21 January 1997. Part II: A Numerical Study. *Monthly Weather Review*, **132,** 1552-1574.

Zahn, M., and H. von Storch, 2010: Decreased frequency of North Atlantic polar lows associated with future climate warming. *Nature*, **467,** 309-312.

Zahn, M., H. Von Storch, and S. Bakan, 2008: Climate mode simulation of North Atlantic polar lows in a limited area model. *Tellus A*, **60,** 620-631.

Zhang, X., and J. E. Walsh, 2006: Toward a Seasonally Ice-Covered Arctic Ocean: Scenarios from the IPCC AR4 Model Simulations. *Journal of Climate*, **19,** 1730-1747.

Zhang, X., A. Sorteberg, J. Zhang, R. d. Gerdes, and J. C. Comiso, 2008: Recent radical shifts of atmospheric circulations and rapid changes in Arctic climate system. *Geophys. Res. Lett.*, **35,** L22701.

Zhao, Q., T. L. Black, and M. E. Baldwin, 1997: Implementation of the Cloud Prediction Scheme in the Eta Model at NCEP. *Weather and Forecasting*, **12,** 697-712.